December 2020

Battery Integration to the Power Grid and Frequency Regulation

Roghieh Abdollahi Biroon
Clemson University, rabdoll@clemson.edu

BATTERY INTEGRATION TO THE POWER GRID AND FREQUENCY REGULATION

A Dissertation
Presented to
the Graduate School of
Clemson University

In Partial Fulfillment
of the Requirements for the Degree
Doctor of Philosophy
Electrical Engineering

---

by
Roghieh Abdollahi Biroon
December 2020

Accepted by:
Dr. Ramtin Hadidi, Committee Chair
Dr. Pierluigi Pisu, Committee Co-Chair
Dr. David Schoenwald
Dr. Sukumar Brahma
Dr. Randy Collins

ABSTRACT

The growing interest in battery energy storage systems (BESSs) at both small-scale and large-scale levels in power grids highlights their significant roles in future power grids. The future grid in the presence of renewable resources such as hydro-power, wind, and solar energy face two major technical challenges; location of potential renewable sources and uncertainty, which can cause serious issues such as blackouts in power systems. However, in both cases, BESSs is one of the promising solutions. While small-scale battery energy storage systems can decrease the need for long-distance heavy load transportation in the power system, which is one of the primary reasons for the blackouts, large-scale BESSs can provide load frequency control to their fast response. A well-managed large-scale battery integration to the power grid reduces load flow deviation in the tie-lines and frequency oscillations caused by small load disturbances. In general, the battery's small time-constants, fast response, and high energy density creates a large spectrum of potential applications for BESSs in power systems.

This thesis focuses on the battery integration to the power system in both distribution and transmission level to evaluate its potential impact on power grid; then, it focuses on the frequency regulation by taking the advantage of the small-scale and large-scale batteries.

The first part of this research investigates the small-scale battery integration to the power system in the distribution level and its potential effects on the transmission level's frequency deviation. It is shown that the higher penetration level of the renewables can cause serious issues such as overvoltage, thermal, and frequency deviation issues in the

distribution and transmission levels under current tariffs. The load profile's sensitivity to the battery characteristics and its efficiency, and electricity tariffs are studied. Then, tariff modification as one of the promising tools for load profile adjustment is introduced to modify the customers' load profile and mitigate the frequency deviation. The results under modified tariffs are compared to the frequency control results in a small microgrid using model predictive control.

In the second chapter, the effect of those new loads on the power flow and inter-area oscillation modes are studied. Then a servomechanism controller is designed to damp the inter-area oscillations. Considering the small time constant of the large-scale battery, we model a large-scale battery integration to the power system to study the effect of its integration on the power system's stability. Finally, centralized and decentralized hybrid controls are designed on the inverter's firing angle to manage the large-scale battery's active and reactive power to damp the oscillations. Results show a notable improvement on frequency deviations.

DEDICATION

This dissertation is dedicated to my dear parents

ACKNOWLEDGMENTS

First, my greatest gratitude goes to my advisers Dr. Ramtin Hadidi and Dr. Pierluigi Pisu.

I would like to extend my appreciation towards my advisor Prof. Hadidi for his support, assistance and thoughtful comments during my Ph.D program. I enjoyed every moment of working with him as my advisor.

Next, I would like to sincere respects towards Prof. Pisu for his support, assistance, and patience during these five years of Ph.D journey. Under his supervision I have extended my knowledge and experience in control theory and this research would not be possible without his excellent mentorship. I am thankful to him for all hours he spent with me discussing control approaches.

I would also thank Dr. David Schoenwald for his support during my Ph.D. program. Dr. Schoenwald was so dedicated to spending his valuable time to his critical feedbacks on my publications during my Ph.D.

Next, I would like to thank my committee members Prof. Edward E. Collins and Prof. Sukumar Brahma for their insightful questions, critical feedback that helped me to improve this dissertation, and for their heartwarming words.

Next, I want to thank Dr. Imtiaz Haque and Dr. Elham Makram for their belief in me and giving this opportunity to me to fulfil my longtime promise to my father.

At last, I would like to express my gratitude to my beloved sister Zoleikha for her supports. There is no word to reflect my respect and appreciation for her.

This research is based on projects with Sandia National Laboratories under contract DE-NA0003525 funded by the U.S. Department of Energy's Energy Storage Program, managed by Dr. Imre Gyuk, Center for Advanced Power Engineering Research (CAPER) and Clemson University Electric Power Research Association (CUEPRA).

TABLE OF CONTENTS

TABLE OF FIGURE

CHAPTER ONE

INTRODUCTION

1.1. Overview and Motivation

The United States has considerable potential renewable energy resources. A total potential capacity of more than 8000 GW land-based wind and nearly 7,000 GW capacity of concentrated solar power in its seven southwestern states can be named as two primary renewable resources [1]. US total electrical energy consumption in 2019 was about 4127 terawatt-hours (Twh), which is less than 25 percent of potential energy that can be harvested in seven southwestern states [2]. However, developing renewable resources presents a new set of technological challenges to the power grids, including the locations of large-scale renewable resources that are usually far from population centers and the renewable generation's unpredictability and variability.

A small level of renewables can be smoothly integrated into the power grids; however, accommodating more than approximately 30 percent of the electricity generation from these renewable sources will be challenging and require new approaches to develop and operate the power grid. Uncertainty and variability can be dealt with by switching in and out fast-acting conventional reserves, installing large-scale storage on the grid, or long-distance transmission of renewable electricity to enable the access to larger pools of resources to balance regional and local excesses or deficits. At present, renewable variability is handled almost exclusively by ramping conventional reserves up or down based on forecasts. However, as renewable penetration level grows, storage and

transmission will likely become more cost-effective and necessary. As renewable generation grows, it will be most unlikely for the conventional resources to compensate for the renewables' variability. This issue will require the capture of electricity generated by wind, solar and other renewables for later use.

The other challenge in the future grid will be the power transmission. Renewable sources are typically distributed over large areas in the upper central and southwestern US, far from demand centers in east and west coasts (Fig. 1). This means new strategies and new long-distance transmission capability will be required to deliver enormous energy generated by renewables across the country to the demand centers.

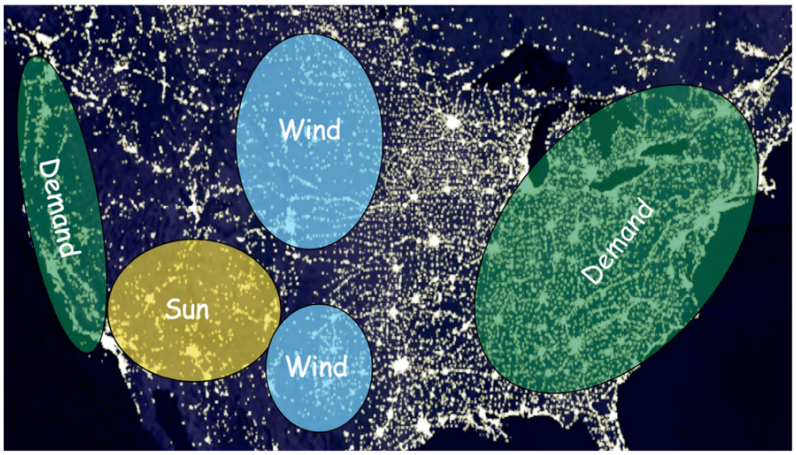

Figure 1. Separation between the renewable sources and demand centers [1]

On the other hand, heavily loaded long-distance transmission lines increase the likelihood of the inter-area oscillations and blackouts in the power system. The American Physical Society (APS) proposed a long-term plan to the Department of Energy (DOE) with regard to the renewables' integration to the power grid as follows [1]:

i) Extend the DOE/OE (Office of Energy) program on High-Temperature Superconductivity for ten years, with a focus on DC superconducting cables for long-distance transmission of renewable electricity from source to market-based on the given road map (Fig. 2);

ii) Accelerate R&D on wide bandgap power electronics for controlling power flow on the grid, including alternating to direct current conversion options and development of semiconductor-based circuit breakers operating at 200 kV and 50 kA with microsecond response time; and

iii) Develop an overall strategy for energy storage in grid-level applications that guide regulators to recognize the value that energy storage brings to the grid's transmission and generation services.

Considering the promising position of the battery in the future power grid, a comprehensive study on the effect of battery integration to the power system in both distribution and transmission level is required.

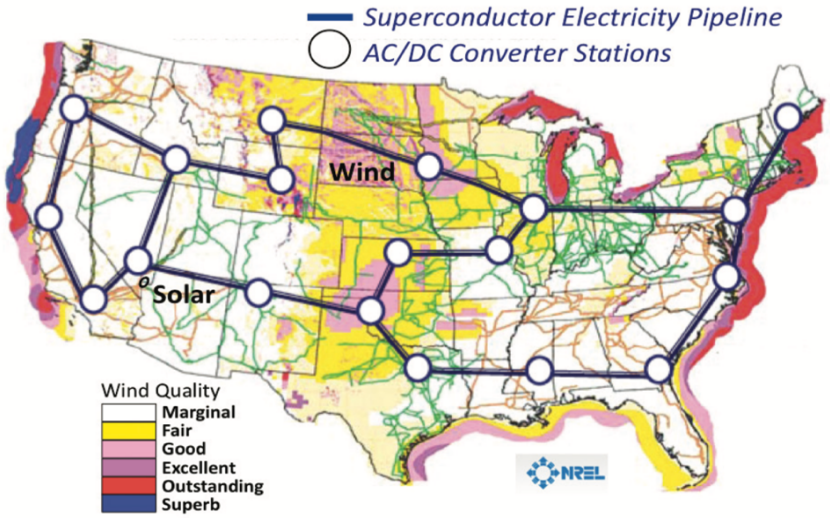

Figure 2. The proposed DC superconductor electricity pipeline for carrying large amounts of renewable power [1]

This research has studied the impact of the battery integration's high penetration level on voltage and frequency deviation in the distribution system. In this subject, tariff modification is proposed to mitigate the battery integration's negative influence on the distribution level, especially on the voltage and frequency deviation. The results are compared to the Model Predictive Control (MPC) approach to evaluate the approach's effectiveness; yet, tariff modification is a complicated and time-consuming procedure. The higher penetration level of the renewables, under existing tariffs, in the distribution system will cause a higher power flow rate in the transmission level. To control the inter-area oscillations resulting from the power flow deviation in transmission level, we studied the inter-area oscillations damping scenario by employing the large-scale batteries in the transmission level.

1.2. Opportunities and Challenges

Considering interest in renewable energy, unmanaged renewables integration to the power system can cause severe issues in both distribution and transmission level such as;

Distribution level

Higher renewables under current tariffs encourage to charge and discharge at the same time intervals. This policy will be beneficial for both renewable owners and utilities in the renewables' lower penetration level. The distribution system will experience reverse power flow from the end-users toward the generation system in a renewable rich system. The existing distribution system is designed for one-way power flow from generation toward users, and feeders' capacity decreases as they become close to the end-users. As a result of existing electricity rating policy and distribution system structure, renewables integration into the distribution system can cause the following challenges:

i) Voltage deviation

ii) Thermal issues in distribution feeders

iii) Frequency deviation in islanded microgrids

iv) Unbalance system

Transmission level

The negative impact of the unmanaged renewables integration into the distribution level will not be limited to the distribution system and will affect the transmission level. Studies show that 30 percent of renewables integration causes higher load flow and puts higher stress on transmission lines. Also, load deviation causes inter-area oscillation in the power

system, which can cause serious issues to the generation system. These impacts can be summarized as:

i) Higher peak to average ratio

ii) Frequency deviation, mainly inter-area frequency deviation

iii) Generator damage under load deviation stress

iv) Voltage instability

On the other hand, a well-managed renewables integration increases the resiliency and reliability of the system. Taking advantage of the renewables low inertia and fast response, we can control the system's power system response to fault occurrence. By utilizing renewables in power systems such as energy storage, generation sources need not be ramped up or down but can instead be run at optimal efficiency while energy storage accounts for variations in the demand. In addition, BESSs can improve the reliability of supply during peak load periods, and BESSs can react to grid demand variations nearly instantaneously. BESSs also have the capacity to function over longer durations with a wide range of storage and power capacities [1][2]-[4].

1.3. Intellectual Merit

This research focuses on battery integration into the power system and its potential to enhance the power system resiliency and reliability. In this regard, two important approaches have been taken; tariff modification for small-scale renewables integration to the power system by taking advantage of the small-scale battery; and employing the large-scale battery in transmission level as a fast response control system to inject/absorb

deficit/surplus power to maintain system stability. In this subject, sensitivity analysis has been done to highlight the most significant factors that can serve the research purpose.

1.4. Broader Impacts

This dissertation is expected to impact electricity customers by helping them to select the optimum renewable and battery size to serve their requirements, and utilities to have a clear assessment of future power grid in their trattorias to define and impose proper tariffs for each sector to improve their services without compromising the system reliability or their customer satisfaction. Third-party renewable owners will benefit from this research to evaluate the potential investment opportunities in both distribution and transmission levels.

CHAPTER TWO

SMALL-SCALE BATTERY INTEGRATION TO THE DISTRIBUTION SYSTEM

2.1. Introduction

Distributed energy resources (DERs), especially battery energy storage systems (BESS), are one of the best solutions to overcome power shortage even if the grid is disconnected momentarily. In recent years, utilities have been offering incentive programs and rebates to encourage their customers to install solar photovoltaic (PV) panels and battery storages on their properties. Batteries are fast-growing among the other renewables due to their multi-objective functionality. Battery energy storages provide both power injection and absorption into the power grids and have a very fast response time [3]-[4]. A well-managed renewables integration to the power systems leads to a more reliable power delivery and enhances the performance and power quality [5]-[7]. By employing the DERs in power grids, billions of dollars can be cut out of the investment to renovate or upgrade the power system. It is shown that the optimal integration of the DERs to the power grid can reduce the peak to the average ratio (PAR) in the power system [8]-[10]. Also, DERs integration to the power grid will minimize power loss [11] and enhance the power grid characteristics such as power quality [12], system resiliency, and stability [13]. However, unstudied DERs integration to the power grid, especially the small-scale renewables with high penetration level, can cause serious frequency, voltage, and thermal issues in the distribution system [14]-[16]. Renewables connection to the power grid, especially in the distribution level, will change the feeder loading profile which results in changes in voltage profiles including

voltage rise and unbalance, frequent operation of load tap changers (LTCs), line voltage regulators, and reactive power flow as a result of voltage regulation activities [17]- [18]. Other adverse effects of the renewables integration to the power grid can be summarized as overcurrent and overvoltage protection [19], including mis-operation of overcurrent protection equipment and temporary overvoltage in the feeders, higher active and reactive power losses during the relatively large reverse power flow [20] and reliability and operation of the power system. Moreover, due to the application of power electronic converters/inverters to integrate the renewables to the power grid, harmonics are produced and injected into the power system [14],[16].

With the approximate 50 percent share in the electricity demand market, the residential and small commercial sectors play a substantial role in the future power grid development road map. This role will be intensified in the presence of the electric vehicles (EVs) in the future power grid. Considering the large number of residential and small-scale commercial customers, and their market share in electricity consumption, to implement the small-scale renewables in those customers' premises, a comprehensive study is required, particularly on battery sizing, price, and optimum exchange of the power to reduce the cost of DERs integration for both utilities and customers.

Many demand-side managements (DSM) techniques have been identified in [9],[10], [18]-[22]. Some of these techniques are the load priority techniques [21], [22], the end-use appliances control techniques [10], [19], the load shifting and valley filling techniques, and the tariff [21], [22]. As one of the demand-side management strategies, electricity tariffs are used to modify electricity consumers' behavior. Smart electricity tariffs highlight

critically important hours of a year by introducing an extremely high rate to limit the demand within the network capacity [23]. It has been shown that the price of electricity by itself does not show a significant impact on electricity consumption [24]-[25]. However, it can play a significant role in adapting the consumers' electricity consumption behaviors in the presence of battery energy storage systems and electric vehicles [26]-[27].

In the majority of existing literature, a battery is sized based on load shaving [28], [29], and frequency control [30]-[31] in the power grid. Battery sizing and its integration to the distribution have been studied to minimize the electricity cost for the customer without paying deserved attention to the distribution system [28], [29]; or for load shaving and frequency regulation in the power grid without considering the customers' interest [30], [31].

2.2. Problem Statement

Considering that battery size directly affects the load profile, we need to find an optimum size of the battery by considering both sides' (customers and utilities) interests. In this regard, our main objective in this section are:

i) to propose the optimum size of the small-scale battery considering the customers' and utilities' interests;

ii) to study the potential effect(s) of the renewables on a distribution feeder;

iii) to investigate the sensitivity of the new load profile to the tariff modification and battery characteristics;

iv) to propose novel tariffs to improve the power quality such as voltage profile and frequency deviation in the power system.

To evaluate the effect of the small-scale renewables' integration on the power system, especially on the distribution system, we need to start our study from the end-users. For this purpose, a residential household employing solar panels, electric vehicles, and stationary batteries in their house (Fig. 4) is chosen as our case study model. The solar panels generate electricity to be used at home, and the surplus can be stored in the batteries (EV and the stationary battery) or sold back to the power grid. Double arrows represent the battery and EV, to emphasize that they can be the consumer or supplier of electrical energy to the home/power grid depending on their states of charges (SOCs). The total energy exchange between customer and power grid, P_G, is measured in the point of delivery (POD). P_G is also considered as customer's new load profile from the power system's perspective. The customer's load consumption data and solar output power is provided from the EPRI website [32].

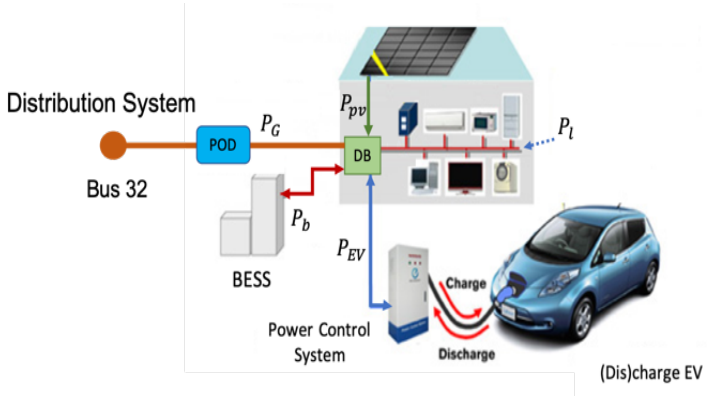

Figure 3. Schematic of residential load connected to the grid in the presence of the renewables

EV's daily trip is modeled by an imaginary load which simulate the EV's battery state of charge deviation during the trip. The case study customer's load consumption, solar output and EV virtual load for a residential house are shown in Fig. 4. For the sake of simplicity, we assume that EVs can connect to the grid for charging or discharging purpose just from home.

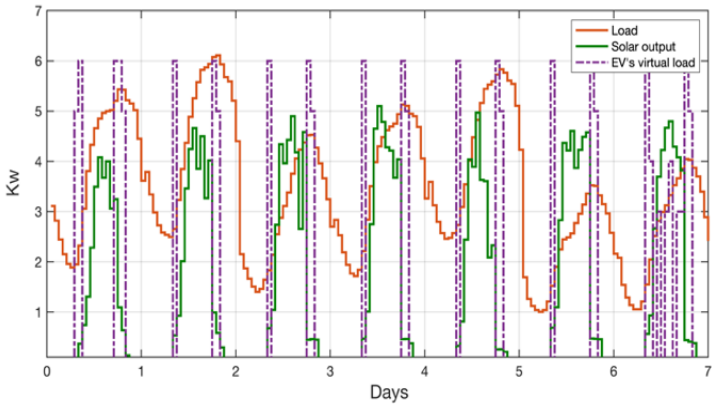

Figure 4. Original load, solar output and EV's virtual load

In the next step, to evaluate the effect of the high penetration level of the renewables on the distribution system, the IEEE 123 node feeder (Fig. 5) is considered as the case study feeder in which 30 percent of the residential customers are willing to employ renewables in their premises. This feeder is a 4.16 kV, relatively short (~7.5 circuit miles total) feeder, adapted to serve 650 customers with a peak load of 4 MW. The feeder includes the common characteristics that are installed in real networks. Based on the results from the individual customers' optimization, we will investigate the power loss and voltage deviation of the feeder.

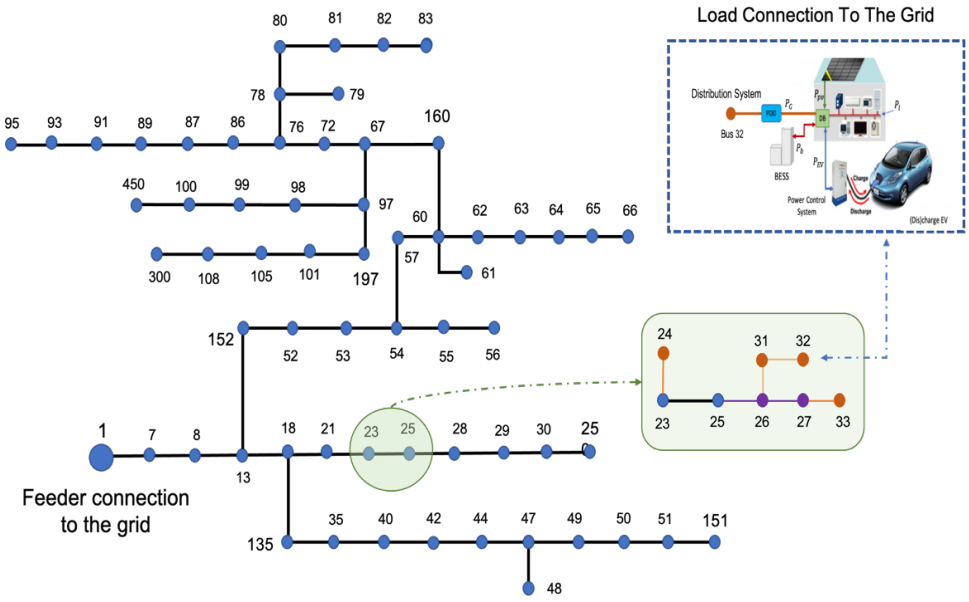

Figure 5. Schematic of case study distribution feeder (IEEE 123 node)

2.3. Battery Sizing

Battery sizing is a challenging subject, and it depends on the renewables and battery storage penetration level in the power grid [9], [17]. Customers with large batteries will be able to sell more power to the grid, which is not necessarily beneficial for utilities in a renewable rich power grid. To prevent over-estimating the battery's size, we use the Zero Net Energy (ZNE) building policy in which customer and utility have zero net energy exchange.

To calculate the stationary battery's size, we exclude the electric vehicle from calculation. We consider load consumption and solar output at each hour of the day as a random variable with 108 samples (54 weeks' data consisting of minimum and maximum load information). A probability density function (PDF) is derived for each hour. Using the PDF

function, we can form the statistical distribution for the power consumption (load) of our case study to calculate an upper and lower boundary for the load. To avoid over-estimating the battery's size, we consider upper and lower bounds for load consumption and PVs' output for specifically given expected values. A maximum and minimum expected limit for power consumption is considered using the obtained probability distribution based on a given reliability margin. In this study, the expected value is considered 85 percent.

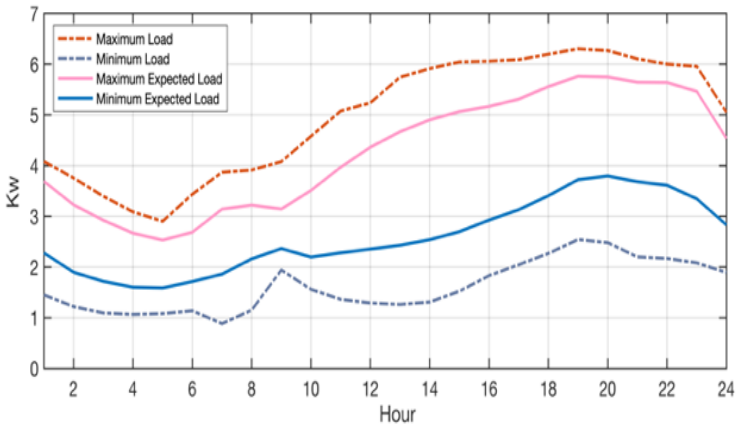

Figure 6. Maximum and minimum load consumption profile

Upper and lower expected load consumption for the given expected value are shown in Fig. 6. Similar maximum and minimum expected limits are defined for solar generation, and the results are depicted in Fig. 7. A battery is sized based on the customer's expected reliability level. For the defined maximum expected load consumption and minimum expected solar output, reliability of the battery performance will be 80 percent for this case study, which is calculated based on $P\left({P_l}^t \geq P^t_{l_{max-e}}\right)$, the probability of load consumption being higher than the maximum limit, and $P(P^t_{pv} \leq P^t_{pv_{min-e}})$, the probability of solar output being lower than the minimum limit. The 80 percent reliability of battery means that

in any circumstances of load consumption and solar panel output, 80 percent of the time, the battery will provide the household load consumption demand.

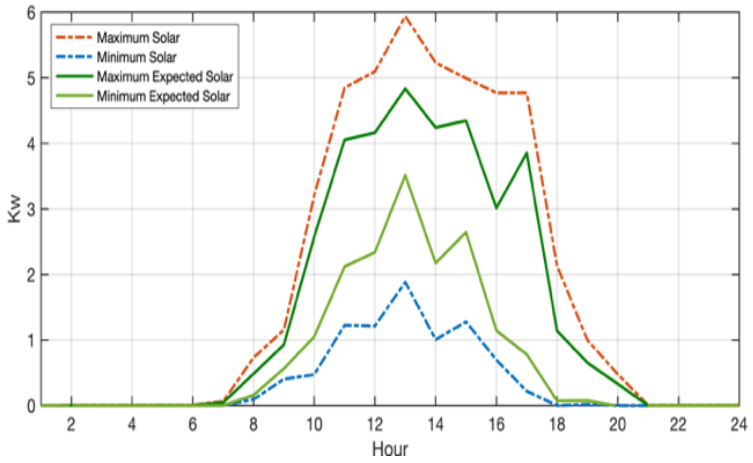

Figure 7. Maximum and minimum solar generation

Considering the ZNE policy, the objective function is defined such that the power exchange between the power grid and customer be equal to zero. Battery capacity (C_b) is also added to the objective function to achieve the battery's minimum size. Objective functions and constraints stated as

$$J_{BESS} = min(\psi . \sum_{t=1}^{24} \|P_G^t\|_2 + C_b) \quad (1)$$

$$P_l{}^t = P_{l_{max-e}}^t \quad (2)$$

$$P_{pv}^t = P_{pv_{min-e}}^t \quad (3)$$

$$-P_{d\_b}^t \leq P_b^t \leq P_{c\_b}^t \quad (4)$$

$$P_G^t = P_{pv}^t - P_l{}^t + P_b^t \quad (5)$$

$$soc_b^{t+1} = soc_b^t + (P_b^t * \Delta t / C_b) \quad (6)$$

P_l, P_{pv}, and P_b are load consumption, solar output and battery (dis)charge power respectively and $P_{c\_b}^t$ and $P_{d\_b}^t$ represent the upper and lower limits for the stationary battery charge and discharge power and ψ is a weighting factor to push exchanged power to zero. Considering the maximum (dis)charging power of 5 *kw* for the battery, the optimum battery capacity for the case study customer is calculated as 30 *kwh*. For the rest of the study we will consider the above-mentioned data, and an electric vehicle battery capacity of the 75 *kwh* with 6 *kw* charge/discharge power.

2.4. Battery Integration to the Distribution System

Considering the optimum size of the battery, in order to study the effect of the renewables on the exchanged power between the consumer and power grid at POD, tariff policy is required. We consider three different rating policy to evaluate the effect of the small-scale battery integration on the power system. Also, to assess the effect of a higher level of renewables penetration in the distribution system, we assume that the 30 percent of customers connected to the case study feeder are willing to employ renewables in their house. The optimization is formulated for one month and the results are shown for one week to be traceable.

2.4.1. Time of Use (TOU) Electricity Rate

In the time of use rating policy, customers pay a higher rate for their electricity consumptions during the peak time compared to the off-peak time during the week and weekends. Also, the charge and discharge rates for the EVs are similar to the rest of the

loads. We consider that the EV is connected to the grid from home. This connection is limited to specific time during the night from 8:00 pm till 6:00 am.

The optimal electricity consumption price is formulated as the following objective function

$$J_{TOU} = min\ [\sum_{t=1}^{T} P_G^t . R^t] \quad (7)$$

where, P_G^t is the exchanged power between the customer and power grid at POD, and R^t is the energy consumption rate. R^t has two values of R_p =6.6 $\mathcal{C}/kwh$ for peak hours (1pm-7pm) and R_{op} =5.4 $\mathcal{C}/kwh$ for off-peak hours. The exchanged power equation is:

$$P_G^t = {P_l}^t - P_{pv}^t + P_b^t + P_{ev}^t + P_{L\_EV}^t \quad (8)$$

Where P_{ev}^t is the (dis)charging power for EV and $P_{L\_EV}^t$ is the virtual load which defines the EV's monthly trip profile. T is the optimization horizon such as daily, monthly, or yearly duration. In this study we consider *T=720* for one-month study with $\Delta t = 1h$ optimization time interval. The optimization in (7) is subjected to the following constraints:

$$-P_{d\_EV}^t \leq P_{ev}^t \leq P_{c\_EV}^t \quad (9)$$

$$-P_{d\_b}^t \leq P_b^t \leq P_{c\_b}^t \quad (10)$$

$$soc_b^{t+1} = soc_b^t + (P_b^t * \Delta t / C_b) \quad (11)$$

$$0.1 \leq soc_b^t \leq 0.9 \quad (12)$$

$$soc_b^1 = soc_b^T \quad (13)$$

$$soc_{ev}^{t+1} = soc_{ev}^t + (P_{ev}^t * \Delta t / C_{ev}) \quad (14)$$

$soc_{ev}^t \geq 0.5$ at t=7:00 am and

$soc_{ev}^t \geq 0.5$ at t=5:00 pm (15)

$$0.1 \leq soc_{ev}^t \leq 0.9 \quad (16)$$

$P^t_{c\_EV}$ and $P^t_{d\_EV}$ represent the upper and lower limits for the EV's battery. C_{ev} is the total battery capacity in EV. soc^t_{ev} represents the state of charge for the EV's battery which should stay between 10 and 90 percent to satisfy given constraint in (7) at all time. The state of charge of the stationary and EV batteries should be similar at the beginning and the end of the month. Also, to satisfy minimum state of the charge for morning and afternoon trips of the EV, the battery of EV must have at least 50 percent charge at 7:00 am and 5:00 pm.

The optimization results for the exchanged power between the customer and distribution system is shown in Fig. 8. It is shown that the exchanged power between the customer and the distribution system has been increased by 250 percent. Distribution system experience two positive peaks before and after peak time and one negative peak during the peak time; also, sudden deviations occurs under TOU policy in the presence of the batteries.

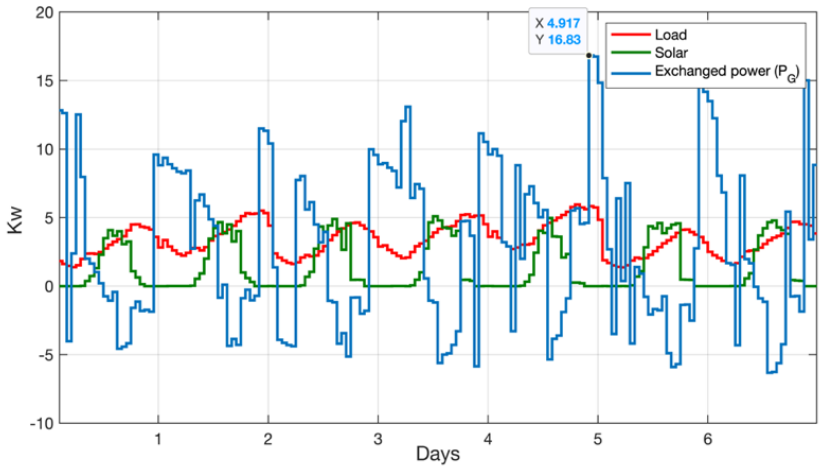

Figure 8. Exchanged power profile at POD in TOU rating policy

Load profiles are for the EV and stationary batteries are presented in Fig. 9. Both batteries taking the advantage of the electricity rate difference between the peak and off-peak time

to charge and discharge up to their maximum capacity to minimize the cost function.

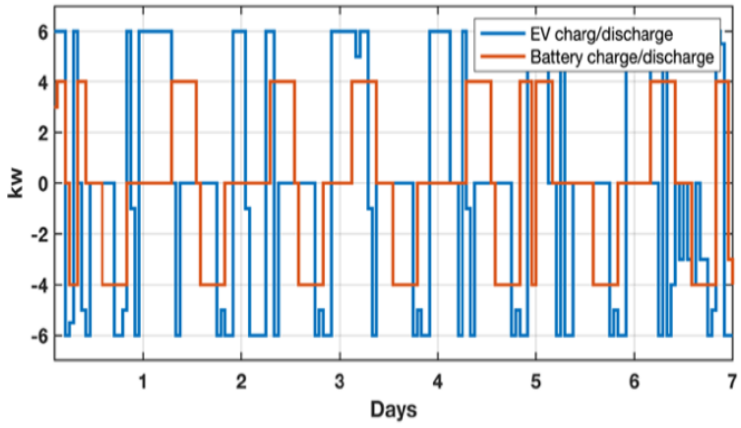

Figure 9. Stationary and EV batteries (dis)charging profile in TOU policy

2.4.2. Maximum Demand (MD) Electricity Rate

In maximum demand rating policy as formulated in (17), customers should pay additional fee for their maximum electricity demand during the bill rendering period in addition to their energy consumption price.

$$J_{MD} = min\,[(\sum_{t=1}^{T} P_G^t . R^t) + \lambda\,.\,P_{Gmax}] \quad (17)$$

$$P_G^t = P_l{}^t - P_{pv}^t + P_b^t + P_{ev}^t + P_{L\_EV}^t \quad (18)$$

P_{Gmax} is the maximum exchanged power between the customer and distribution system at POD, $\lambda = 300\ \mathcal{C}/kw$ is the maximum demand fee and optimization results are presented in Fig. 10 and Fig. 11 for exchanged power and batteries' load profile.

The maximum exchanged load under MD rating policy is less than the original load, however, negative power flow and sudden changes in load still are serious issues. Batteries in this case charge/discharge so that the maximum exchanged power stays at lowest possible rate in order to minimize the customers' total bill.

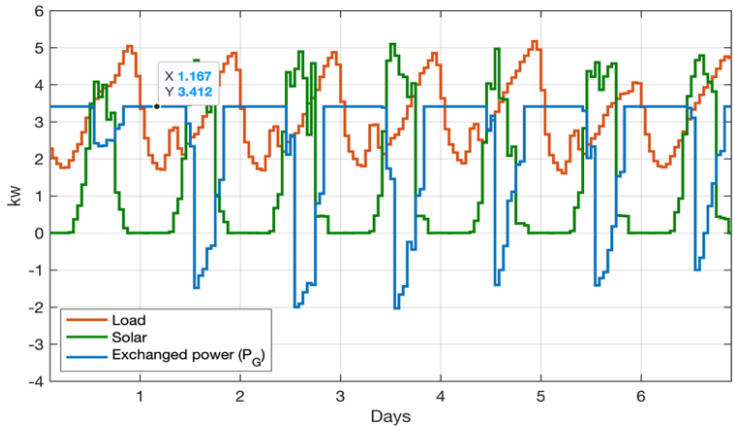

Figure 10. Exchanged power profile at POD under MD rating policy

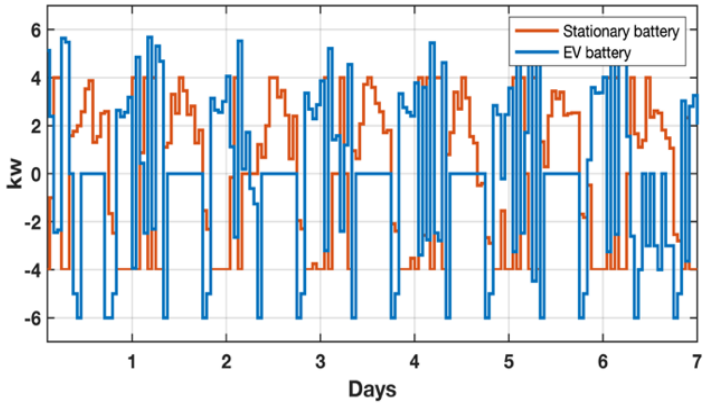

Figure 11. Stationary and EV batteries (dis)charging profile under MD rating policy

Comparing the results in Figs. 8- Fig.11 indicate that TOU policy causes higher positive and negative peak, almost twice of the original load peak. In distribution feeders with a higher penetration level of the renewable integration, the new peak can exceed feeders' capacity. Also, as a result of reverse power flow, distribution feeders which are designed for one-way power flow from generation toward end use customers, experience overvoltage and thermal issues. Moreover, sudden load deviation mainly in higher voltage level will cause large power flow in transmission level and frequency deviation in the power grid. MD can be considered as the best rating policy among all three tariffs, based

on load profile results, which force batteries to charge and discharge such that the exchanged power decreases to minimum possible value. However, power grid still faces two main challenges that should be addressed; sudden load deviation and negative power flow. To propose an adequate solution, we need sensitivity analysis with regard to the existing variables in the optimization equations.

2.5. Voltage Deviation in Distribution System

Feeder IEEE 123 node is considered as our case study distribution feeder to evaluate the effect of the higher level of renewables' connection on distribution system. The total number of the customers on the feeder is 650 customers and total load demand on the feeder is 3896 *KVA*. We assume that 220 customers (approximately 30 percent) are interested in renewable energy sources.

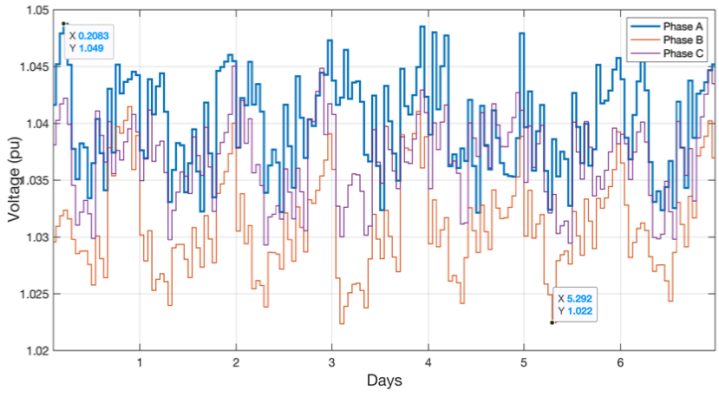

Figure 12. Voltage deviation at bus 67

For the original load consumption profile, the voltage profile in bus 67 (as an example) is depicted in Fig. 12. The average active and reactive power losses of the feeder are during the month are 33.23 *kw* and 66.5 *kvar* respectively where the maximum active and reactive power losses are 72.95 *kw* and 146 *kvar*.

To simulate the effect of renewables connection to the power grid, randomly 30 percent of the customers are chosen to be presented with new load profiles under TOU rating policy as most popular rating policy which has the highest peak in presence of the renewables. The new load profiles will be replaced with the original load profiles. The voltage profile of the feeder considering the new load profiles for 30 percent of randomly chosen customers is depicted in Fig. 13. The new load shapes cause more voltage deviation also the maximum voltage increase from the standard limit. The average active and reactive loss are 37.67 *kw* and 74.5 *kvar* respectively. The maximum active power loss is 159.7 *kw* and maximum reactive power loss is 317.4 *kvar*. Both average and maximum power losses in the feeder have been increased in results of increased power exchange between the customer and the power grid.

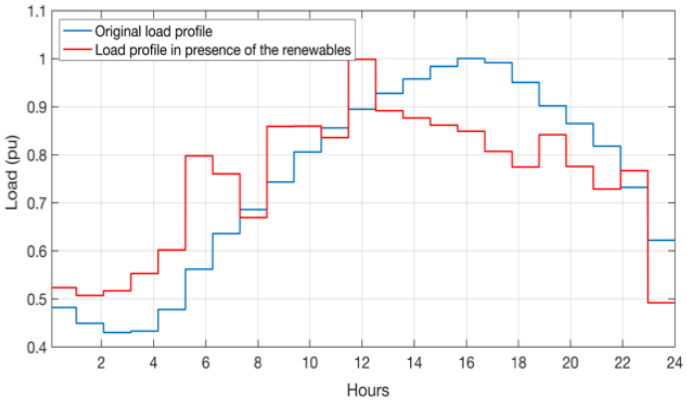

Figure 13. Load profile after 30 percent of renewables' integration in residential sector

Part of this power loss increases are inevitable as we have connected new device to the system to replace gas consumption with clean energy. Comparing the voltage profile in Fig. 12 and Fig. 14 clearly show that the renewables integration will affect the distribution system power quality and the higher penetration level of the renewables will cause serious

voltage issues which needs to be addressed. Voltage deviation under MD tariff with 30 percent renewables stays in standard region, however, the voltage deviation still is an issue [18].

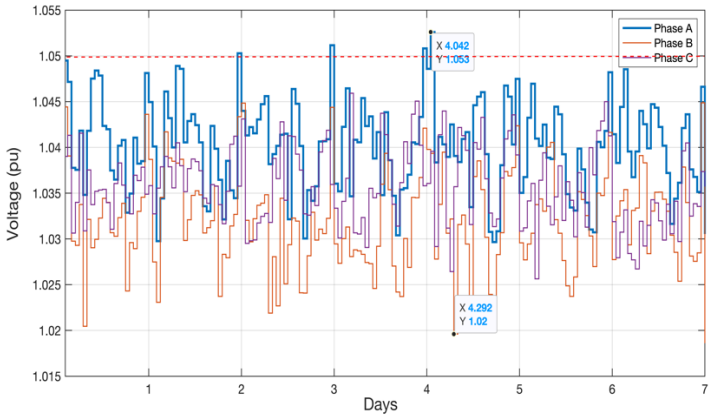

Figure 14. Voltage deviation at bus 67 with 30 percent of renewables connection in TOU policy

CHAPTER THREE

SENSITIVITY ANALYSIS

3.1. Sensitivity to the Tariff Policy

Peak time in electricity tariffs is defined according to the power grid peak load to encourage electricity consumers to shift their consumption away from peak periods. The peak time definition will be highly important in the higher penetration level of renewables, especially solar and batteries. Last year, San Diego Gas & Electric's (SDG&E's) accepted to shift time-of-use peak periods from the solar-friendly hours of 11:00 am to 6:00 pm to the less sunny hours of 4:00 pm to 9:00 pm in result of renewables integration to the power grid [33]. In fact, solar growth forces SDG&E to change its rating policy to reach a better load profile.

3.1.1. Sensitivity to Peak Time Schedule

In this section, we study the sensitivity of the battery (dis)charge and power exchange in TOU policy to one-hour shift ahead or behind in peak time. The results for power exchange between the consumer and power grid for an hour shift of TOU ahead and behind are presented in Fig. 15 and Fig. 16 respectively.

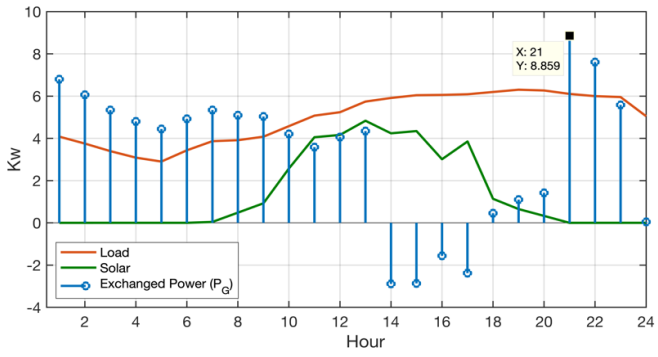

Figure 15. Power exchange in POD for one hour ahead in TOU policy

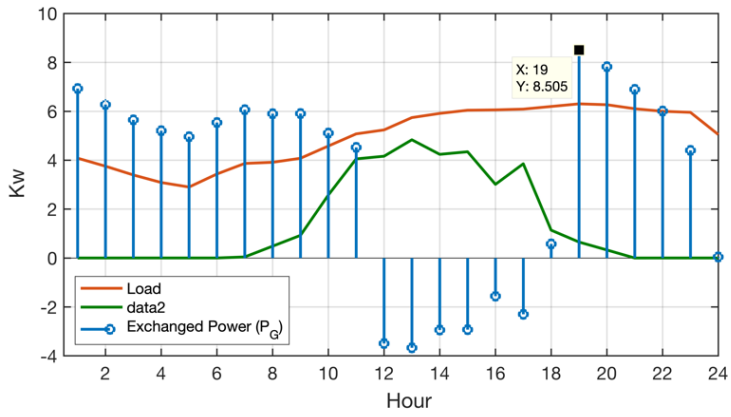

Figure 16. Power exchange in POD for one hour behind in TOU policy

Comparing the results to the original results (Fig.17) indicate that although results for one hour behind is better, in both cases the distribution system still is challenged by the reverse power flow during the peak time and higher peak load immediately after the peak time.

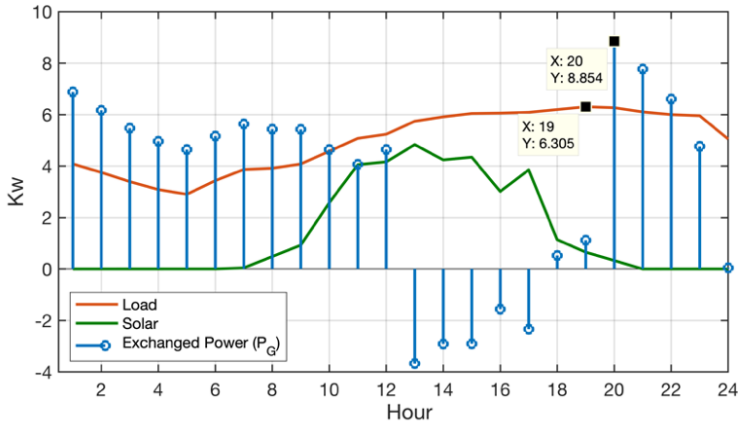

Figure 17. Exchanged power in POD for TOU policy

3.1.2 Sensitivity to the Maximum Demand Rate

It is trivial that the exchanged power is not sensitive to the electricity rating under TOU policy. Maximum demand tariff is sensitive to both rate deviation and time of use schedule; however, it is more sensitive to the MD fee than the energy price. To evaluate the effect of

the maximum demand fee changes in MD strategy, maximum demand fee is increased from 300 ¢/kw to 800 ¢/kw. Figure 18 depicts power exchange profile for the new MD tariff. It is shown that when we increase the maximum demand fee the exchanged power, P_G, decreases.

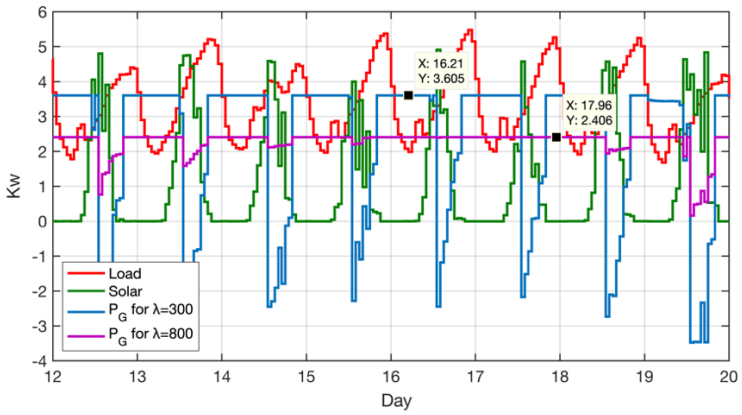

Figure 18. Exchanged power deviation with respect to lambda

To have a precise conclusion and verification of possible saturation point and corresponding value of λ, we run the optimization for different values of λ and plot the maximum exchanged power with respect to λ. Figure 19 shows the evolution of the maximum exchanged power with respect to λ. By increasing the λ, the maximum exchanged power decreases up to a certain level; after the saturation point, further rise in λ has no more effect on the maximum power exchange. The higher MD rate forces customers to charge their batteries and use them during the peak demands instead of selling energy to the power grid during the peak time to reduce their maximum demand. In fact, self-feeding will be more profitable for the customers compared to exporting the stored energy to the power grid during the peak time.

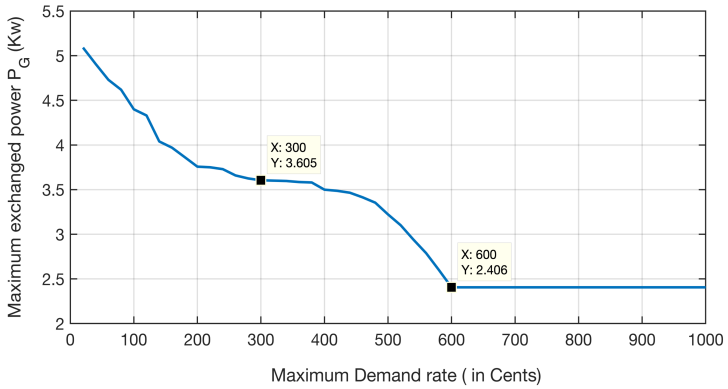

Figure 19. Maximum demand rate effect on P_G

Next, in order to have a better insight on the effect of λ on P_G and evaluate the results, we chose three arbitrary values of λ and showed the result of the optimization in Fig. 20. The results indicate that by increasing the λ, the magnitudes and number of negative $P_G s$ decrease. The saturation point depends on the customer's load consumption behavior and the battery's characteristics [journal].

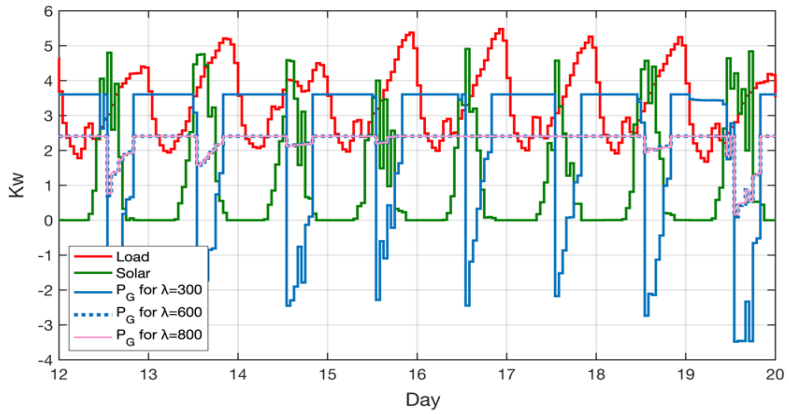

Figure 20. Exchanged power deviation with respect to lambda

3.2. Sensitivity to the Battery Characteristics

In In addition to λ, the parameters of the installed battery in the customer's property should be considered. These parameters affect the exchanged power at POD and consequently

effects the saturation λ. To show the effect of battery characteristics on the exchanged power under MD tariff, two different batteries are considered. The exchanged power formulas for these two cases are defined as:

$$P_{G1}^t = P_{pv}^t - P_l{}^t + P_{b1}^t \quad (19)$$

$$P_{G2}^t = P_{pv}^t - P_l{}^t + P_{b2}^t \quad (20)$$

where, $P_{G1}^t$and P_{G2}^t stand for power exchange for battery number 1 and battery number 2, respectively. Battery charging/discharging power for each battery is indicated by P_{b1}^t , and P_{b2}^t. Let us define J_1 and J_2 to be the optimum value of the cost function (17) for the two choices of the battery, correspondingly. To have $J_2 = J_1$, the following should be true:

$$\sum_{t=1}^{T} P_{G2}^t . R^t + \lambda \, . \, max(P_{G2}^t) = \sum_{t=1}^{T} P_{G1}^t . R^t + \lambda . max(P_{G1}^t) \quad (21)$$

which is equivalent to:

$$\sum_{t=1}^{T} (P_{G2}^t - P_{G1}^t) . R^t + \lambda \, . \, (max(P_{G2}^t) - max(P_{G2}^t)) = 0$$

Substituting the value of $P_{G1}^t$and P_{G2}^t from (13)-(14), we have

$$\sum_{t=1}^{T} (P_{pv}^t - P_l{}^t + P_{b1}^t - P_{pv}^t + P_l{}^t - P_{b2}^t) . R^t$$

$$+ \lambda \, . \left(max\left(P_{pv}^t - P_l{}^t + P_{b1}^t\right) - max\left(P_{pv}^t - P_l{}^t + P_{b2}^t\right)\right) = 0$$

Then,

$$\sum_{t=1}^{T} (P_{b1}^t - P_{b2}^t) . R^t + \lambda \, . \, (max(P_{b1}^t) - max(P_{b2}^t)) = 0 \quad (22)$$

Considering R^t to be the same value for both cases, (22) consists of three sets of variables: the maximum demand rate (λ), the term $\sum_{t=1}^{T}(P_{b1}^t - P_{b2}^t)$, which is related to the capacity difference of the two batteries, and $(max(P_{b1}^t) - max(P_{b2}^t))$.

To evaluate the effect of battery capacity, we run optimization in (17) for three different sizes of battery. We consider the original battery with capacity of 30 kwh and $P_b = \pm 5\ kw$ used for optimization in section III as our baseline. The other two batteries are selected as follows

B_1= 20 kwh, and $P_b = \pm\ 5\ kw$

B_2= 30 kwh, and $P_b = \pm\ 5\ kw$

Figure 21 displays the optimization results.

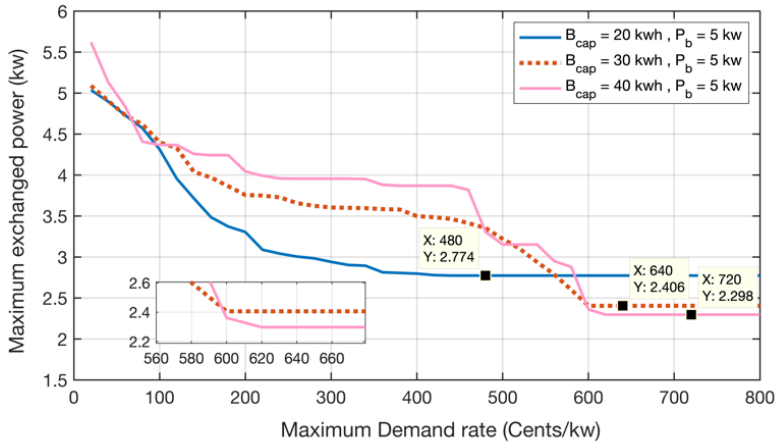

Figure 21. MD rate and exchanged power variation due to battery capacity

Batteries with different capacities and same charging/discharging power have different saturation points for the MD rate. For instance, for a particular value of maximum exchanged power, the battery with a larger capacity has a higher maximum demand fee rate. In other words, increasing the battery capacity leads to a higher saturation value for

λ. Moreover, with a higher battery capacity for a given λ, the maximum exchanged power is lower, and consequently more feeder capacity will be released by this rating policy.

In the second step batteries are considered to have the same capacities as the bassline but different charging/discharging rates as

B_1= 30 kwh, and $P_b = \pm 4\ kw$

B_2= 30 kwh, and $P_b = \pm 6\ kw$

Figure 22 shows the effect of the P_b variation on the maximum demand rate curve with respect to lambda. Different rates of the P_b show slight changes on λ, and P_G comparing to the battery capacity. Also, after a certain level, $P_b$variation has no effect on P_G.

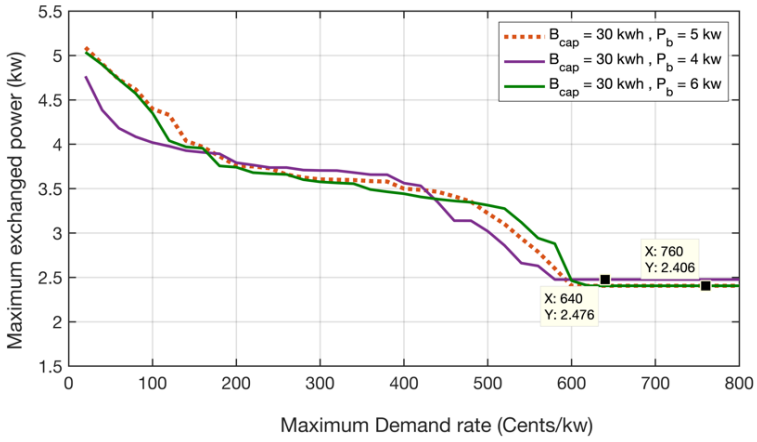

Figure 22. MD rate and exchanged power variation due to battery (dis)charging rate

3.3. Sensitivity to Battery Pack's Efficiency

Our goal in this section is to investigate the effect of the stationary battery's performance on the load profile optimization; without loss of generality, we consider an ideal model with 100 percent efficiency for the PV and electric vehicle's battery operations. To study the effect of the battery performance on its contribution to the demand side load

management, we focus on main factors affecting the battery's performance including (dis)charging efficiencies (round-trip efficiency), self-discharging, and depth of discharge of the battery. Then, we analyze the effects of these parameters on the demand management of the customers connected to the power grid.

3.3.1. Round-Trip Efficiency and Self-Discharging Efficiency Modeling

The exchanged power between the customer and the distribution system considering the battery's overall efficiency generally is formulated as:

$$P_G^t = {P_l}^t - P_{pv}^t + \left(\eta_{b\_c} P_{b\_c}^t - \left(\frac{1}{\eta_{b\_d}}\right) P_{b\_d}^t\right) + P_{ev}^t + P_{L\_EV}^t \quad (23)$$

Where η_{b_c} and η_{b_d} are the charging and discharging efficiencies of the battery. The state of charge of the battery considering the self-discharge (η_s), for each time interval is defined as

$$soc_b^{t+1} = \eta_s soc_b^t + [\left(\eta_{b\_c} P_{b\_c}^t - \left(\frac{1}{\eta_{b\_d}}\right) P_{b\_d}^t\right) * \frac{\Delta t}{C_b}] \quad (24)$$

The round-trip efficiency of the battery which also is called as battery efficiency is a function of the battery's temperature, charging/discharging rate and normally is between 80-93 percent. In this study, we consider an average of 8 percent self-discharge for the battery with two values of round-trip efficiencies as 80 and 93 percent in our case study [34].

3.3.2. Depth of Discharge and Battery Lifetime

Depth of discharge of the battery is another effective factor on battery lifecycle and behavior in power grid that should be considered. Considering a fixed amount of energy to

be cycled through a battery before it requires replacement, regardless of the depth of discharge for each individual cycle is not correct. The lifetime of the battery highly related to the depth of discharge of the battery and operation conditions. In general, the estimated throughput of the battery is derived from the depth of discharge curve of the battery with respect to the number of cycles to failure provided by the manufacture. To determine the expected life of a battery in the power system, the battery model then sums the Amp hours or Watt hours that pass into or out of the battery and when this value reaches the total throughput calculated for the battery, the battery life is considered used up. Battery manufacturers create their cycles to failure data using specific testing requirements, usually at a constant temperature of 25℃ with the condition that when the battery capacity diminishes to 80 percent of its nominal capacity it is considered dead (see Fig. 23 adapted from [35] and the numbers does not reflect any specific battery brand).

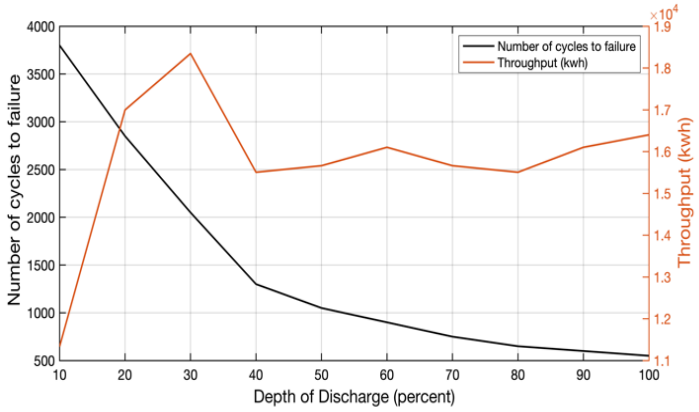

Figure 23. Example of the potential throughput life calculation for a 30-kwh battery with discharges from full state of charge to various depth of discharges.

There are various methods to obtain the lifetime consumption of a battery including the Ah-throughput and cycle counting approaches. In this paper, we use the results of the Ah-

throughput counting method to evaluate the lifetime consumption of the battery. This method considers that a fixed amount of energy can be cycled through a battery before it requires replacement. The estimated throughput, (ρ the total throughput over a battery bank lifetime), is expressed as follows

$$\rho_i = DoD_i F_i C_b \tag{25}$$

in which $\mathrm{DoD_i}$ is the specific depth of discharge being considered, $\mathrm{F_i}$ represents the cycles to failure for the given $\mathrm{DoD_i}$, and $\mathrm{C_b}$ is the nominal battery capacity. In our specific case study that the SOC level of the battery varies between 10-90 percent, and we call it as our **ideal battery** with efficiency of the 100 percent, the average throughput of the battery is calculated as

$$\rho = \frac{\sum_{i=1}^{9} DoD_i F_i C_b}{9} = 15696\ kwh \tag{26}$$

Figure 23 shows that the best performance of the battery occurs in $DoD_3 = 30\%$. For $DoD_3 = 30\%$, the minimum and maximum state of charges of the battery are as follows

$$soc_{min} = (1 - DoD) soc_{max} \tag{27}$$

$$0.7 \leq soc_b^t \leq 1 \tag{28}$$

Simulation results and discussion

Battery efficiency is studied for TOU and MD rates based on given cost function in in (7) and (17) are subjected to the following additional constraints:

$$soc_b^{t+1} = \eta_s soc_b^t + [\left(\eta_{b\_c} P_{b\_c}^t - \left(\frac{1}{\eta_{b\_d}}\right) P_{b\_d}^t\right) * \frac{\Delta t}{C_b}] \tag{29}$$

$$soc_{min} = (1 - DoD) soc_{max} \tag{30}$$

$$soc_{min} \leq soc_b^t \leq soc_{max} \tag{31}$$

Since the focus of this study is the effect of the stationary battery's efficiency on the exchanged power between the customer and the distribution system, the efficiency of the EV's battery is considered 100% and we will not impose other additional constraint on that.

To evaluate the effect of the battery efficiency and optimal depth of discharge on the customer's load profile, in the first step, we consider the effect of each factor on the load profile separately. Next, we study the effect of all factors on the load profile in combine and compare the results to the so-called ***ideal battery*** performance.

Round-trip efficiency impact on the load profile

To evaluate the effect of the battery's charging/discharging (round-trip) efficiency on the load profile, we consider $\eta_s = 1$. Moreover, we consider same values for the charging and discharging efficiencies. The effect of the round-trip efficiency is studied for the round-trip efficiency's upper and lower boundaries. For this purpose, two values of the 80 and 93 percent for the round-trip efficiency are applied to the optimization as $\eta_{b\_c} = \eta_{b\_d} = 0.8$ and $\eta_{b\_c} = \eta_{b\_d} = 0.93$. The simulation results of the exchanged power at the POD are shown in Fig. 24 and Fig. 25 for the TOU and MD policies, respectively.

The round-trip efficiency doesn't have notable effect on the maximum exchanged power between the customer and the distribution system. However, in both tariffs, the battery throughput energy and optimal value have been changed significantly. In the TOU policy battery with the efficiency of the 80 percent is no longer beneficial for the demand side load management. It is important to note that this result is obtained in presence of the EV battery connection. Similar to the TOU policy, in the MD policy the stationary battery only

participates in the load management to keep the maximum demand in its lowest level. The optimal value in the MD policy has been increased as the battery's energy loss limits the battery's participation in the optimal value minimization process. The results for the battery energy throughput and the optimal values of bills for two tariffs and two values of efficiencies are tabularized in Table 1 and Table 2.

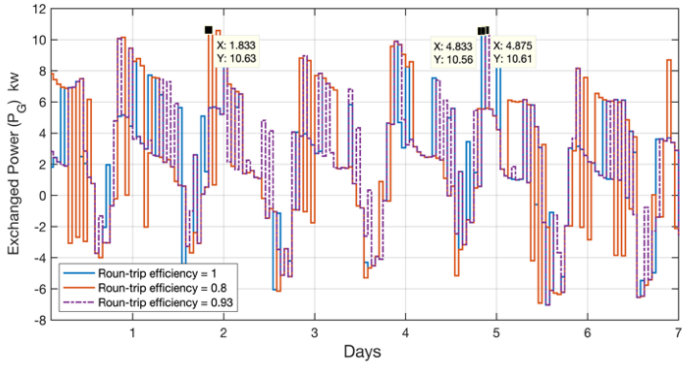

Figure 24. Effect of battery's round trip efficiency on the load profile for the TOU tariff

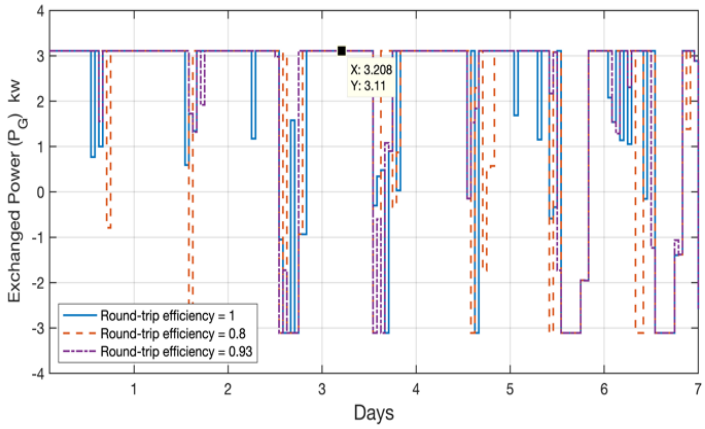

Figure 25. Effect of battery's round trip efficiency on the load profile for the MD tariff

Effect of the battery's depth of discharge on the load profile

The best operating region for the battery is a controversial subject. Different constraint on maximum and minimum state of the charge for the battery are considered in [37] and [38]. In our case study, we consider two scenarios for the depth of discharge in the battery based

on manufacture's data given in Fig. 23. In the first scenario, we consider our so-called "***ideal battery***" with $\eta_s = 1$ and $\eta_{b\_c} = \eta_{b\_d} = 1$. The SOC of the ideal battery is subjected to following constraint

$$0.1 \leq soc_b^t \leq 0.9 \quad (32)$$

For the second scenario, we consider a 30 percent of the depth of discharge limit for the battery with $\eta_s = 1$ and $\eta_{b\_c} = \eta_{b\_d} = 1$. The constraints on the SOC of the battery based on the Fig. 23 is modified to

$$soc_{min} = (1 - DoD)soc_{max} \quad (33)$$

$$0.7 \leq soc_b^t \leq 1 \quad (34)$$

The optimization results for the load exchange between the customer and distribution system are depicted for the TOU and MD tariff policies in Fig. 26 and Fig. 27, respectively. In the TOU policy, the maximum exchanged load has been decreased for $DOD = 30\%$ as the battery does not have the opportunity to fully discharge during the peak time and as a result it needs less power during the off-peak time to be fully charged.

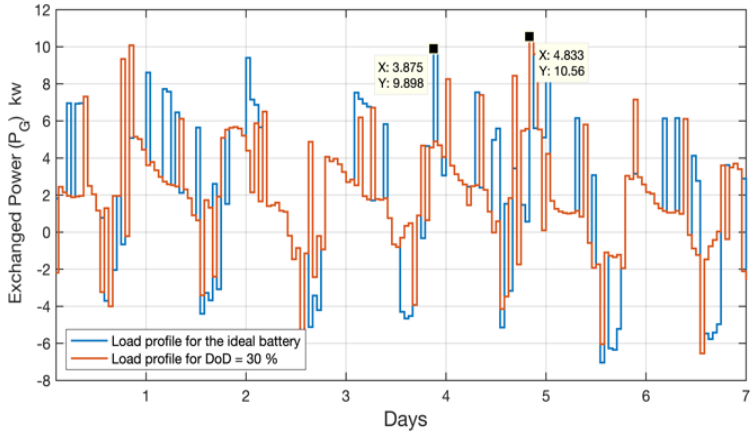

Figure 26. Effect of battery's depth of discharge on the load profile for the TOU tariff

The maximum exchanged power in the TOU has less deviations compared to the ideal battery as the unnecessary charge/discharge of the battery has been reduced due to limited depth of discharge of the battery.

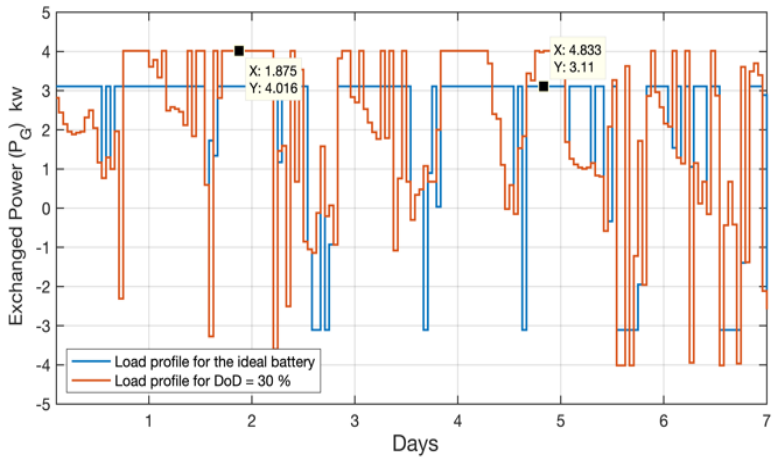

Figure 27. Effect of battery's depth of discharge on the load profile for the MD tariff

In the MD rating policy, Fig. 27, as the battery's total capacity of (dis)charge has been reduced, the battery's participation in the demand management to minimize the maximum exchanged power is not sufficient to maintain the minimum value. The total throughput energy of the battery for a one-month optimization under the TOU tariff are 1380 *kwh* and 736 *kwh* for the ideal battery and the battery with 30 percent DOD, respectively.

Based on given information in Fig. 23, the average throughput energy for the ideal battery and battery with DOD=30 percent during their lifetime are *15696 kwh and 18346 kwh.* The expected lifetime for each battery under the TOU and MD tariffs is:

Lifetime for *ideal battery* for the TOU tariff is $\frac{15696}{1380} = 11.4$ months and

Lifetime for *ideal battery* for the MD tariff is $\frac{15696}{1028} = 15.4$ months

The corresponding lifetime of the battery subjected to DOD=30% are as follow

Lifetime for the battery with *DOD=30%* for the TOU tariff is $\frac{18346}{736} = 25$ months and

Lifetime for the battery with *DOD=30%* for the MD tariff is $\frac{18346}{776} = 23.6$ months

The results show that the battery has a longer lifetime with the limited depth of discharge. Battery under the TOU policy and DOD=30% has the longest lifetime, however, since the difference is less than two months the results can be changed in favor of the MD rating policy with a simple regulation in the MD ratings which is beyond the scope of this paper. Note that the numbers are used for comparison and does not represent any battery brand.

3.3.3. Comparison between the ideal and real battery effects on the load profile

To have a precise evaluation on the battery operation in the demand side load management, all the above-mentioned constraints are applied to the battery in our case study model and the optimization results are compared to the ideal battery. Battery in this scenario is subjected to the following efficiency and DOD constraints.

$0.7 \leq soc_b^t \leq 1$, $\eta_s = 1 - \left(\frac{0.08}{24}\right)$ *and* $\eta_{b\_c} = \eta_{b\_d} = 0.8$

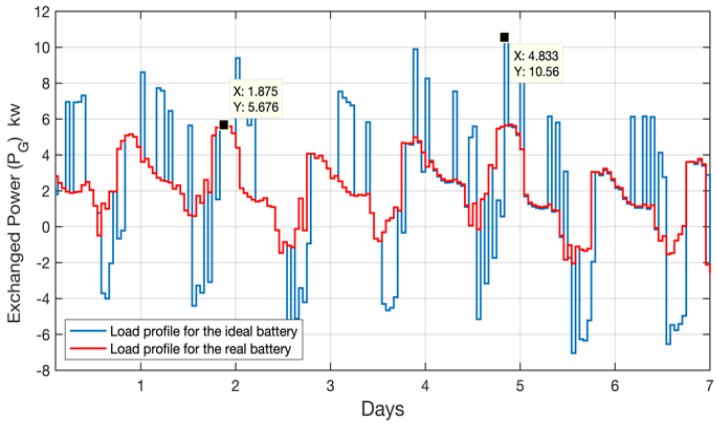

Figure 28. Load profile for the ideal and real battery under the TOU rating policy

Considering all effective factors on the battery's output and participation to the load

management shows a significant decrease in the load exchange between the customer and distribution system for both MD and TOU policies as depicted in Fig. 28 and Fig. 29.

The exchanged power under the TOU policy (Fig. 28) has been decreased compared to the results in Fig. 23. The battery participation under the TOU policy (see Fig. 28) has been decreased. The decrease in the battery's participation occurs due to higher cost of stationary battery participation. Lower efficiency of the stationary battery makes it no more beneficial. The throughput of the battery (68 *kwh*) in this case has been increased compared to case with round-trip efficiency of 80 percent, zero *kwh*, to keep the minimum state of the charge of the battery. Unlike the TOU tariff, the MD policy experiences a notable increase in the exchanged power. In the MD policy, a small increase in maximum demand is more cost effective than the battery's energy losses during the charge/ discharge process. Finally, all the optimization results for a one-month period are summarized in the Table 1 and Table 2 for the TOU and MD policies, respectively.

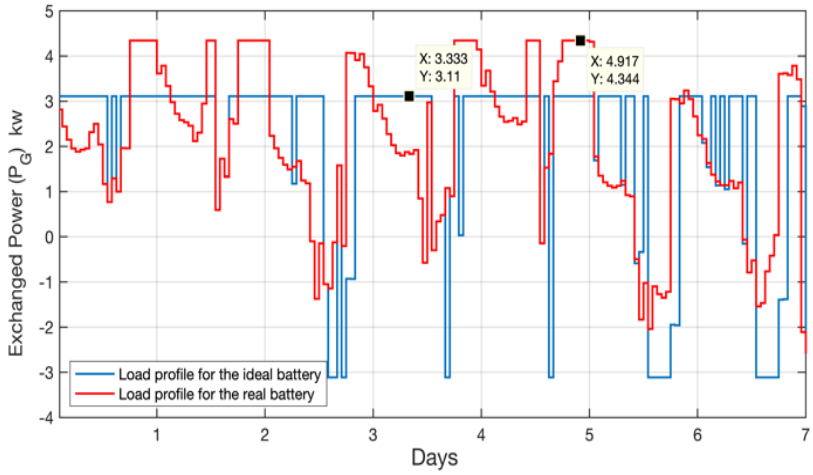

Figure 29. Load profile for the ideal and real battery under the MD rating policy

Table 1. Battery operation under Time of Use tariff

Effective Factor		Maximum Load (*kw*)	Optimal Value/Bill ($)	Total Battery Throughput (*kwh*)
Ideal Case		10.56	69.19	1380
Round-trip Efficiency	0.8	10.63	77.26	0
	0.93	10.61	75.02	1364
Depth of discharge		9.9	70.13	736
Real Case		5.7	76.19	68

Table 2. Battery operation under Maximum Demand tariff

Effective Factor		Maximum Load (*kw*)	Optimal Value/Bill ($)	Total Battery Throughput (*kwh*)
Ideal Case		3.11	98.38	1028
Round-trip Efficiency	0.8	3.11	109.46	580
	0.93	3.11	102.86	1036
Depth of discharge		4.02	103.12	776
Real Case		4.34	112.88	260

The results of this study are beneficial for the battery industry in addition to those customers are interested in employing the battery in their premises to evaluate the effectiveness of their investment. We showed that battery efficiency has notable impact on the optimal exchanged power, however, it does not affect the load profile shape which is

the at most interest of the utilities. Moreover, battery industry can benefit from the results to target the most important factors in the battery efficiency and lifetime required to be improved.

3.4. Inverter Efficiency

Considering the efficiency curve of the inverter as Fig. 29, and battery (dis)charging power rate of $-P_{bmax} < P_b^t < P_{bmax}$, the total battery pack efficiency, η, can be formulated as

$$\eta = \eta_{inv} * \eta_b \tag{35}$$

$$\eta_{inv}=\eta_0 \left[1 - e^{\left(\frac{-\kappa . P_b^t}{P_{bmax}-P_b^t}\right)}\right] \tag{36}$$

Where η_b is the battery storage efficiency and, η_0 is the maximum efficiency of the inverter, κ describes the slip of the curve, and η_{inv} represents the inverter efficiency. Also, the battery SOC will change as

$$soc_b^{t+1} = soc_b^t + [\eta * P_{b-c}^t - (\frac{1}{\eta}) * P_{b-d}^t] * \frac{\Delta t}{C_b} \tag{37}$$

$$P_b^t = P_{b-c}^t - P_{b-d}^t \tag{38}$$

Where $P_{b\_c}^t$, $P_{b\_d}^t$, are the battery's charge and discharge power, respectively. The battery pack has considerably lower efficiency when it (dis)charge with less than ten percent of its maximum (dis)charging power. The inverter efficiency (9) is a nonlinear function, therefore, we use nonlinear optimization's tools to solve this formulated optimization problem.

The objective functions in (7) and (17) are to schedule the charging/discharging profile of the battery to minimize the corresponding electricity bill. Note that the second term in (17)

represents the maximum demand price, which forces the optimization to schedule the battery output in a way that the maximum exchanged power between the customer and distribution system remains in a minimum possible value. Both scenarios consider two battery choices: *(i)* an ideal battery pack; and *(ii)* a realistic battery pack with nonlinear inverter efficiency, as shown in Fig. 30.

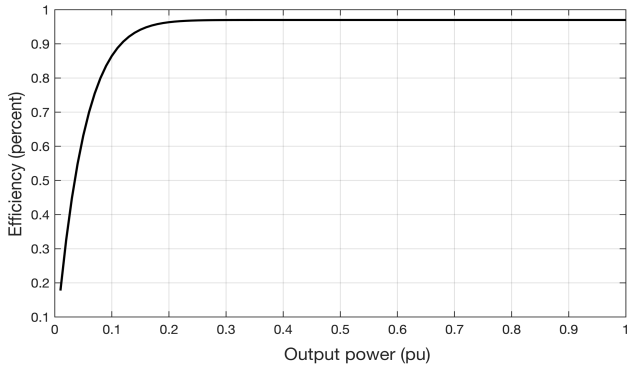

Figure 30. Inverter efficiency curve

3.4.1. Scenario 1: TOU Tariff

The exchanged power between the distribution system and the customer at POD (blue line) and the battery (dis)charging power (red line) are shown in Fig. 31 for an ideal battery. Figure 31 shows that the battery (dis)charge with maximum capacity to maximize the customer's benefit. The exchanged power and battery (dis)charge power for the battery with nonlinear inverter efficiency are represented in Fig. 32, showing the impacts of the real inverter efficiency on battery performance compared to the ideal inverter. The battery with a realistic inverter has a limited (less than fifty percent) contribution in demand-side management to avoid battery power loss due to the inverter's lower efficiency in lower powers. The case study customer's electricity bill, total battery throughput, and the maximum exchanged power for TOU tariff are summarized in Table 3. For a (dis)charge

power less than ten percent of its nominal power, in which the inverter has a considerably lower efficiency, the number of battery (dis)charges shows a significant drop compared to the battery with an ideal inverter. The lower contribution of the battery results in a slightly higher electricity bill and a higher load peak at POD.

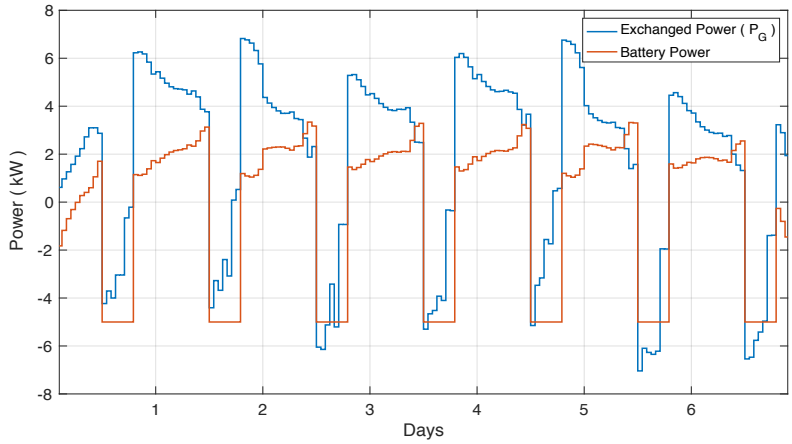

Figure 31. Exchanged power between the customer and distribution system and the battery (dis)charge power for ideal battery pack under TOU electricity tariff

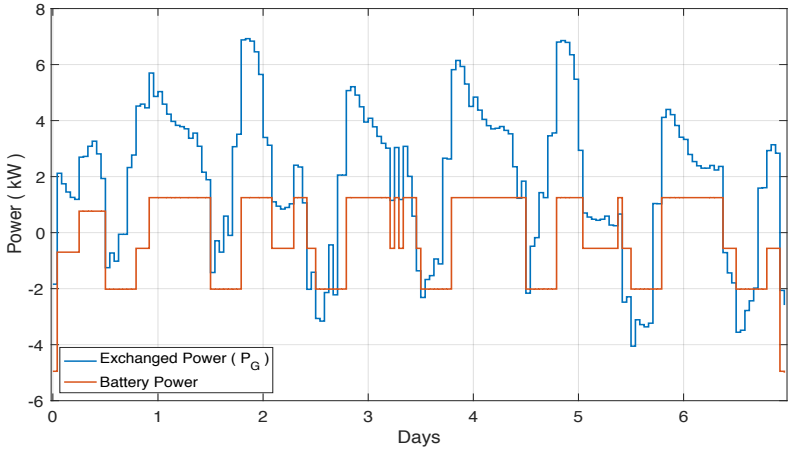

Figure 32. Exchanged power between the customer and distribution system and the battery (dis)charge power for the real battery pack under TOU electricity tariff

Table 3. Impact of the nonlinear inverter efficiency under TOU tariff

	Customer's bill ($)	Throughput of the battery (kWh)	Maximum exchanged power (kw)
Ideal battery pack	56.5	2041	6.7
Real battery pack	69.5	1008	6.9

3.4.2. Scenario 2: MD Tariff

The simulation results for optimization formulated in (17) for an ideal inverter are shown in Fig. 33. A comparison between results in Fig. 33 with Fig. 31 indicates that the battery under MD tariff (dis)charges in lower powers to maintain a minimum exchanged power. Battery operation in lower powers implies higher impact expectation for a real battery application.

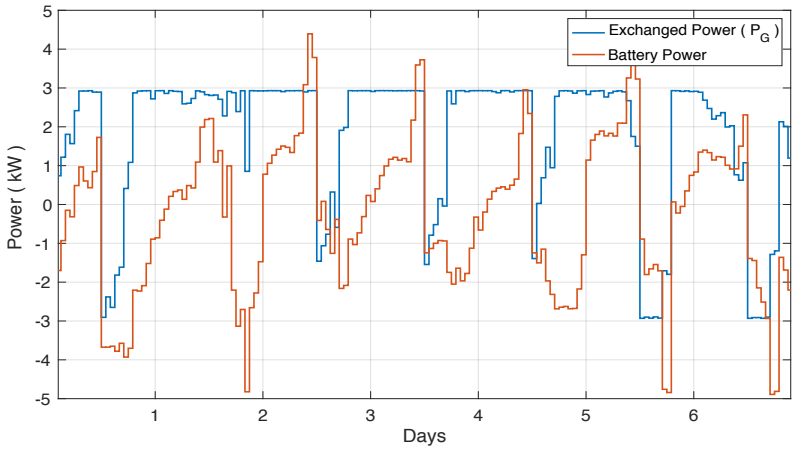

Figure 33. Exchanged power between the customer and distribution system and the battery (dis)charge power for ideal battery pack under MD electricity tariff

Figure 34. shows that the exchanged power for the battery with a non-ideal inverter. Due to the nonlinear inverter efficiency, battery operation in lower powers is no longer beneficial, yet, to minimize the customer bill, battery operation is adjusted to reach the

optimal solution. The impacts of the inverter nonlinear efficiency on the customer's bill and load profile are summarized in Table. 4. The total contribution of the battery has been decreased to maximize the battery efficiency (performance); thus, the maximum exchanged power has been increased.

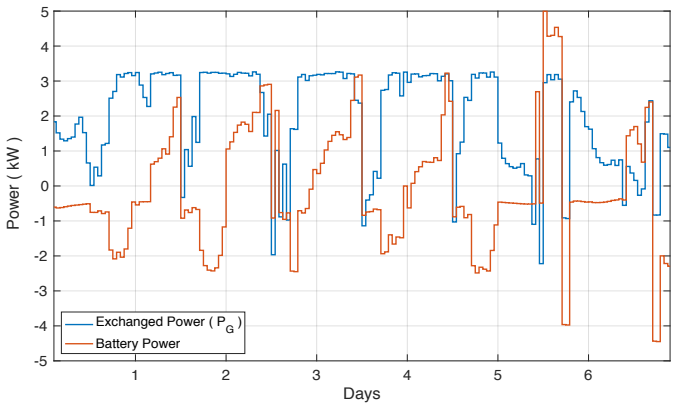

Figure 34. Exchanged power between the customer and distribution system and the battery (dis)charge power for real battery pack under MD electricity tariff

Table 4. Impact of the nonlinear inverter efficiency under the MD tariff

	Customer's bill ($)	Throughput of the battery (kWh)	Maximum exchanged power (kw)
Ideal battery pack	56.5	1188	2.9
Real battery pack	64.8	1004	3.3

There are several approaches to overcome or reduce the negative impact of the inverter efficiency; imposing constraints on the battery's operation point, employing a control system to switch on and off battery operation, imposing new tariff to force battery operate in a limited time to charge with higher power, or choosing a battery pack with a lower (dis)charge power to push the operating point to a higher efficiency spectrum. The former

solutions are not the optimal and will increase the customer's bill; however, the latter case develops a notable improvement in customer bills and battery contribution in the demand-side management. To this end, we choose a real battery pack with twenty percent less (dis)charge power than the original battery pack. The exchanged power under TOU, and MD rating policies for the new battery pack with lower power are shown in Fig. 35 and Fig. 36, respectively. The customer's bill and total battery throughput for TOU and MD are summarized in Table. 5.

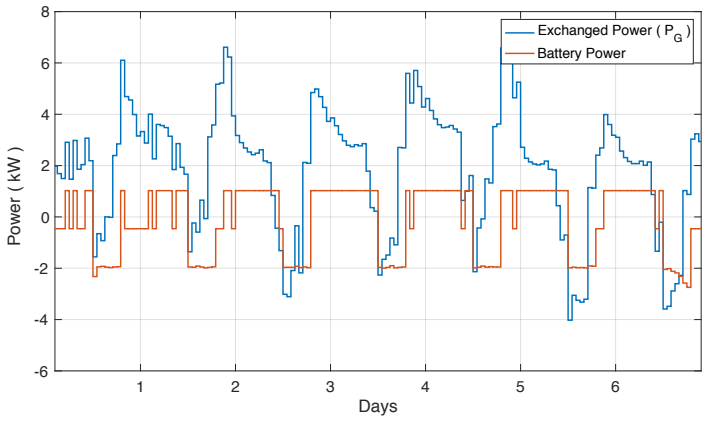

Figure 35. Exchanged power between the customer and distribution system and the battery (dis)charge power for real battery pack with a lower (dis)charge power under TOU electricity tariff

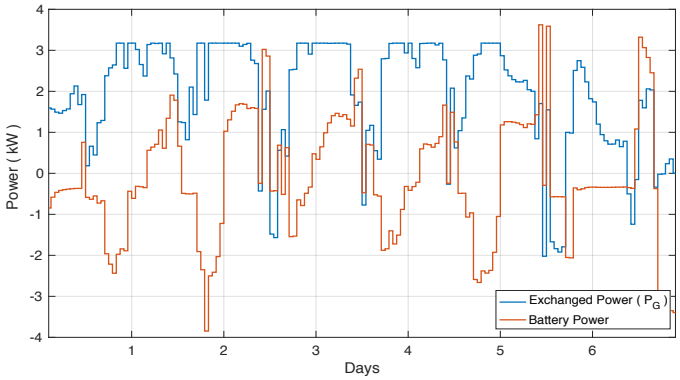

Figure 36. Exchanged power between the customer and distribution system and the battery (dis)charge power for real battery pack with a lower (dis)charge power under MD electricity tariff

Note: in the battery sizing section, we found minimum battery capacity, which could have multiple choices of the battery (dis)charge power.

Table 5 Impact of the nonlinear inverter efficiency with lower battery (dis)charge power

	Customer's bill ($)	Throughput of the battery (kWh)	Maximum exchanged power (kw)
Real battery pack (TOU tariff)	69	898	6.6
Real battery pack (MD tariff)	64.3	882	3.2

CHAPTER FOUR

TARIFF MODIFICATION

4.1. Introduction

To mitigate the negative effect of the distributed energy resources (DERs) connection to the power grid; there are several approaches such as putting limitation on the exchanged power between the customer and power grid. In this subject, [38] proposed to minimize battery and solar size; where [39] suggests employing a larger battery to absorb the PV surplus generation. However, in the residential and small commercial sectors, convincing the customers to plan their power consumption and their renewables connection to the grid will be challenging. The other approach to control the power flow in the distribution feeder is imposing effective tariffs on the power consumption to encourage the customers to change their load consumption behavior based on utilities interest. The new tariffs can be defined so that customers schedule their power consumption, solar panels output and batteries (dis)charging schedule such that they gain highest possible benefit. Meanwhile under new tariffs and in result of customers new consumption schedule; utilities face lower power variation in the system.

Considering sensitivity of the customers' load profiles to current tariffs rate change and battery characteristics [18]-[26], in this section we propose two different tariffs to mitigate the negative effect of renewables' connection to the power grid; in the first tariff, we add a Smoothening Factor Fee (SFF) to limit the load deviation in one of the current tariffs in the POD terminal. In the second proposed tariff, we charge customers based on their maximum

demand and load deviation at POD. We call the second proposed tariff as Maximum Demand Smoothening Fee (MDSF). The optimization for load consumption for these tariffs can be formulated as follows:

$$J_{SSF} = min\left[\sum_{t=1}^{T}\left(P_s^t . F_1^t + P_{c\_ev}^t . F_{EV}^t\right) + \zeta . \Delta P_G^t\right] \quad (39)$$

$$J_{MDSF} = min\left[\lambda . max\left(abs(P_G^t)\right) + \zeta . \Delta P_G^t\right] \quad (40)$$

$$\Delta P_G^t = P_G^{t+1} - P_G^t \quad (41)$$

Where ζ is the SFF and λ is MDSF which are regulated by utilities based on general customer's load profile. These factors can be regulated so that the optimal value for customers have least changes. New optimizations in both new cases are subjected to given constraints in (9) – (16).

4.2. Smoothening Factor Fee Rating Policy

The optimization in (39) is run for the first scenario (TOU rating policy) and the results are presented in Fig. 37.

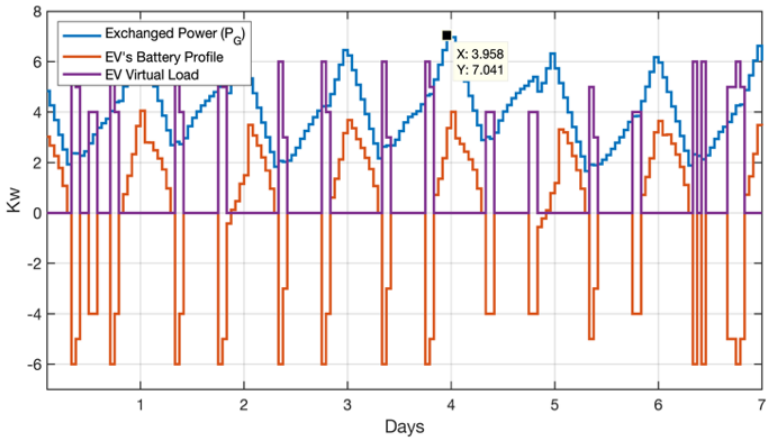

Figure 37. Exchanged power profile in POD and grid under SFF rate

It is shown that in result of the tariff modification; i) maximum exchanged power between the customer and power system has been decreased from 16.5 kw to 7.0 kw and ii) the distribution feeder has positive power flow from the grid to the customer (this occurs in result of load deviation constraint and the positive load flow is not always guaranteed), and iii) the dramatic load variations in POD have been eliminated.

4.3. Maximum Demand Smoothening Fee Rating Policy

In the second case, the optimization defined in (40), is applied to the case study model and the results are depicted in Fig. 38. By tariff modification the maximum exchanged power is decreased from 16.5 *kw* in TOU and 3.6 *kw* in MD and limited to 2.92 *kw*, which is also lower than 5.7 *kw* in the original load profile. Load profile for new tariff is smooth and has lower maximum without any negative power flow.

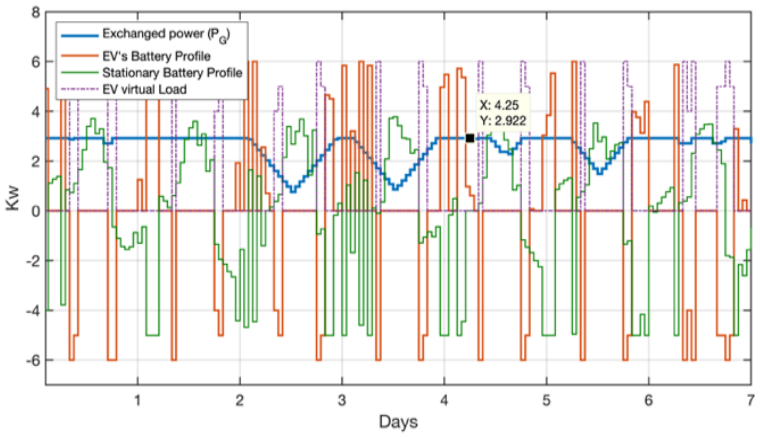

Figure 38. Exchanged power profile under MDSF rate

The main advantage of MDSF tariff to SFF tariff is the lower peak to average ratio (PAR). Lower PAR means lower investment requirement for peak time demand in power system especially in generation and transmission sector. The voltage deviation for SSF and MDSF

tariffs are shown in Fig. 39 and Fig. 40. The average active and reactive power losses for SSF rating policy are 31.15 kw and 62 *kvar* and the maximum active and reactive power are 70.58 *kw* and 141.7 *kvar* respectively which show notable improvement. Also, the average active and reactive power losses for MDSF tariff will be as 30.28 *kw* and 60.6 *kvar*. The maximum active power during the month will be 59.24 *kw* and the maximum reactive power loss is 118.9 *kvar.* As we expected voltage deviation for MDSF rate has the least deviation and power loss is less than the original case.

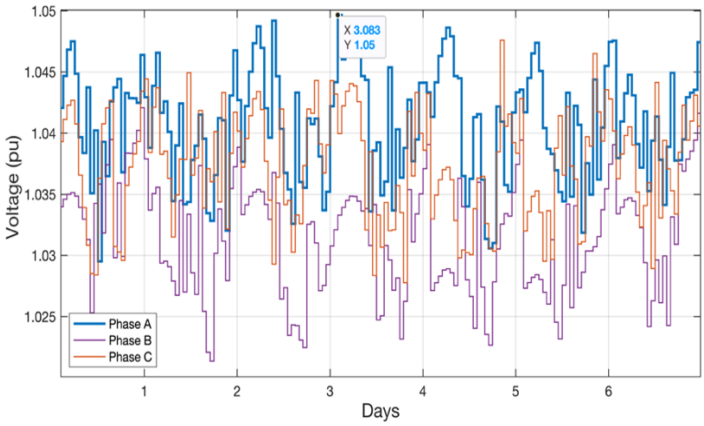

Figure 39. Voltage deviation at bus 67 under SFF modified tariff

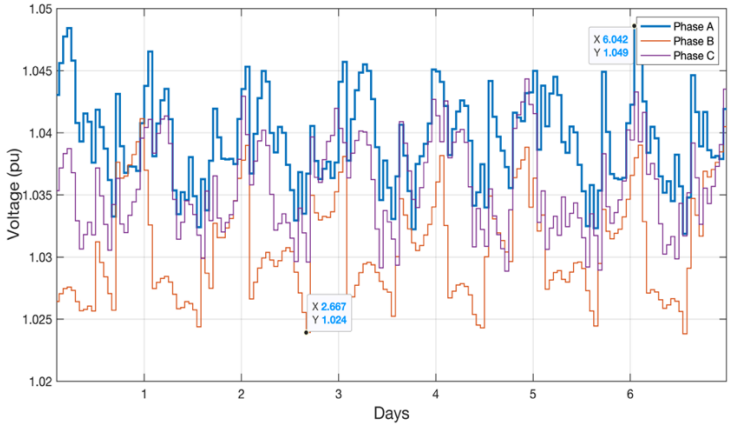

Figure 40. Voltage deviation at bus 67 under MDSF modified tariff

4.4. Frequency Deviation in Small Scale Power Grid

Our microgrid case study model, Fig. 41, is a combined heat and power (CHP) generator. The control system of the generator is designed to regulate the frequency deviation to zero for the microgrid with the original load. The nominal capacity of the generator is considered 10 Mw and ΔP_l represents the load deviation from the original load profile under renewables connection to the power grid. The load deviation is represented in "*pu*" and the frequency deviation is studied for a one-day period for the sake of simplicity. Since the frequency oscillations are damped in less than 100 seconds, we only show the frequency oscillations for the first 100 seconds of every hour of the day.

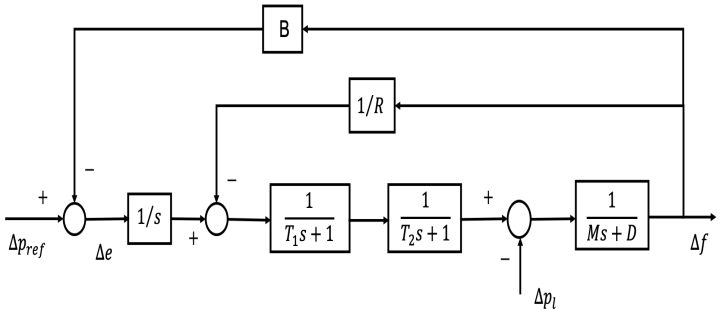

Figure 41. Simplified CHP generator schematic for the case study model

The control system of the microgrid is set so that the maximum deviation of the frequency under the load deviation is less than 0.8 percent ($\Delta\omega < 0.05$) to prevent the frequency breakers' operation. The new load profile under TOU tariff and the original load profile are comparable in Fig. 13. The frequency deviation of the microgrid under original and new load profiles are depicted in Fig. 42. It is shown that the renewables integration under current tariff causes frequency issues which will result in frequency relay operations.

Current tariff, as we expected, is not applicable for future grid and they should be modified based on future grid requirements and architecture.

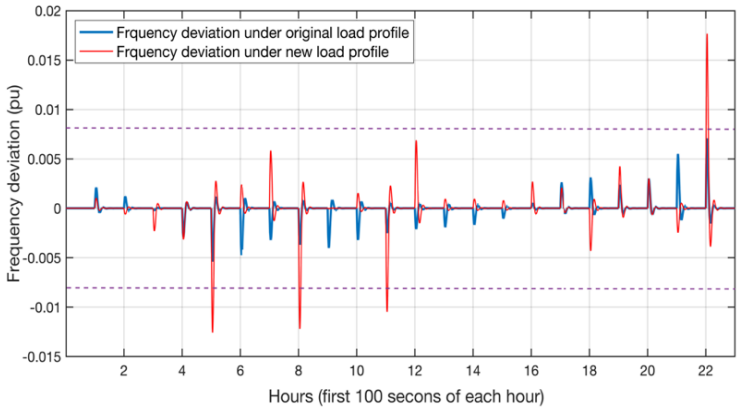

Figure 42. Frequency deviations in the microgrid before and after renewables' integration

To mitigate the negative effects of the renewables' integration to the power grid, three approaches are considered, and the results are compared together; model predictive control, the tariff regulation, and large-scale battery integration into the microgrid.

4.4.1. Frequency Control by Model predictive Control (MPC)

In this section, we design a model predictive controller on the system shown in Fig. 41. As the MPC is a discrete time control approach, we discretize the system with a very small sampling time while assuring the controllability of the system does not change. The state space representation of the system is

$$\begin{cases} x(k+1) = A_d x(k) + B_d u(k) + B_{dw} w(k) \\ y(k) = C_d x(k) \end{cases} \tag{42}$$

where the control input $u(k)$ determines p_{ref} value and $w(k)$ represents the disturbance. In this study, we consider load deviation, ΔP_l, as the disturbance. The goal of the MPC design is to reduce the effects of this disturbance on the frequency deviation as the output

of the system. Therefore, the controller and the system should satisfy the following constrains

$$|u(k)| \leq |u_{max}|, \forall\, k \tag{43}$$

$$|y(k)| \leq |y_{max}|, \forall\, k \tag{44}$$

y_{max} is selected very small to regulate $y(k)$ to zero. To control the uncertain system (42), we design the MPC state feedback controller as

$$u(k) = F(k)x(k) \tag{45}$$

where the following cost function is considered to evaluate the MPC performance.

$$J = \sum_{k=0}^{tf} J(k) = \sum_{k=0}^{tf} (x(k)^T W_x x(k) + u(k)^T W_u u(k)) \tag{46}$$

in which, W_x and W_u are the weight matrices. Following the robust MPC theories in [40], appropriate matrices Q, Y, and $Z > 0$ should satisfy the following linear matrix inequalities (LMIs) so that the state feedback controller guarantees the desired specifications on the output and control signals.

$$M_1 = \begin{bmatrix} 1 & * \\ x(k) & Q \end{bmatrix} \geq 0 \qquad M_2 = \begin{bmatrix} Q & * \\ Z & u_{max}^2 I \end{bmatrix} \geq 0 \tag{47}$$

$$M_3 = \begin{bmatrix} Q & * & * & * \\ A_d Q + B_d Y & Q & * & * \\ W_x^{1/2} & 0 & \gamma I & * \\ W_u^{1/2} & 0 & 0 & \gamma I \end{bmatrix} \geq 0 \tag{48}$$

$$M_4 = \begin{bmatrix} Q & * & * & * \\ A_d Q + B_d Z & Q & * & * \\ W_x^{1/2} & 0 & \gamma I & * \\ W_u^{1/2} & 0 & 0 & \gamma I \end{bmatrix} \geq 0 \tag{49}$$

$$M_5 = \begin{bmatrix} Q & * \\ C_d(A_d Q + B_d Y) & y_{max}^2 I \end{bmatrix} \geq 0 \tag{50}$$

$$M_6 = \begin{bmatrix} Q & * \\ C_d(A_d Q + B_d Z) & y_{max}^2 I \end{bmatrix} \geq 0 \tag{51}$$

$$\min_{Q,Y,Z} \gamma \ \ s.t: \ (47), (48), (49), (50), (51) \tag{52}$$

where (*) represents the diagonal transpose of the corresponding array. After finding appropriate matrices Q, Y, and Z using MATLAB and YALMIP toolbox for each step, the state feedback controller is designed as

$$F(k) = Y(k)Q^{-1}(k), \forall\, k \tag{53}$$

The MPC frequency regulation (Fig. 43) shows lower frequency deviation compared to the current tariff, however, the oscillation time is longer. The longer oscillation time is a challenge in power system especially in large area and in transmission level in which we try to damp the inter-area oscillation in a very limited time [41].

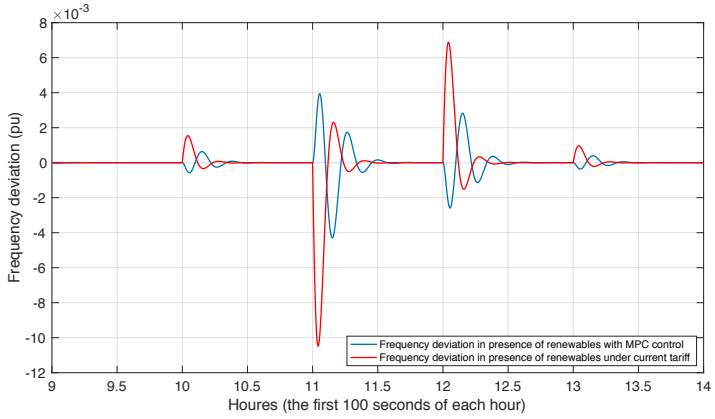

Figure 43. Frequency deviations in the microgrid with MPC control

4.4.2. Frequency Control by Tariff Modification

In the second case, in order to reduce frequency deviations, we apply the MDSF tariff to the same feeder with 30 percent renewables, the new load profile for MSDF rate is shown in Fig. 44 and the results for frequency deviation under new tariff are presented in Fig. 45.

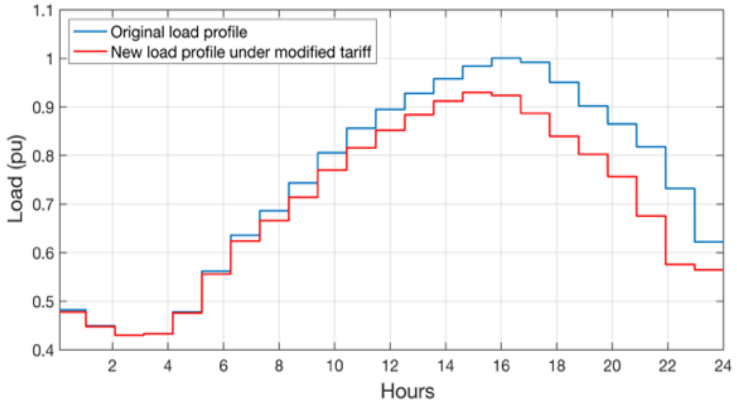

Figure 44. Load profile after 30 percent of renewables' integration in residential sector

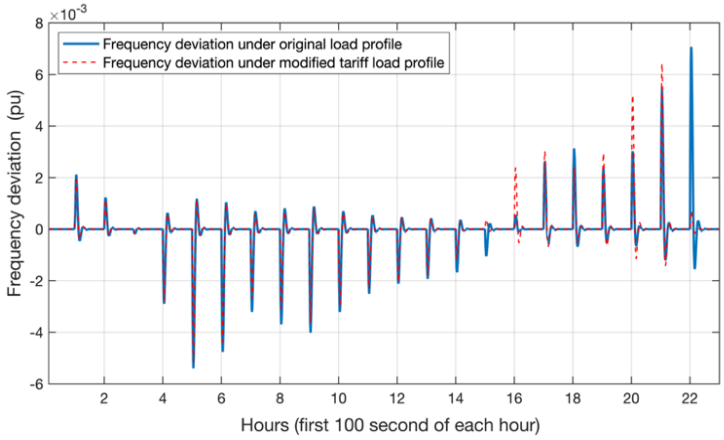

Figure 45. Frequency deviations in the microgrid under modified MDF tariff

4.4.3. *Frequency Control employing Large-Scale Battery*

In the third approach, we consider a large-scale battery connected to the microgrid to maintain the frequency regulation (see Fig. 46). Large-scale battery energy storage in power grid provide ancillary services such as peak load shaving [28], inter-area oscillation damping and load frequency deviation regulation [30] have widely been investigated. The

battery compensates the deficiency of the generation or absorbs surplus power generated by the CHP generator to maintain the frequency at the standard level. Considering the existing electricity tariff, presented in Fig. 6, the load frequency deviation in the presence of the 30 percent small-scale renewables are shown in Fig. 47.

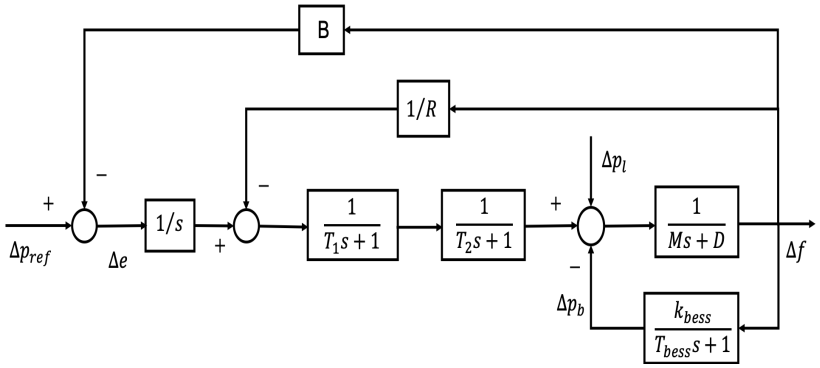

Figure 46. Battery integration to the microgrid

The battery integration to the microgrid moderates the frequency deviation; however, microgrid still has the frequency issues after peak time. Hence increasing the battery size could not be an optimum solution due to the battery installation and maintenance fees.

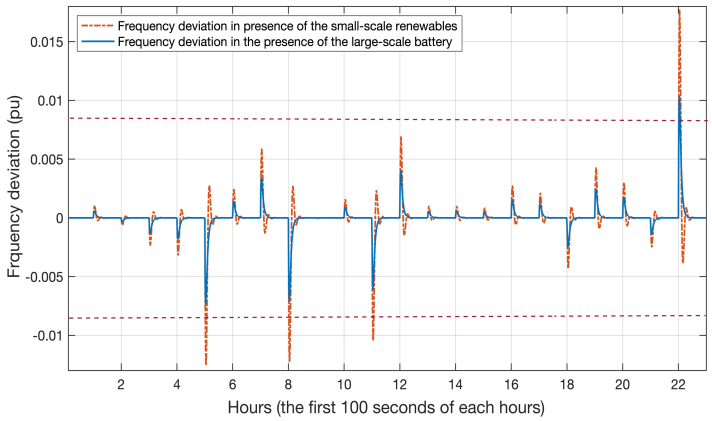

Figure 47. Frequency deviation in the presence of the large-scale battery

To closely compare the results obtained with MPC controller and the tariff modification approaches, we plot the frequency deviations in hours 9-14 in Fig. 48. The designed MPC

controller (blue line) acts better where the load deviation of the costumer is relatively small while in large load deviations, tariff modification (green line) is a more effective technique to reduce frequency deviations.

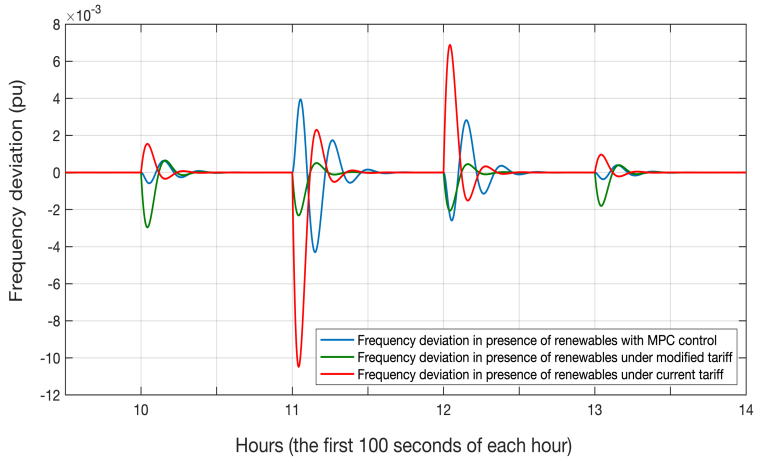

Figure 48. The MPC frequency control vs modified tariff

To closely compare the results obtained with MPC controller and the tariff modification approaches, we plot the frequency deviations for both cases for hours 9-14 in Fig. 15. The designed MPC controller (blue line) acts better where the load deviation of the costumer is relatively small while in large load deviations, tariff modification (green line) is a more effective technique to reduce frequency deviations.

The results for the large-scale battery integration to the microgrid (purple line) compared to the tariff modification (green line) are represented in Fig. 49. It has been shown that the tariff modification has a lower frequency deviation compared to the large-scale battery integration. However, the frequency oscillation in the microgrid is well damped by the large-scale battery among the other approaches with regard to its fast dynamic.

The results in Fig. 48 and Fig. 49 imply that:

the smart tariff regulation based on the customers' load consumption behavior and the renewables penetration level is the most promising solution to shape the power grid load profile.

Large-scale battery integration has lower oscillations, as a result, well-managed large-scale battery applications in larger microgrids or power system will increase the stability of the grids.

This study highlights the importance of the tariff regulation along with other existing control approaches, not as an alternative, to increase the reliability and resiliency of the power system in the presence of the renewables.

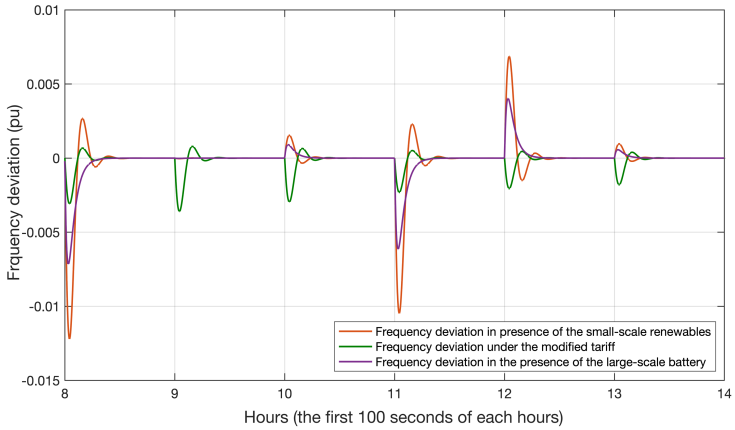

Figure 49. The frequency deviation in the presence of the large-scale battery vs modified tariff

The tariff modification is compared to the MPC frequency control and the large-scale battery integration into the microgrid. It is shown that the tariff modification is an effective tool to improve power system quality, particularly when the load deviation is relatively large. Moreover, we discuss that by tariff modification, in addition to the frequency control, utilities will be able to smoothen the load profiles in power grids and decrease the PAR. A

lower PAR in power systems guarantees lower investment requirements in the generation, transmission, and distribution system for a very short period of peak time.

CHAPTER FIVE

LARGE SCALE BATTERY INTEGRATION TO THE POWER GRID

5.1. Introduction

Inter-area oscillations are one of the main concerns in power system small signal stability. Since they involve a wide area in power systems, identifying the causes and damping the oscillations are a considerable challenge. Undamped inter-area oscillations cause severe problems in power systems including large-scale blackouts. Identification and designing a proper controller to damp inter-area oscillations in power systems is challenging due to the complexity and dynamic nature of the power system. Identification of inter-area oscillatory modes and damping of these oscillations have been widely investigated [42]- [44]. A distributed algorithmic approach has been studied to estimate the electro-mechanical oscillation modes of a power system by using real-time synchrophasor measurements of phase angles and frequencies [42]. In another study [43], a procedure for identifying critical oscillation modes is proposed based on the oscillation contribution factor, where the oscillation contribution factor for each generator is defined based on synthesizing parameters such as amplitude, damping ratio and attenuation obtained by the Prony algorithm. Tao Jiang et.al, [44] used a stochastic subspace identification (Data-SSI) algorithm to identify the system state space model. They proposed a new approach to estimate the dominant modes for monitoring inter-area oscillation in the China Southern power grid (CSG) by the use of phasor measurement units (PMUs) under both ringdown and ambient conditions. In spite of all this research inter area oscillation mode

identification and control is still a challenging area due to two factors related to the power system dynamic nature: *i)* the dominant mode varies with respect to the system dynamic such as load deviation and *ii)* the coherency of the system changes with regard to the dominant mode alteration. In a recent study, Oakridge National Lab. with co-operation of the University of Tennessee shows that the dominant modes cause the interarea oscillation changes with respect to load deviation in power system. Figure 50 shows the oscillation occurrence distribution of Eastern Interconnection (EI) through 2013 to 2015 during the day for each month [45]. And Fig. 51 shows the dominant frequency distribution of inter-area oscillations in Eastern Interconnection based on data in Fig. 50. It is shown that the dominant modes are a function of load deviation during the day and year.

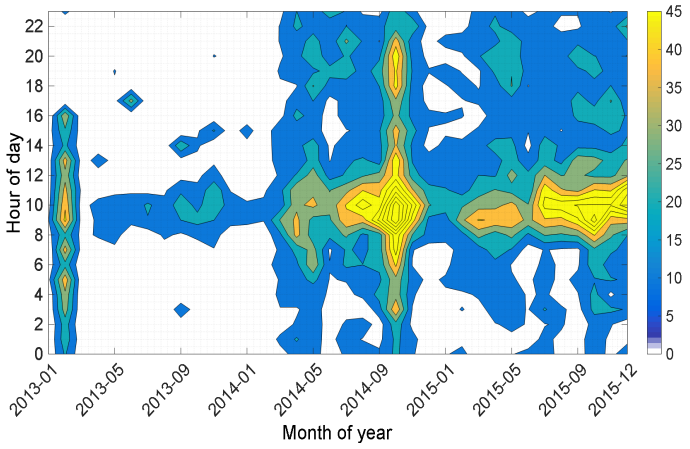

Figure 50. Inter-area oscillation occurrence distribution of EI

Considering the fact that the integration of the small-scale renewable increases the load deviation in the higher voltage level and will intensify the inter-area oscillation in transmission level, we need to identify weak transmission lines and design suitable control.

In this subject we need to evaluate the coherency of the generators and identify the weak links to balance the load flow or reinforce the weak tie lines.

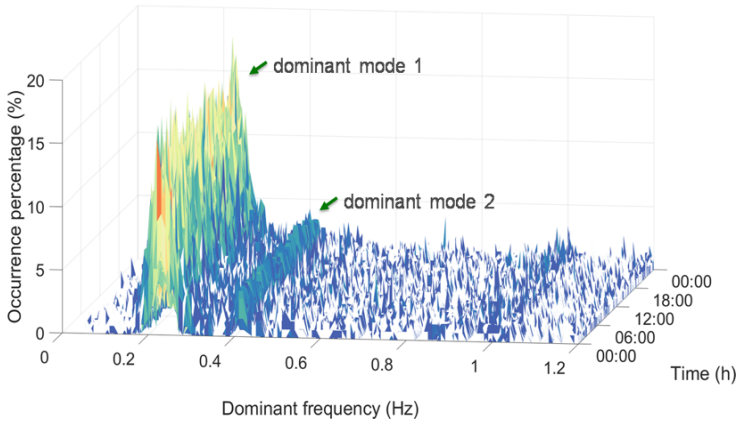

Figure 51. Dominant frequency distribution of inter-area oscillations in EI

In a power system formed by interconnecting two or more closely coupled generation/load areas through relatively weak ties, the coherent generators in each area exhibit similar rotor angle swings after a disturbance [46]- [49]. It is shown that generators that are closely coupled in an electrical sense tend to swing together in groups during disturbances, and this characteristic behavior can be exploited to reduce the size of the power system model [50]- [53]. In the coherency-based method, each coherent group of generators is replaced by a single equivalent generator. This achievement helps us to study power system dynamic and transient stability without simulation of the full power system [50]. In systems having a number of low frequency inter-area modes, we can use the coherency property to identify relatively closely coupled generators from the angle components of eigenvectors of the inter-area modes [51]. Moreover, we can also identify the buses having angles which oscillate coherently with the generator angles. This divides the system into sets of coherent

buses and generators equal in number to the number of inter-area modes. The tie lines between one coherent group and another are the weak connections which are the root cause of the inter-area oscillations. Since the coherency of the power system changes with regard to the load deviation, decomposing the power grid based on dominant mode deviation is a useful approach to design the decentralized controller for a large-scale system or initiate the optimum locating for the large-scale batteries integration to the power system to reduce the load flow in the high-risk lines. As decentralized control approaches are more practical in large scale systems, they have been widely used in power systems [54- [55]. To design each individual controller in a decentralized control approach, no exchange of information among different areas is necessary, which makes the control design easier to implement in large power systems. Also, decentralized control design of lower dimensional subsystems increases system robustness with respect to a wide variety of structured and unstructured perturbations in the interconnections [56]. For this purpose, a large-scale system is decomposed into smaller subsystems without losing any information. These subsystems will have smaller dimensions compared to the large-scale system so that the solution to the control design problem will be more tractable.

Damping the inter area oscillation using the energy storage system is considered in several studies [57]-[60]. Damping the oscillations by an energy storage device using particle swarm optimization and heuristic dynamic programming is discussed in [59] and shown to outperform Power System Stabilizers (PSS) and Flexible AC Transmission Systems (FACTS)-enabled damping on the same example system. An energy storage system based on Ultra Capacitor technology is proposed for damping control via real power modulation

in [60]. However, in all above-mentioned studies the battery has been considered as an active power source to inject/absorb active power while the major advantage of BESS is the fact that both its active power and power factor are adjustable and controllable by the firing angle of the thyristors in the inverter. Therefore, by controlling the inverter, it is possible to have reactive power injection in the power system. As the reactive power directly affects the voltage deviation in power systems, unstudied reactive power flow may cause voltage instability in the network. Considering the growing penetration level of the large-scale batteries in future power grids highlights the importance of an accurate battery dynamic model to capture the effect of both the active and reactive power injection to the power system.

In this section, we consider a loop shape power system consisting of three different interconnected areas with the exact models for the generators and tie lines to see the effect of the controller on a loop shape system where we will have different power injection in each area. The objective of this section is:

i) to study the effect of the load deviation on the coherency of the generators;

ii) to find a systematic solution to design decentralized servomechanism controllers for a large-scale system to target specific oscillation modes and damp the oscillation.

iii) to investigate the effect of a large-scale battery integration on the power system stability as a control device to damp the inter area oscillations.

iv) to design a control system to control the active and reactive power of the battery

by thyristor firing angle to damp the inter-area oscillation in the power system.

5.2. Power System Coherency

When a power system is subjected to a disturbance such as load deviation or fault id transmission lines, the machines of the system tend to separate into groups within which the rotors of the member machines oscillate in harmony. This physical property is known as coherency, and machines which swing together are called coherent machines.

Coherency depends, in a complex fashion, on several factors such as machine inertias, initial operating conditions, system topology, and the location of the disturbance. In fact, it is possible that for a given disturbance a machine may be a member of one coherent group, while for a different disturbance the same machine may become a member of another coherent group. In order to integrate a large-scale battery to the power grid there are several approaches such as frequency regulation [61]- [62], power loss reduction [63], and peak load shaving [64].

As it is mentioned, one of the major challenges in future power grid is power transmission from the future renewable resources to the demand centers. DC superconducting cables development plan and large-scale battery were two highlighted plans to overcome above-mentioned issue. In this regard, battery integration to the power system should carefully be studied.

In the section one, we showed that the higher level of small-scale renewables penetration in distribution system will be a challenging issue due to abnormal power flow deviation in the transmission lines which can be considered as disturbances. Graham in [46] clearly

shows that these disturbances can result in power system instability in weak tie lines. In this section, we evaluate the potential effect of the load deviation on generators coherency to find the potential weak tie lines which should be taken in consideration for large-scale battery integration. For this purpose, a three-area power system as shown in Fig. 52 is considered as our case study model. The load consumption in area one is altered from $11 + j2$ (Fig.52) to $8 + j2$ (Fig. 54) to simulate the small-scale renewables integration in one area. The oscillatory frequencies and coherent generators for the first scenario are shown in Fig. 54. To evaluate the coherency of the system for current loading, a three-phase fault on bus 6 is applied to the system. It is clear that the coherency of the generators (Fig. 53) and buses (given in Table 6) are different for each inter-area oscillation modes.

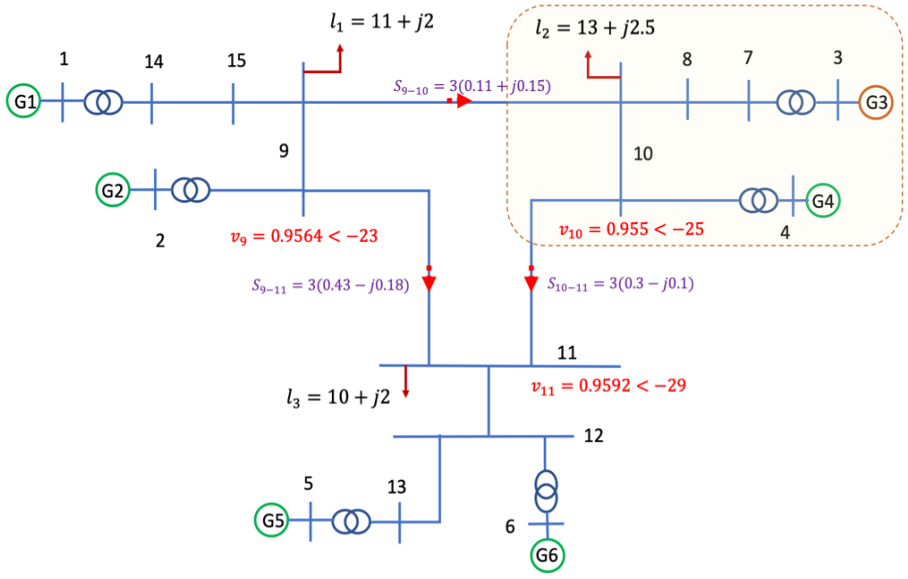

Figure 52. Case study power system generators coherency for the first scenario $l_1 = 11 + j2$

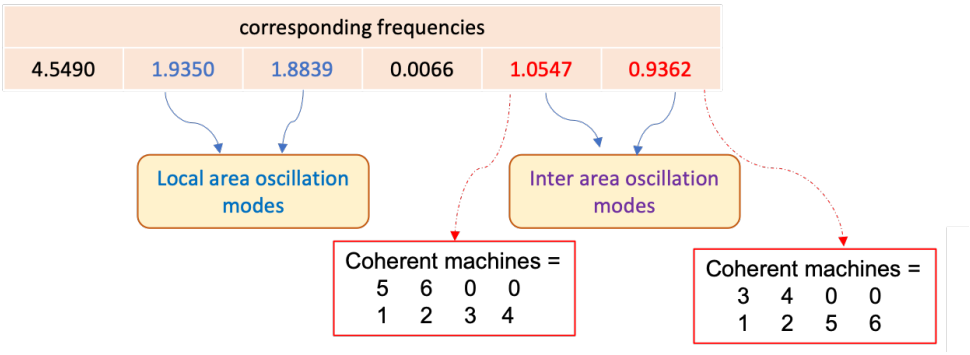

Figure 53. Inter-area oscilation modes and the coherency of the generators for first loading scenario

For the first mode, *f=0.9362 hz*, machines in the second area, G3 and G4, will oscillate against the rest of the power system while for the second mode, *f=1.0547 hz*, the third area, G5 and G6, will oscillate against the rest of the power system. The weak tie lines for the first mode under current load consumption will be the 9-10 and 10-11.

Table 6. Buses' coherency for the first scenario

Bus	Mode 0.9362		Mode 1.0547	
1	0.9861	0.0139	0.9917	0.0083
2	0.8529	0.1471	0.9091	0.0909
3	0.014	0.986	0.9748	0.0252
4	0.1483	0.8517	0.8982	0.1018
5	0.511	0.489	0.0283	0.9717
6	0.5077	0.4923	0.3558	0.6442
7	0.0669	0.9331	0.946	0.054
8	0.1893	0.8107	0.8785	0.1215
9	0.7241	0.2759	0.8371	0.1629
10	0.2799	0.7201	0.8299	0.1701
11	0.5065	0.4935	0.4598	0.5402
12	0.5076	0.4924	0.3614	0.6386
13	0.51	0.49	0.133	0.867
14	0.9336	0.0664	0.9606	0.0394
15	0.8128	0.1872	0.8883	0.1117

In the second scenario, same fault is applied to the system under new loading situation. The coherency of the generators (Fig. 53) and buses (given in Table 7) are different for each inter-area oscillation modes and from the first loading scenario. For the first mode, *f=0.9434 hz*, machines in the first area, G1 and G2, will oscillate against the rest of the power system while for the second mode, *f=1.0607 hz*, the third area, G5 and G6, will oscillate against the rest of the power system (see Fig. 55). The weak tie lines for the first mode under current load consumption will be the 9-10 and 9-11.

To design the proper control system to damp the oscillation we need to identify the dominant modes and their occurrence probability to design adequate control with lowest cost to meet the reliability of the system. In the next section, a servomechanism control design solution will be introduced to damp the effect of the certain oscillatory modes in the system.

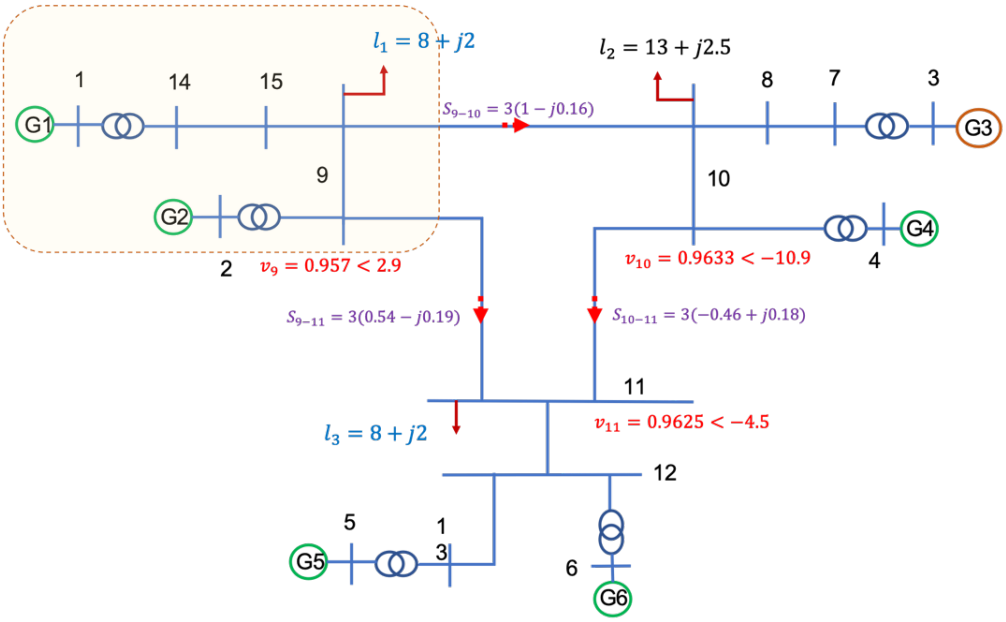

Figure 54. Case study power system generators coherency for the second scenario $l_1 = 8 + j2$

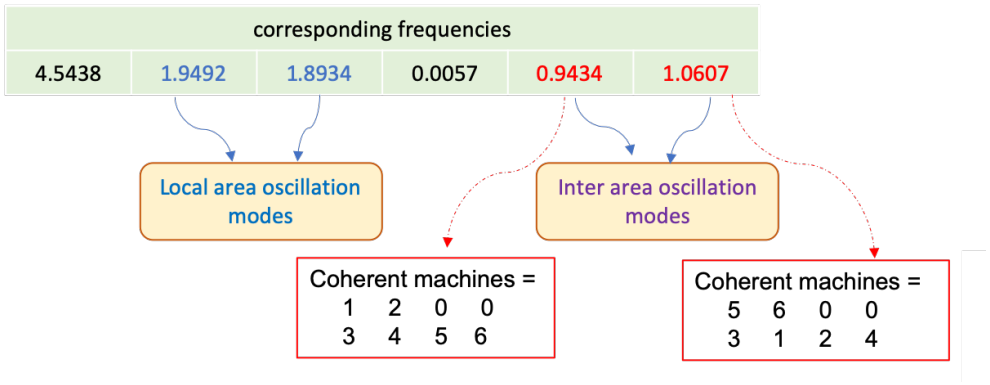

Figure 55. Inter-area oscilation modes and the coherency of the generators for second loading scenario

Table 7. Buses' coherency for the second scenario

Buses	Mode 0.9434		Mode 1.0607	
1	0.9863	0.0137	0.9923	0.0077
2	0.8524	0.1476	0.9156	0.0844
3	0.0147	0.9853	1.0643	-0.0643
4	0.1447	0.8553	0.9695	0.0305
5	0.4533	0.5467	0.0293	0.9707
6	0.4738	0.5262	0.3691	0.6309
7	0.0689	0.9311	1.0261	-0.0261
8	0.1869	0.8131	0.9427	0.0573
9	0.722	0.278	0.8495	0.1505
10	0.2722	0.7278	0.8839	0.1161
11	0.479	0.521	0.4774	0.5226
12	0.4744	0.5256	0.3747	0.6253
13	0.4606	0.5394	0.1376	0.8624
14	0.9347	0.0653	0.9631	0.0369
15	0.8134	0.1866	0.8961	0.1039

5.3. Case Study Model

We consider a three-area system connected to each other through tie lines in a loop shape configuration as shown in Fig. 56.

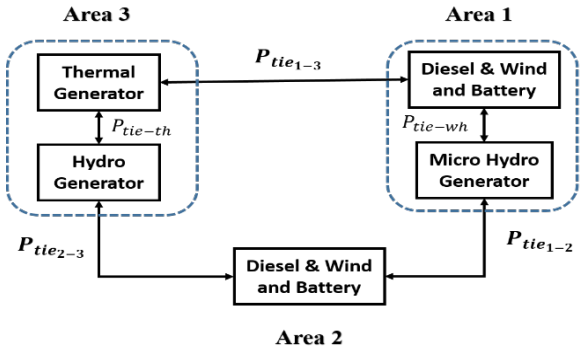

Figure. 56. Large-scale power system case study model

The vector $\mathrm{X} = [\mathrm{X}_1, \mathrm{x}_2, \mathrm{X}_3, \mathrm{x}_4, \mathrm{X}_5, \mathrm{x}_6]^{\mathrm{T}}$ represents state variables for the whole system. X_1, X_3, and X_5 are the state variables for the first, second, and the third area respectively; and X_2, X_4, and X_6, are the tie lines dynamics.

First Area

The first area is a subsystem composed of two parts. The first part contains a wind generator, a diesel generator, and a battery energy storage as a short-term back-up for wind generation. Energy storage devices as actuators for damping control systems, have several advantages. Most of these devices have very fast response times and can provide both power injection and absorption (discharge and charge, respectively). This can allow the energy storage system to participate in both power and energy application simultaneously, thus increasing the value proposition of the device [3]. The second part is a micro hydro generation unit connected to the first part through a tie line. The dynamic model of the first part is shown in Fig. 57, and Fig. 58 displayed second part of the model for the first area.

The first area has three inputs and three outputs, and it is defined by a 16×16 state matrix. The state variables defining this area are:

$$X_1 = [\Delta f_{1-1}, \Delta P_{GD}, \Delta X_{ED1}, \Delta X_{ED2}, \Delta F_T, \Delta X_{PC1}, \Delta X_{PC2}, \Delta X_{PC3}, \Delta P_{BES}, \Delta P_{BESdroop}$$

$$, \Delta P_{tie-wh}, \Delta f_{1-2}, \Delta P_{GH}, \Delta P_{RH}, \Delta X_{EH}, \Delta P_{refH}]$$

where Δf_{1-1} is the frequency deviation of the first part (hybrid system), and Δf_{1-2} is the frequency deviation of the second part (micro hydraulic) [65]. $\Delta \mathrm{P_{BES}}, \Delta \mathrm{P_{BESdroop}}$ are representing battery dynamics and ΔP_L shows connected load variations in the grid. Inputs and outputs of this area, are defined as

$$U_1 = [\Delta P_{CD}, \Delta P_{CW}, \Delta P_{refh}]$$

$$Y_1 = [\Delta f_{1-1}, \Delta P_{tie-wh}, \Delta f_{1-2}]$$

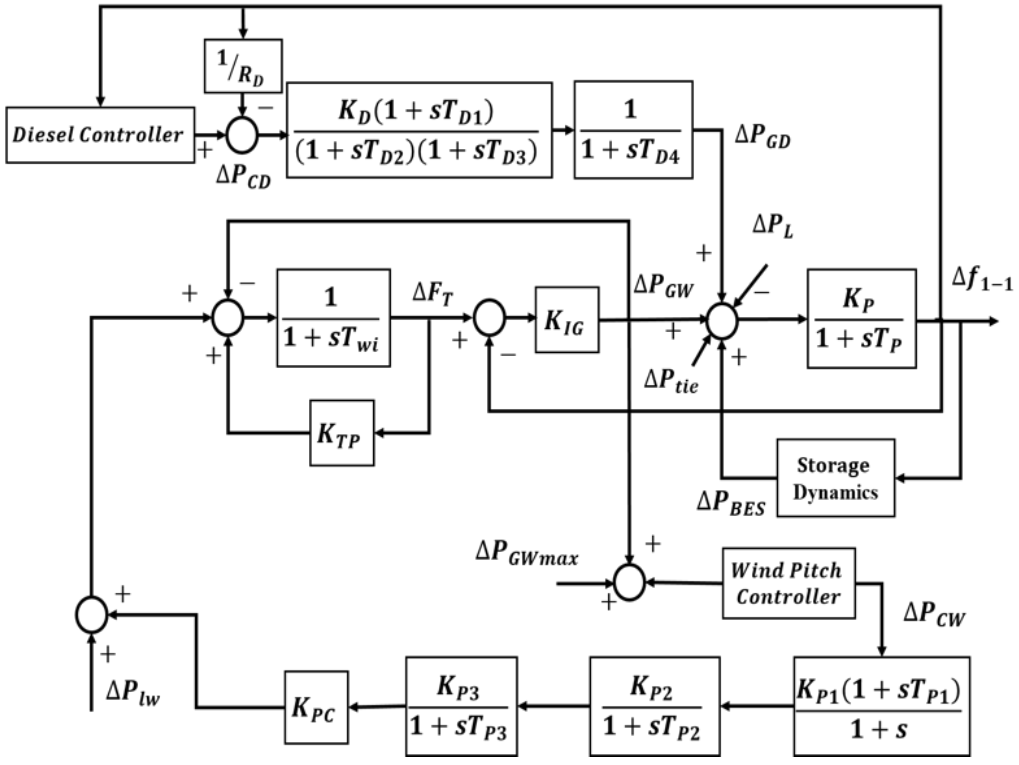

Figure 57. Dynamic model of wind generator, diesel generator, and battery as a backup [65], [66]

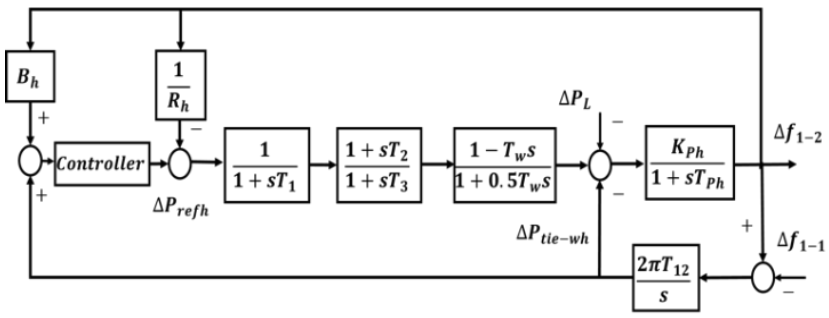

Figure 58. Dynamic model of micro hydro generator [66]

Second Area

The second area is the same as the first part of the first area shown in Fig. 57. This area consists of a wind generator, a diesel generator, a battery as a short-term backup for wind generation. This subsystem has been modeled with a 10×10 state matrix with two inputs and two outputs.

$X_3 = [\Delta f_2, \Delta P_{GD}, \Delta X_{ED1}, \Delta X_{ED2}, \Delta F_T, \Delta X_{PC1}, \Delta X_{PC2}, \Delta X_{PC3}, \Delta P_{BES}, \ \Delta P_{BESdroop}]$

Inputs and outputs for this area are:

$U_2 = [\Delta P_{CD}, \Delta P_{CW}]$

$Y_2 = [\Delta f_2, \Delta X_{PC3}]$

Third Area

Finally, the third area consists of a reheat-thermal generator unit and a hydro generator. These generators are connected together through a tie line as shown in Fig. 59. This tie line is considered so that both generators have same output (referring to case in two areas four machines [67]).

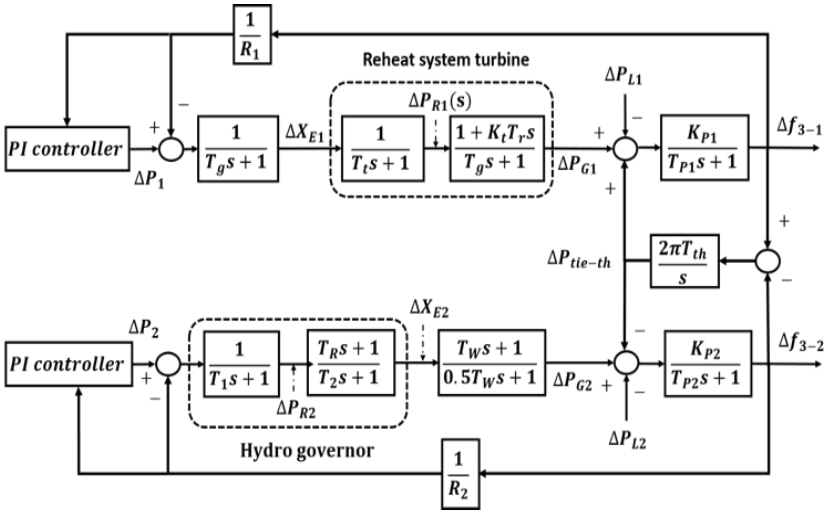

Figure 59. Dynamic model of a hydraulic generator and a reheat generator connecting through a tie line [67]

This system has two inputs, two outputs and it is modeled via a 11×11 state matrix. The state variables defining the third area are:

$X_3 = [\Delta X_{E1}, \Delta P_{G1}, \Delta P_{R1}, \Delta f_{3-1}, \Delta Y_1, \Delta X_{E2}, \Delta P_{G2}, \Delta P_{R2}, \Delta f_{3-2}, \Delta P_{th}, \Delta Y_2]$

where Δf_{3-1} is frequency variation of the thermal unit, Δf_{3-2} is the hydro unit frequency variation, and ΔP_{L1}, and ΔP_{L2} are the connected load variations in the grid.

Inputs and outputs for this area are:

$U_3 = [\Delta P_1, \Delta P_2]$

$Y_3 = [\Delta f_{3-1}, \Delta f_{3-2}]$

The original large-scale power system is simulated by a 40×40 state matrix containing three aforementioned subsystems and three tie lines' dynamics. This system has seven inputs and outputs in total.

5.4. Servomechanism Control Design

To design a servomechanism control we consider a loop-shaped three-area power system connected to each other through tie-lines. The system will be decomposed to three lower order system and a decentralized control will be designed for each area based on inter-area oscillation modes to damp the oscillation.

5.4.1. System Decomposition

For a large-scale system, it is almost impossible to design a central control. Decomposition of a large-scale systems with the overlapping structure, especially in power system, has been an important research area to solve control design challenge in large-scale systems. System decomposition methodology is built based on expanding the system's state space equations; so that, the overlapping subsystems effect is shown as disjoint subsystems.

Each disjoint subsystem includes all information needed from the rest of the system that gives the decomposed subsystem the opportunity of working independently. So, a decentralized controller can be designed for each subsystem to guarantee the desired performance of the system. There are different decomposition approaches for large-scale systems. Some of the common methods are nested epsilon decompositions approach, balanced box-decompositions (BBD) method, and overlapping decompositions [68], [69]. In this study, we use overlapping decomposition method to decompose the large-scale system into smaller subsystems based on its configuration. The schematic of the system is represented in Fig. 60.

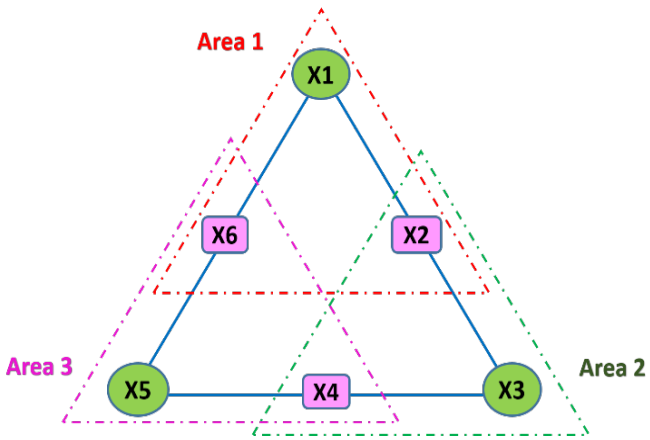

Figure 60. Overlapping decomposition schematic for loop structure

By considering $X = [X_1, X_2, X_3, X_4, X_5, X_6]^T$ as the states variables for the whole system shown in Fig. 54, the corresponding state matrix is defined as

$$A = \begin{bmatrix} A_{11} & A_{12} & 0 & & A_{16} \\ A_{21} & A_{22} & A_{23} & \cdots & 0 \\ 0 & A_{32} & A_{33} & & 0 \\ & \vdots & & \ddots & \vdots \\ A_{61} & 0 & 0 & \cdots & A_{66} \end{bmatrix}$$

Using the overlapping decomposition methodology, the decomposed subsystems will be represented as following:

First decomposed area:

$$\begin{cases} \dot{\bar{X}}_1 = \bar{A}_1 \bar{X}_1 + \bar{B}_1 \bar{U}_1 \\ \bar{Y}_1 = \bar{C}_1 \bar{X}_1 \end{cases} \tag{54}$$

where the first subsystem given in (54) has three inputs and three outputs, and 18 states. These states are $\bar{X}_1 = [X_6, X_1, X_2]^T$ and the state matrix, input and output matrix are

$$\bar{A}_1 = \begin{bmatrix} A_{66} & A_{61} & A_{62} \\ A_{16} & A_{11} & A_{12} \\ A_{26} & A_{21} & A_{22} \end{bmatrix}, \bar{B}_1 = \begin{bmatrix} B_{13} & B_{11} & B_{12} \\ B_{23} & B_{21} & B_{22} \\ B_{33} & B_{31} & B_{32} \end{bmatrix}$$

$\bar{C}_1$ is block diagonal $\{C_{66}, C_{11}, C_{22}\}$, and

$\bar{X}_1 \in R^{18}, \bar{U}_1 \in R^3, \bar{Y}_1 \in R^3$, $\bar{A}_1: R^{18} \times R^{18}$, $\bar{B}_1: R^{18} \times R^3$, and $\bar{C}_1: R^3 \times R^{18}$.

Second decomposed area:

The second subsystem has two inputs and outputs. The subsystem in (55) has 12 states which are defined as $\bar{X}_2 = [X_2, X_3, X_4]^T$

$$\begin{cases} \dot{\bar{X}}_2 = \bar{A}_2 \bar{X}_2 + \bar{B}_2 \bar{U}_2 \\ \bar{Y}_2 = \bar{C}_2 \bar{X}_2 \end{cases} \tag{55}$$

The state, input and output matrices for the second subsystem are

$$\bar{A}_2 = \begin{bmatrix} A_{22} & A_{23} & A_{24} \\ A_{32} & A_{33} & A_{34} \\ A_{42} & A_{43} & A_{44} \end{bmatrix}, \bar{B}_2 = \begin{bmatrix} B_{21} & B_{22} & B_{23} \\ B_{31} & B_{32} & B_{33} \\ B_{41} & B_{42} & B_{43} \end{bmatrix}$$

and $\bar{\mathrm{C}}_2$ is block diagonal $\{\mathrm{C}_{22}, \mathrm{C}_{33}, \mathrm{C}_{44}\}$ where

$\bar{X}_2 \in R^{12}$, $\bar{U}_2 \in R^2, \bar{Y}_2 \in R^2$, $\bar{A}_2: R^{12} \times R^{12}$, $\bar{B}_2: R^{12} \times R^2$, and $\bar{C}_2: R^2 \times R^{12}$.

Third decomposed area:

Finally, the third decomposed subsystem is defined as in (56). It has two inputs and two outputs, with 15 states.

$$\begin{cases} \dot{\bar{\mathrm{X}}}_3 = \bar{\mathrm{A}}_3 \bar{\mathrm{X}}_3 + \bar{\mathrm{B}}_3 \bar{\mathrm{U}}_3 \\ \bar{\mathrm{Y}}_3 = \bar{\mathrm{C}}_3 \bar{\mathrm{X}}_3 \end{cases} \tag{56}$$

These states are $\bar{X}_3 = [X_4, X_5, X_6]^T$ and the state, input and output matrices are

$$\bar{A}_3 = \begin{bmatrix} A_{44} & A_{45} & A_{46} \\ A_{54} & A_{55} & A_{56} \\ A_{64} & A_{65} & A_{66} \end{bmatrix}, \bar{B}_3 = \begin{bmatrix} B_{42} & B_{43} & B_{41} \\ B_{52} & B_{53} & B_{51} \\ B_{62} & B_{63} & B_{61} \end{bmatrix}$$

and $\bar{\mathrm{C}}_3$ is block diagonal $\{C_{44}, C_{55}, C_{66}\}$ such that

$\bar{X}_3 \in R^{13}$, $U \in R^2$, $Y \in R^2$ *and* $\bar{A}_3: R^{13} \times R^{13}$, $\bar{B}_3: R^{13} \times R^2$, $\bar{C}_3: R^2 \times R^{13}$.

After decomposing the large-scale system, still it can be too complicated to deal with decomposed subsystems due to their high order equations. An approximation procedure is

utilized to generate reduced order models of particular structure that maintain the main characteristic behavior of the original system that facilitate the decentralized control design. This particular structure is explained in the next section.

Control Design for Interconnected Systems

For a linear time-invariant system as

$$\begin{cases} \dot{x} = Ax + \sum_{j=1}^{r} B_j u_j \\ y_j = C_j x \qquad j = 1,2, \dots, r \end{cases} \tag{57}$$

Referring to the theorem in [70], a decentralized linear time invariant controller exists for the decentralized ω control-agent system so that, the closed loop system is stable in sense of Lyapunov (asymptotically) if and only if all the decentralized fixed modes of system given in (57) lie on the open left half of the complex plane. If we have additive disturbance of ω added to the right-hand side of (57) such that

$$\begin{cases} \dot{z}_1 = A_1 z_1 \\ \omega = Q_1 z_1 \end{cases} \tag{58}$$

where $z_1 \in R^{s1}$, and (Q_1, A_1) is observable and $z_1(0)$ is unknown. Each control agent has a pre-specified reference output y_j^r and the aggregated reference vector $y_{ref} = [y_{1,r}, y_{2,r}, \dots, y_{r,r}]^T$ to satisfy

$$\begin{cases} \dot{z}_2 = A_2 z_2 \\ y_{ref} = Q_2 z_2 \end{cases} \tag{59}$$

It is shown that under certain conditions, there exist a solution to the decentralized servomechanism problem so that $e(t) \to 0$ as $t \to \infty$ for all above mentioned disturbances [21]. Note that $e(t) = y(t) - y_{ref}(t)$.

Consider the special case,

$$\ddot{Y} = P\dot{Y} + QY + RU \tag{60}$$

where both $Y(t)$ and $U(t)$ are n-dimensional vectors. P, R, and Q are real with compatible dimension matrices. Having R full rank will guarantee the existence of a solution for the servomechanism problem [20]. By defining $\mathrm{Y} = \mathrm{X}_1$, and $\dot{Y} = \mathrm{X}_2$, system can be rewritten as

$$\begin{cases} \begin{bmatrix} \dot{X}_1 \\ \dot{X}_2 \end{bmatrix} = \begin{bmatrix} 0 & I \\ P & Q \end{bmatrix} \begin{bmatrix} X_1 \\ X_2 \end{bmatrix} + \begin{bmatrix} 0 \\ R \end{bmatrix} U \\ Y = [I \quad 0] \begin{bmatrix} X_1 \\ X_2 \end{bmatrix} \end{cases} \tag{61}$$

then, the following theorem can be applied to the system.

Theorem [70]

A necessary and sufficient condition to exist a solution to decentralized servomechanism for given system in (60) such that

$$y(t) \to y_{ref}(t) \;\; or \quad e(t) \to 0 \quad \text{as:} \;\; t \to \infty$$

for all those classes of disturbances described by (58) and for all pre-specified reference inputs described by (59), is that matrix R be full rank. The full rank matrix R guarantees the existence of the solution for the given system. Therefore, if we model each subsystem with the given structure in (61) such that R matrix be full rank, the existence of a decentralized controller will be guaranteed.

Note*:* Not all systems given in (57) structure can be rewritten as (60). To take advantage of the aforementioned theory in our large-scale system, we will need to identify each decentralized subsystem as (61). This will guarantee the existence of a decentralized controller for each identified system. In next step, we identify a reduced order model for each subsystem in the form of (61). Each area should be identified with a $2m$ order system, where m is the number of inputs in each decentralized subsystem.

5.4.2. System Identification

specific form represented by (61). This specific form of systems modeling guarantees the existence of a solution to the existence of designing controller for the system in presence of disturbances such that system's outputs converge to reference outputs asymptotically. This requires reduction in the system order according to the number of system's inputs/outputs and given structure in (61). To this end, we use system identification to derive reduced order model for each decomposed subsystem.

System identification is an approach to model a black or grey (unknown or partially known) dynamic system. The estimate model is developed based on observations of input/output experimental data. System identification techniques are applicable in time domain or frequency domain. In frequency domain identification, discrete Fourier transform (DFT) is employed to transfer the data to the frequency domain, then model parameters are estimated in the frequency domain. In time domain identification, measured data are used directly to estimate model parameters. In this section, we use time domain system identification.

Next, for each of these identified subsystems as the reduced order model of each area, our aim is to design a controller to guarantee stable and desired performance of the system in the existence of defined disturbances. The designed controllers will be applied to the original system to improve the small signal stability of the system. Small signal stability in power systems is defined as the ability of the power systems to maintain synchronism when they are subjected to small perturbations [67]. Load changes is an example of small disturbances which often occur in power systems. The small load changes can be defined

as bounded disturbances. In the following, we use servomechanism disturbance rejection approach for control design with the purpose of damping the inter-area oscillations.

5..4.3. Servomechanism Control Design

As discussed in [70], designing a suitable controller based on the reduced order model information such that it works properly on the original system is a real challenge. Practical approaches have been proposed to maintain the robustness of the feedback controller [71]-[73]. In general, one of the reasons that leads to poor performance of the controller on the original system is the error between the original system and the identified one [72]. After system decomposition and system identification, the difference between the original system and the identified system, especially some of the oscillatory modes, appear as disturbances in the system. These errors should be considered in the controller design.

In this section, we consider the oscillation modes of the original decomposed subsystems as input disturbances for the identified subsystems. These modes cause the oscillations in the original system and we attempt to damp their oscillatory effects.

For a given system (62) with input disturbance

$$\begin{cases} \dot{x} = Ax + Bu + \omega \\ y = Cx \end{cases} \tag{62}$$

where the state of the system x is a n-vector, and the output, y, is a r-vector ($r \leq n$), and

i) $\omega = (\omega_1, \omega_2, \dots, \omega_n)'$is unknown, unmeasurable disturbance which belongs to a certain class of disturbances such that it satisfies (63),

$$\omega_k^{(p)} + p_p \omega_k^{(p-1)} + \cdots + p_2 \dot{\omega}_k + p_1 \omega_k = 0$$

$k = 1,2, \dots, n$ (63)

ii) closed-loop system dynamic behavior is specified,

iii) $y(t) \to y_{ref}(t)\ or\ e(t) \to 0$ as $t \to \infty$ for all ω, where $y_{ref} = (y_{1,r}, y_{2,r}, \dots, y_{r,r})$ and $y_{i,r}$ satisfies the differential equation

$$y_{k,r}^{(p)} + p_p y_{k,r}^{(p-1)} + \cdots + p_2 \dot{y}_{k,r} + p_1 y_{k,r} = 0 \quad (64)$$

$k = 1,2, \dots, n$

where $y_{k,r}(0)$, $\dot{y}_{k,r}(0)$, …, $y_{k,r}^{(p-1)}(0)$ are specified,

Davison in [28] shows that, there exists a minimal order linear time invariant differential feedback controller of the form

$$u = K_0 x + \sum_{i=1}^{r} K_i\, n_i \quad (65)$$

stabling the closed-loop system, if

i) (A, B) be controllable

ii) rank $\Gamma = n + rp$

where

$$\Gamma = \begin{bmatrix} \mathcal{M}_p & \mathcal{M}_{p-1} & \dots & \mathcal{M}_2 & \mathcal{M}_1 & B \\ CA^{p-1} & CA^{p-2}B & \dots & CAB & CB & 0 \\ \vdots & \vdots & \ddots & \vdots & \vdots & \vdots \\ CA^{p-1} & CAB & \dots & 0 & 0 & 0 \\ CA^{p-1} & CB & \dots & 0 & 0 & 0 \\ C & 0 & \dots & 0 & 0 & 0 \end{bmatrix}$$

$\mathcal{M}_1 = AB + p_p B$

$\mathcal{M}_2 = A^2 B + p_p AB + p_{p-1} B$

$$\vdots$$

$$\mathcal{M}_{p-1} = A^{p-1}B + p_p A^{p-2}B + \cdots + p_2 B$$

$$\mathcal{M}_p = A^p + p_p A^{p-1} + p_{p-1} A^{p-2} + \cdots + p_2 A + p_1 I$$

and

$$\dot{n}_i = \delta n_i + \begin{pmatrix} 0 \\ 0 \\ \vdots \\ 0 \\ 1 \end{pmatrix} (y - y_{i,r}) \qquad i = 1,2,\dots,\tau$$

$$\delta = \begin{bmatrix} 0 & 1 & 0 & \dots & 0 \\ 0 & 0 & 1 & \dots & 0 \\ \vdots & \vdots & \vdots & \ddots & \vdots \\ 0 & 0 & 0 & 0 & 0 \\ -p_1 & -p_2 & -p_2 & \dots & -p_p \end{bmatrix}$$

In our case study system, not all states of the subsystems are available as outputs. Therefore, to implement the above controller, state estimation is essential to have access to the states of identified subsystems. To this end, a Luenberger observer is designed for each identified subsystem to have a good state estimation on the reduced order model [72].

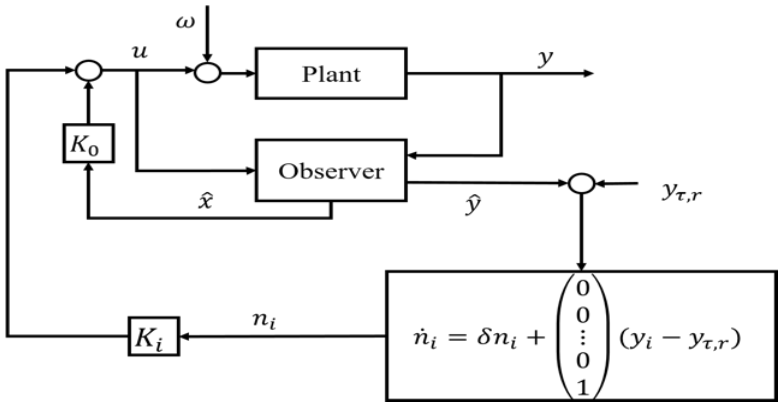

Figure. 61. Observer and output controller configuration

The block diagram of the observer and servomechanism controller for disturbance rejection is shown in Fig. 61. The oscillation modes causing the oscillation in the original system, are considered as disturbances which we desire to damp.

Remarks

i) This approach agrees with the results we have for the class of step and impulse disturbances in [71] which has been employed for same case study system in [72].

ii) This approach can be applied for sinusoidal disturbances except those that can cause rank deficiency due to their frequencies [72].

iii) K_0, and K_i are found such that the closed-loop system remains stable. This system will be robust for any changes in system parameter or feedback gain matrices if the closed-loop system stays stable [71]. Note that, there is no guarantee transient behavior will be satisfactory [73]. For instance, transient performance may be excessively slow or have poorly damped oscillatory behavior [72].

5.4.4. Results and discussion

To investigate the effect of the designed controller for inter-area oscillation on the original system, we implement the designed controller on the original three area system. Next, a step disturbance with magnitude of 0.01 pu at t=10 s, is applied to the system in tie line between first and second area. This small perturbation will excite modes of the system. This disturbance can be any small signal perturbation in power system representing some load connection/ disconnection to the power grid or any other small changes in system's steady state operating point.

The results of frequency deviations in each area prior and after applying the servomechanism controller to the system are shown in Figs. 62-64. As it is shown, inter-area oscillations are well damped. The blue solid lines indicate system response to the perturbation when the designed decentralized servomechanism controller is applied to the system. The outputs of the system with no controller are shown via solid red lines. The obtained results are in line with our previous work of state feedback controller [72], except for the third area. Although the third area has relatively slower damping time, still it fulfils the requirements for power quality, and it is more robust to the identification error comparing to the state feedback controller.

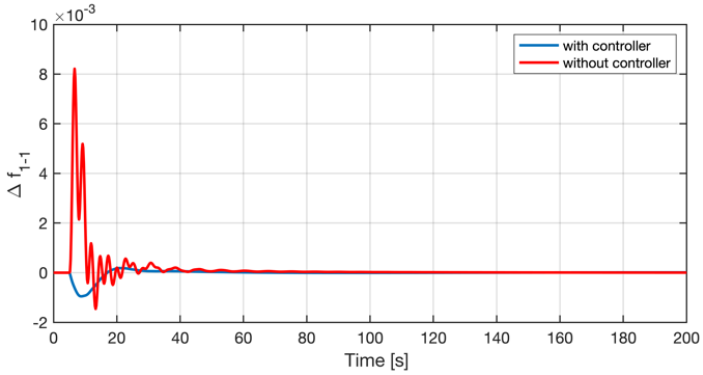

Figure 62. Frequency deviation in first area due to fault in tie line

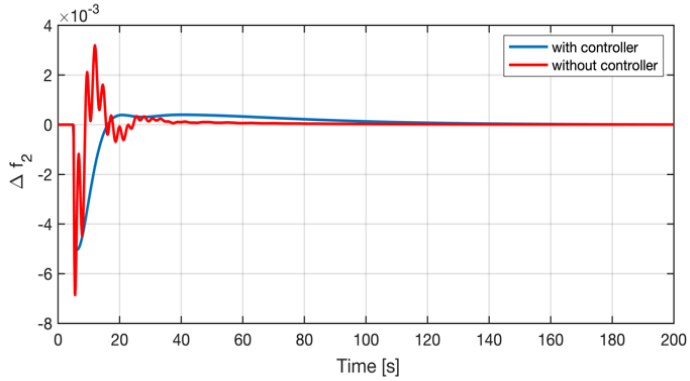

Figure 63. Frequency deviation in second area as a result of fault in tie line

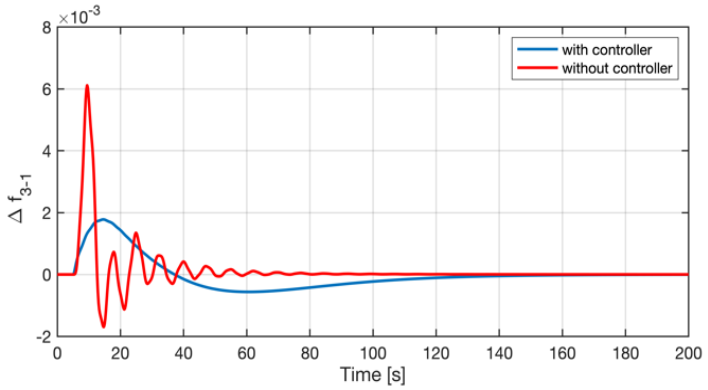

Figure 64. Frequency variation in third area by cause of fault in tie line

A loop shape large-scale power system decomposed to three subsystems. Each subsystem is identified by a lower order model based on their inputs number in a given structure. A servomechanism disturbance rejection controller based on oscillation modes of the system is designed for each subsystem and applied to the original system. We show that inter-area oscillations are well damped by designed controller. Also, the simulation results confirm that servomechanism controller is more robust to delay in the system. For future works, to improve the controller design in this system, two approaches exist: (i) improve the system identification approach to decrease the identification error in the system; (ii) employ more accurate control design approaches for this case.

CHAPTER SIX

LARGE-SCALE BATTERY ENERGY STORAGE DYNAMICAL MODELING FOR POWER SYSTEM STABILITY ANALYSIS

6.1. Introduction

The increasing penetration of renewable energy sources in the grid can raise the likelihood of instability in the power grid, e.g. small signal and voltage instability incidents. To study

the effect of BESS integration on the grid and power system behavior, especially for stability analysis, accurate battery modeling plays a key role. In [74] EPRI proposed a generic model based on [75] for small signal stability analysis. This model in fact, is a combination of several PI controllers and saturation that model the constant active and reactive power injection to the power grid. the main assumptions in this model are: *i:* the battery dynamic and chemistry are ignored and *ii:* the details in DC side of the battery is ignored. In another study, the dynamic model for large-scale batteries and their integration in power grids was first proposed in [76]. In this model, the battery was represented by a constant voltage source parallel to a resistance and capacitor (RC) circuit. The model was later improved and implemented in power system studies [76]-[77]. The proposed model in [77] has been used in research studies for load frequency control and power system stability analysis [78]- [80]. However, nonlinearity is the major disadvantage of the battery model in [78] as it complicates the stability analysis. Moreover, in the majority of the existing literature, BESS is studied as an additional active power source from real power and frequency variation points of views, while the major advantage of BESS is the fact that both its active power and power factor are adjustable and controllable by the firing angle of the thyristors in the inverter. Therefore, by controlling the inverter, it is possible to have reactive power injection in the power system. As the reactive power directly affects the voltage deviation in power systems, unstudied reactive power flow may cause voltage instability in the network. Hence, in power systems small signal stability analysis, *d-q* models of power system components in state space representation must be developed.

As the majority of power system studies, including small signal stability analysis, is carried out in the *d-q* axes, a precise model of the battery in the *d-q* axes is necessary. The lack of parametric based models of the battery in *d-q* axes makes stability analysis more challenging especially as the contributions of batteries in power systems are growing rapidly. In this paper, we develop an analytical model for the battery and its inverter in *d-q* axes. In this study, a new modeling approach using *d-q* analysis is used for batteries integration to the power grid. A state space representation of the battery energy storage model accompanied by an inverter in the *d-q* axes is presented. The inverter firing angle is considered as an input to enable the control of the battery's power factor. The advantages of the proposed model with respect to the other battery models [77] – [81] are: *i)* the reactive power has been considered such that grid voltage deviations can be taken into account, and *ii)* the state space model of the battery has been represented in *d-q* structure, which utilize the stability analysis in the power system.

6.2. Power System Model

Small signal stability in a power system is defined as the ability of the power system to maintain synchronism in the presence of small disturbances such as load deviations. In this context, since the power system is inherently a nonlinear system, the power system model is linearized in the vicinity of its operating point for the small signal analysis. This enables us to apply linear system theory to the power system even though the system is inherently nonlinear. In this regard, all power system components can be modeled in the state space representation as:

$$\begin{cases} \dot{x} = Ax + Bu \\ y = Cx + Du \end{cases} \tag{66}$$

A general power system structure is shown in Fig. 65. Based on the given model, we can define the general equation of the system as:

$$[Y_{bus}]\Delta v_t = \Delta I_G - \Delta I_L - \Delta I_S + \Delta I_B \tag{67}$$

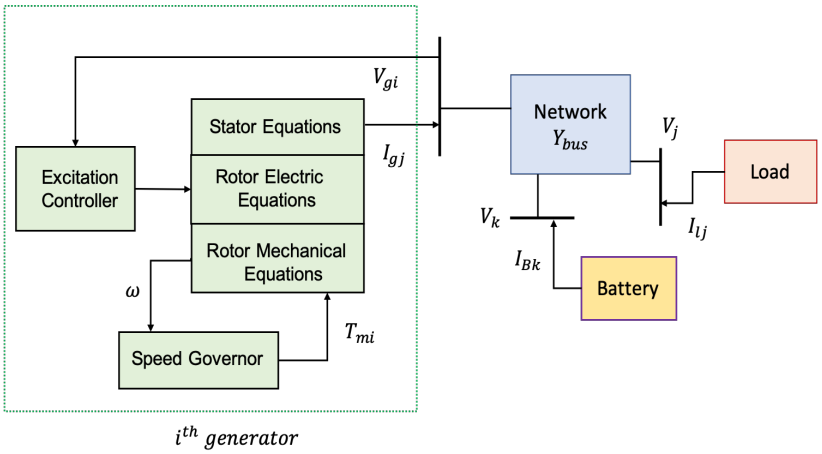

Figure 65. Power system Structure

where, Y_{bus} is the power system admittance matrix, Δv_t is the voltage deviation in the buses and $\Delta I_G, \Delta I_L,\ \Delta I_S,$ and ΔI_B are the changes in generator, load, static var compensator (SVC) and battery current injections to the power system, respectively.

Generator Model

The generator model in state space representation varies based on the modeling approaches chosen [82]– [83]. For instance, in [82] the generator is represented with five states as:

$$\Delta \mathrm{x_g} = \left[\Delta\delta, \Delta\omega, \Delta E'_d, \Delta E'_q, \Delta E_{fd}\right]$$

where, δ is rotor angle, ω is the rotational speed, $\Delta E'_d$ and $\Delta E'_q$ are the d and q axes generator internal voltages and ΔE_{fd} is the field voltage. The order of the generator model can increase to 16 states as the generator model includes the exciter, power system

stabilizer (PSS), and turbine dynamics. The generator differential equations after linearization are:

$$\begin{cases} \Delta\dot{x}_g = [A_g]\Delta x_g + [B_g]\Delta V_g + [E_g]\Delta u_{cg} \\ \Delta I_g = [C_g]\Delta x_g + [D_g]\Delta V_g \end{cases} \quad (68)$$

where ΔV_g represents the voltage deviation in the generator bus, ΔI_g is the generator current deviation and Δu_{cg} is a small perturbation in the generator reference input variables for the generator controllers. Note that, ΔI_g, and ΔV_g are represented in *d-q* axes as

$$\Delta I_g = \begin{bmatrix} \Delta I_{dg} \\ \Delta I_{qg} \end{bmatrix} \text{ and } \Delta V_g = \begin{bmatrix} \Delta V_{qg} \\ \Delta V_{dg} \end{bmatrix}$$

To be able to study the power system, all other equipment such as loads, SVCs and batteries should be written in $d-q$ format. These devices are modeled in state space representation in the following subsections.

Load Model

Power system loads including induction motors and nonlinear loads are modeled as

$$\begin{cases} \Delta\dot{x}_l = [A_l]\Delta x_l + [B_l]\Delta V_l + [E_l]\Delta u_{cl} \\ \Delta I_l = [C_l]\Delta x_l + [D_l]\Delta V_l \end{cases} \quad (69)$$

where, Δx_l are the dynamic loads such as induction motor states and Δu_{cl} are the load control inputs. ΔV_l is the load bus voltage deviation and ΔI_l is the load (demand) current deviation. For the static loads the equation will be simplified to

$$\Delta I_l = [D_l]\Delta V_l = [Y_l]\Delta V_l \quad (70)$$

Static Var Compensator (SVC) model

Similar to the load equations, static var compensator (SVC) in state space representation is modeled as

$$\begin{cases} \Delta\dot{x}_s = [A_s]\Delta x_s + [B_s]\Delta V_s + [E_s]\Delta u_{cs} \\ \Delta I_s = [C_s]\Delta x_s + [D_s]\Delta V_s \end{cases} \quad (71)$$

where, Δx_s are the SVC states and Δu_{cs} are the SVC control inputs. ΔV_s and ΔI_s are the SVC bus voltage and current deviations, respectively.

Battery model

To add the battery dynamics to the power system model, the battery also should be represented as

$$\begin{aligned} \Delta\dot{x}_b &= [A_b]\Delta x_b + [B_b]\Delta V_b + [E_b]\Delta u_{cb} \\ \Delta I_b &= [C_b]\Delta x_b + [D_b]\Delta V_b \end{aligned} \quad (72)$$

Remark1: Note that all equations are in d-q axes, hence:

$$\Delta I_{(.)} = \begin{bmatrix} \Delta I_d \\ \Delta I_q \end{bmatrix} \text{ and } \Delta V_{(.)} = \begin{bmatrix} \Delta v_q \\ \Delta v_d \end{bmatrix} \quad (73)$$

where $\Delta V_{(.)}$ represents voltages deviations in load, SVC or the battery buses, $\Delta I_{(.)}$ is the current deviations and $\Delta u_{c(.)}$ is the small perturbation in their reference input variables.

Network Equations

As shown in Fig. 1, generators and loads in the power system network are interfaced to the network as current injections This leads us to following equation

$$[Y_{bus\_DQ}]\Delta V_{QD} = [P_G]\Delta I_G - [P_L]\Delta I_L - [P_S]\Delta I_S + [P_B]\Delta I_B \quad (74)$$

Y_{bus_DQ} is the network admittance matrix in *d-q* axes and $P_g(i,j) = \begin{bmatrix} 1 & 0 \\ 0 & 1 \end{bmatrix}$ if the i^{th} generator is connected to the j^{th} bus, otherwise $P_g(i,j) = \begin{bmatrix} 0 & 0 \\ 0 & 0 \end{bmatrix}$. Same interfacing matrices are defined for P_l, P_{svc}, and P_B [82]-[83].

After substituting the equations (68), (69), (71) and (72) in (74) and simplifying, the overall system representation becomes

$$\dot{X} = [A_t]X + [E]U_c \tag{75}$$

where

$$A_t = [A] + [B][P]^t[Y'_{bus_{DQ}}]^{-1}[P][C] \tag{76}$$

$$[P] = [P_G\ P_L\ P_S\ P_B] \tag{77}$$

and

$$\left[Y'_{bus_{DQ}}\right]\Delta V_{QD} = [P_G][C_G][X_G] + [P_L][C_L][X_L] + [P_S][C_S][X_S] + [P_B][C_B][X_B] \tag{78}$$

A_t represents the state matrix of the entire power grid, and the stability of the system is studied based on A_t.

To be able to study the effect of the battery integration on the power system stability, we need to model the battery in the state space model structure given in (72). Then we will be able to add the battery model to the power system model in (74). For this purpose, we derive the BESS current equations in *d-q* axes and linearize them in the vicinity of the operating point

6.3. Battery's Linear Model

Large-scale batteries are accompanied by their inverters in power grids [77]. Figure 66 shows the equivalent circuit model of a battery and its inverter. To extract the state space model of the battery, we consider two cases for the charging and discharging modes. The

dynamics of the battery in the charging mode are slightly different from the discharging model.

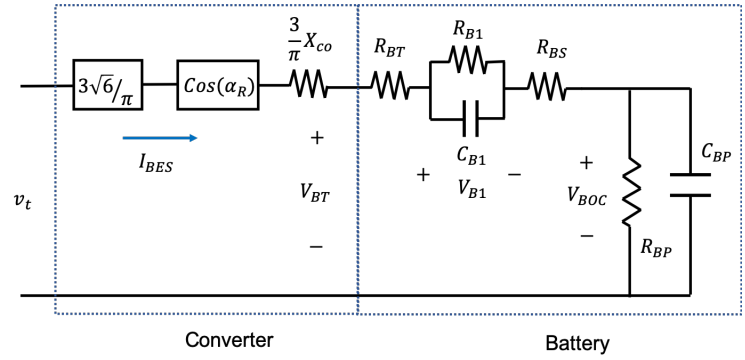

Figure 66. Battery and inverter circuit model

In the first case, we obtain the state space model of the battery for the charging scenario. In the second case, with slight modifications, we obtain the discharging model from the first case.

6.3.1. Charging Mode

In the charging mode, using Kirchhoff's voltage law, the output voltage of the battery, V_{BT}, is

$$V_{BT} = \frac{3\sqrt{6}}{\pi} v_t \, cos(\alpha_R) - \frac{3}{\pi} x_{co} I_{BES} \tag{79}$$

where, I_{BES} is the battery's terminal current. The dynamic model of the battery for the charging mode is shown in Fig. 61, where, α_R is the inverter firing angle and v_t is the bus voltage to which the battery is connected.

Defining $\lambda = 1 + \frac{3}{\pi R} x_{co}$, and $\mathrm{R} = \mathrm{R_{BS}} + \mathrm{R_{BT}}$ the battery current is

$$I_{BES} = \frac{3\sqrt{6}}{\pi \lambda R} v_t \, cos(\alpha_R) - \frac{1}{\lambda R} V_{BOC} - \frac{1}{\lambda R} V_{B1} \tag{80}$$

where V_{B1} is the battery overvoltage, and V_{BOC} is the battery open circuit voltage. In the nonlinear model of the battery represented in Fig. 67, we consider $x_b = [V_{BOC}, V_{Bq}, \alpha_R]^T$ as the state vector of the battery.

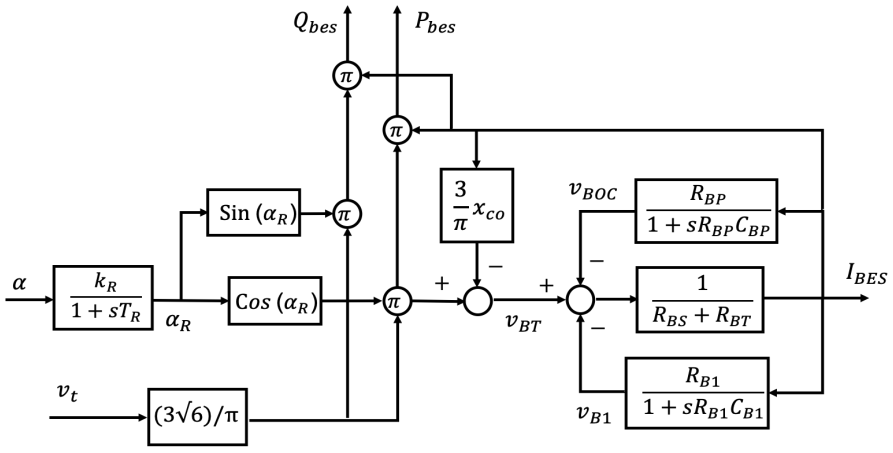

Figure 67. Battery and inverter dynamic model in the charging mode

By linearizing (80) in the vicinity of the operating point of $\alpha_R = \alpha_{r0}$, $v_t = v_{t0}$, $V_{BOC} = V_{boc0}$, $V_{B1} = V_{b10}$, and $I_{BES} = I_{b0}$, the current deviation is

$$\Delta I_{BES} = \frac{3\sqrt{6}}{\pi\lambda R} cos(\alpha_{r0})\, \Delta\, v_t - \frac{3\sqrt{6}}{\pi\lambda R} v_{t0}\, sin(\alpha_{r0})\ \Delta\alpha_R - \frac{1}{\lambda R}\Delta V_{BOC} - \frac{1}{\lambda R}\Delta V_{B1} \tag{81}$$

Moreover, using the dynamic block diagram shown in Fig. 61, we have the following state dynamics

$$\Delta\dot{V}_{BOC} = \frac{1}{C_{BP}}\ \Delta I_{BES} - \frac{1}{C_{BP}R_{BP}}\ \Delta V_{BOC} \tag{82}$$

$$\Delta\dot{V}_{B1} = \frac{1}{C_{B1}}\ \Delta I_{BES} - \frac{1}{C_{B1}R_{B1}}\ \Delta V_{B1} \tag{83}$$

$$\Delta\dot{\alpha}_R = \frac{k_R}{T_R}\ \Delta\alpha - \frac{1}{T_R}\ \Delta\alpha_R \tag{84}$$

Now, considering

$$P_{BES} = \frac{3\sqrt{6}}{\pi}\ v_t\ I_{BES}\ cos\ (\alpha_R) \tag{85}$$

$$Q_{BES} = \frac{3\sqrt{6}}{\pi} v_t I_{BES} sin(\alpha_R) \quad (86)$$

$$I_{bd} = \frac{v_{td}P_{BES} - v_{tq}Q_{BES}}{v_t^2} \quad (87)$$

$$I_{bq} = \frac{v_{tq}P_{BES} + v_{td}Q_{BES}}{v_t^2} \quad (88)$$

$$v_t = \sqrt{v_d^2 + v_q^2} \quad (89)$$

The final state space representation of the battery dynamics and its inverter can be summarized as (85)-(89) in the vicinity of its operating point. In this state space model, the states are the deviation values of nonlinear states as $\Delta x_b = [\Delta V_{BOC}, \Delta V_{Bq}, \Delta\alpha_R]^T$. The input reference control for the battery is defined as $\Delta u_{cb} = \Delta\alpha$, which controls the active and reactive output power of the battery. The outputs are active (ΔI_{bd}) and reactive (ΔI_{bq}) current deviations of the battery. Note that the voltage input signal is in d-q axes as $\Delta v = [\Delta v_q, \Delta v_d]^T$. Note that Δv is the battery terminal voltage deviation as a result of the battery connection to the power grid.

$$\begin{bmatrix} \Delta\dot{V}_{BOC} \\ \Delta\dot{V}_{B1} \\ \Delta\dot{\alpha}_R \end{bmatrix} = A_b \begin{bmatrix} \Delta V_{BOC} \\ \Delta V_{B1} \\ \Delta\alpha_R \end{bmatrix} + B_b \Delta v + E_b \Delta u_{cb} \quad (90)$$

$$\begin{bmatrix} \Delta I_{bd} \\ \Delta I_{bq} \end{bmatrix} = C_b \begin{bmatrix} \Delta V_{BOC} \\ \Delta V_{B1} \\ \Delta\alpha_R \end{bmatrix} + D_b \Delta v \quad (91)$$

where

$$A_b = \begin{bmatrix} \left(\frac{-1}{R_{BP}C_{BP}} - \frac{1}{R\lambda C_{BP}}\right) & \frac{-1}{R\lambda C_{BP}} & \frac{-3\sqrt{6}.v_{t0}}{\pi R\lambda C_{BP}} sin(\alpha_{r0}) \\ \frac{-1}{R\lambda C_{B1}} & \left(\frac{-1}{R_{B1}C_{B1}} - \frac{1}{R\lambda C_{B1}}\right) & \frac{-3\sqrt{6}.v_{t0}}{\pi R\lambda C_{B1}} \sin(\alpha_{r0}) \\ 0 & 0 & \frac{-1}{T_R} \end{bmatrix} \quad (92)$$

$$B_b = \begin{bmatrix} \frac{3\sqrt{6}\ v_{q0}}{\pi\lambda C_{BP} v_{t0}} cos\ (\alpha_{r0}) & \frac{3\sqrt{6}\ v_{d0}}{\pi\lambda C_{BP} v_{t0}} cos\ (\alpha_{r0}) \\ \frac{3\sqrt{6}\, v_{q0}}{\pi R\lambda C_{B1} v_{t0}} cos\ (\alpha_{r0}) & \frac{3\sqrt{6}.\, v_{d0}}{\pi R\lambda C_{B1} v_{t0}} cos\ (\alpha_{r0}) \\ 0 & 0 \end{bmatrix} \quad (93)$$

$$E_b = \begin{bmatrix} 0 \\ 0 \\ \frac{k_R}{T_R} \end{bmatrix} \quad (94)$$

Finally, the terms of $C_b = [C_{bij}]$ and $D_b = [D_{bij}]$ matrices (ij representing the i^{th} and j^{th} columns) are as follows

$$C_{b11} = \frac{-3\sqrt{6}\, v_{d0}}{\pi R\lambda v_{t0}} cos(\alpha_{r0}) + \frac{3\sqrt{6}\, v_{q0}}{\pi R\lambda v_{t0}} sin(\alpha_{r0}) \quad (95)$$

$$C_{b12} = \frac{-3\sqrt{6}\, v_{d0}}{\pi R\lambda v_{t0}} cos(\alpha_{r0}) + \frac{3\sqrt{6}\, v_{q0}}{\pi R\lambda v_{t0}} sin(\alpha_{r0}) \quad (96)$$

$$C_{b13} = \frac{-54}{\pi^2 R\lambda} v_{d0}.sin\ (2\alpha_{r0}) - \frac{54}{\pi^2 R\lambda} v_{q0}.cos\ (2\alpha_{r0}) + \frac{3\sqrt{6}}{\pi R\lambda v_{t0}} (V_{boc0} + V_{b10})[v_{d0}.sin\ (\alpha_{r0}) + v_{q0}.cos\ (\alpha_{r0})] \quad (97)$$

$$C_{b21} = \frac{-3\sqrt{6}\, v_{q0}}{\pi R\lambda v_{t0}} cos(\alpha_{r0}) - \frac{3\sqrt{6}\, v_{d0}}{\pi R\lambda v_{t0}} sin(\alpha_{r0}) \quad (98)$$

$$C_{b22} = \frac{-3\sqrt{6}\, v_{q0}}{\pi R\lambda v_{t0}} cos(\alpha_{r0}) - \frac{3\sqrt{6}\, v_{d0}}{\pi R\lambda v_{t0}} sin(\alpha_{r0}) \quad (99)$$

$$C_{b23} = \frac{54}{\pi^2 R\lambda} v_{d0}.cos\ (2\alpha_{r0}) - \frac{54}{\pi^2 R\lambda} v_{q0}.sin\ (2\alpha_{r0}) + \frac{3\sqrt{6}}{\pi R\lambda v_{t0}} (V_{boc0} + V_{b10})[v_{q0}.sin\ (\alpha_{r0}) - v_{d0}.cos\ (\alpha_{r0})] \quad (100)$$

and

$$D_{b11} = \frac{-27}{\pi^2 R\lambda} sin\ (2\alpha_{r0}) + \frac{3\sqrt{6}}{\pi R\lambda v_{t0}^3} [v_{d0}^2\ sin(\alpha_{r0}) + v_{d0} v_{q0} cos\ (\alpha_{r0})](V_{boc0} + V_{b10}) \quad (101)$$

$$D_{b12} = \frac{54}{\pi^2 R\lambda}\ cos^2(\alpha_{r0}) - \frac{3\sqrt{6}}{\pi R\lambda v_{t0}^3} [v_{q0}^2\ cos(\alpha_{r0}) + v_{d0} v_{q0} sin\ (\alpha_{r0})](V_{boc0} + V_{b10}) \quad (102)$$

$$D_{b21} = \frac{54}{\pi^2 R\lambda}\ cos^2(\alpha_{r0}) - \frac{3\sqrt{6}}{\pi R\lambda v_{t0}^3}[v_{d0}^2\, cos(\alpha_{r0}) - v_{d0}v_{q0}\ sin\ (\alpha_{r0})](V_{boc0} + V_{b10})(103)$$

$$D_{b22} = \frac{27}{\pi^2 R\lambda}\ sin\ (2\alpha_{r0}) - \frac{3\sqrt{6}}{\pi R\lambda v_{t0}^3}[v_{q0}^2 sin(\alpha_{r0}) - v_{d0}v_{q0}\ cos(\alpha_{r0})](V_{boc0} + V_{b10})\ (104)$$

Having derived the state space model for the battery in the charging mode, we derive a similar model for the discharging case.

6.3.2. Discharging Mode

To modify the charging model in Fig. 61 for the discharging mode two slight changes are required: *i)* changing the firing angle to $\beta = \pi - \alpha$; and *ii)* changing the current flow direction. Therefore, the obtained battery voltage is

$$V_{BT} = V_{BOC} - V_{B1} - (R_{BT} + V_{BS})I_{BES} \quad (105)$$

Considering the inverse flow of the current, I_{BES} has negative value in the equation (82). So, (105) can be modified to

$$V_{BT} = V_{BOC} - V_{B1} + (R_{BT} + V_{BS})I_{BES} \quad (106)$$

6.2.3. Simulation Results

To validate the credibility of the obtained linearized model in *d-q* axes, simulations were conducted to compare the behavior against the original model. For brevity, only the results for the charging mode are discussed. The discharging mode has the same quality of results. In the simulation study, the following system operating conditions were considered: $v_{tq0} = 100\ V$,

$v_{td0} = 692.82\ V$, $v_{t0} = 700\ V$, and $\alpha_0 = 15°$.

At this operating point, a small perturbation on the firing angle of the inverter with the value of $\Delta\alpha = -1.97°$ was considered. Figure 68 compares the results of the state vector $x_b = [V_{BOC}, V_{Bq}, \alpha_R]^T$ in both models. The states in the original model are shown in blue and states of the linearized *d-q* axis model are depicted with red.

All states start with the same initial conditions as both models were in the same operating points. The slopes of deviations are very close to each other and there are slight differences in the final values.

The bias errors are mainly noticeable in the steady state because of the linearization approximation whereas the application of this model is for transient behavior in small signal analysis for no more than a few minutes time duration.

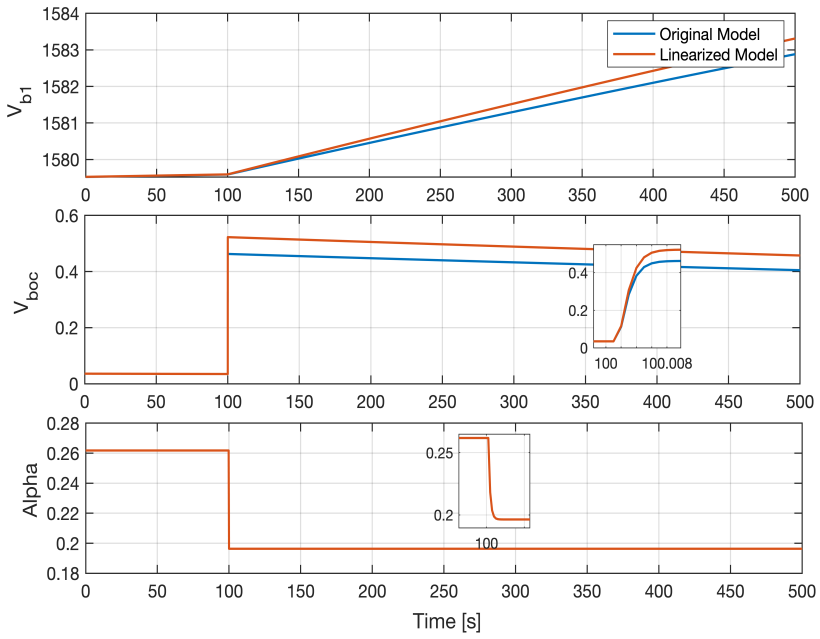

Figure 68. Open circuit voltage of the battery

In the original model depicted in Fig. 66, there is no direct access to measure the *d-q* axis currents of the battery. Therefore, to validate the output signals of the obtained model, we

compute these currents by solving the following equations for active and reactive power, which approximates (107)-(108) as

$$P_{BES} = v_{td} I_{bd} + v_{tq} I_{bq} \tag{107}$$

and

$$Q_{BES} = v_{td} I_{bq} - v_{tq} I_{bd} \tag{108}$$

The battery current in d and q axes (I_{bd}, and I_{bq}) of the original model and the linearized model are shown in Fig. 69. The linearized model results are close to the original model, particularly in the transient time frame that would be employed in small signal stability studies.

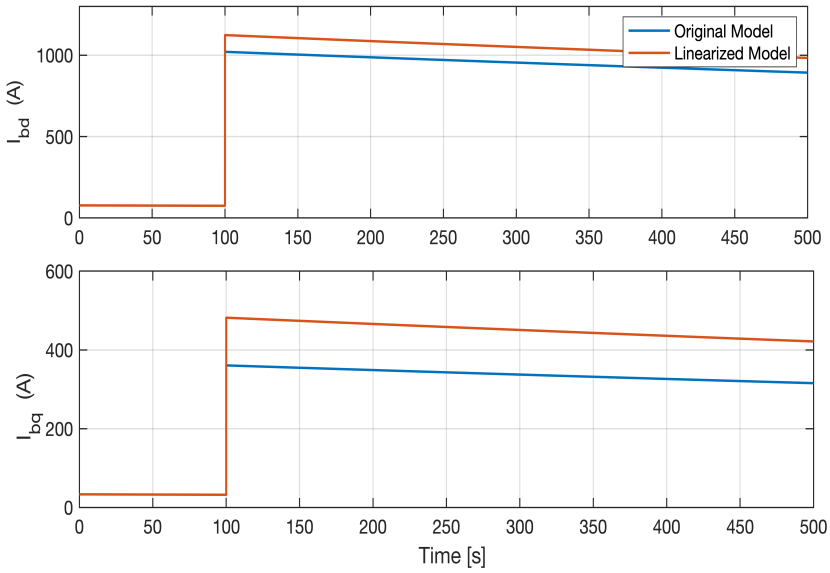

Figure 69. Battery d axis output current

Finally, the effect of the linearized battery integration to the power grid is investigated on the two-area case study model and the results are shown in Fig. 70. It is shown that the battery connection has improved the stability and transient behavior of the system.

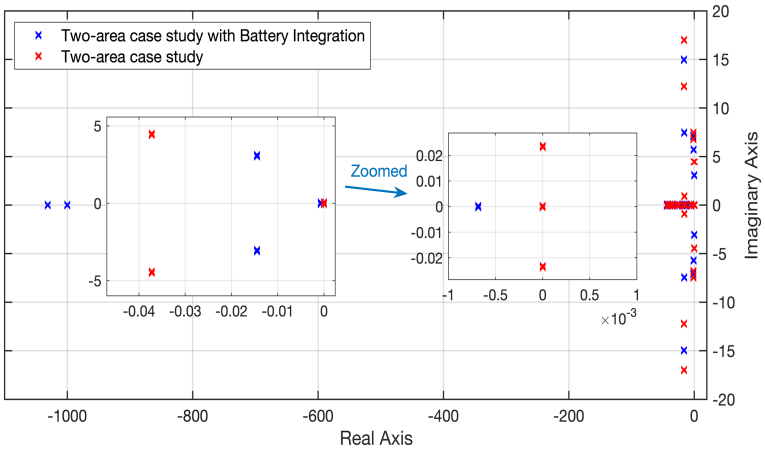

Figure 70. Two-area case study model eigenvalue analysis in presence of the battery

Considering the dynamic model of the battery for charging and discharging mode allows us to have full control on four quadrants of active and reactive power. Four quadrant control means the real current flow directions can represent either charging or discharging states, while the reactive current flows can represent either supplying or absorbing reactive power simultaneously and independently (see Fig. 71).

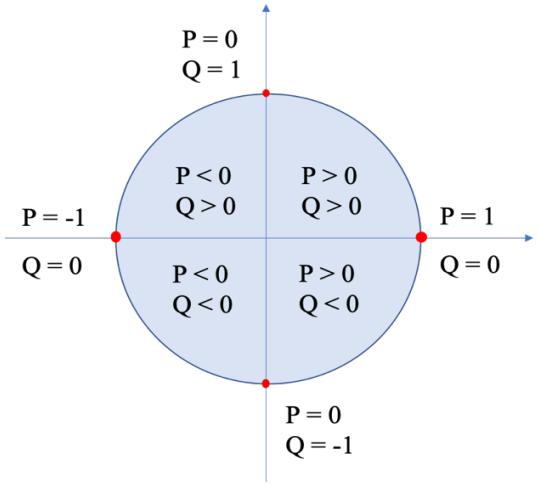

Figure 71. BESS Four quadrant control and operation diagram

By implementing proper control strategy, the BESS can provide the following functionalities in the power grid based on system requirements [84]:

1. Voltage control and regulation at the local terminals of the BESS, at the point of interconnection (POI) or plant level (when incorporated in a power plant).
2. Frequency support by quickly providing or absorbing real power or being part of automatic generation control (AGC).
3. Spinning reserves, non-spinning reserves, or supplemental reserves. Generation capacity over and above customer demand is reserved for use in the event of contingency events like unplanned outages. Many storage technologies can be quickly synchronized to grid frequency through power electronics control, so they can provide a service equivalent to spinning reserves with minimal to zero standby losses (unlike the idling generators). Energy storage is also capable of providing non-spinning or supplemental reserves.
4. Power oscillation damping which is the objective of this research. BESS can be used to damp or alleviate power oscillations if the proper supplemental controls are deployed, and the BESS is strategically located in the transmission system to be able to affect the modes of oscillation of concern.

Large-scale battery control schematic in power system considering the charge/discharge model, which will be able to provide active and reactive power in lead/lag form, is shown in Fig. 66. In this model A_c and A_d represent the state metrices of the whole system in charging and discharging modes respectively.

CHAPTER SEVEN

CONTROL DESIGN

7.1. Introduction

The complexity of the power system is a significant challenge to design and implement proper control. There are several approaches to design control for a given system. Each of these approaches has its advantages and disadvantages to other approaches that highlight their effectiveness for specific applications. Optimal control deals with finding a control law for a given system such that a specific optimality criterion is achieved. The control problem includes a cost function that is a function of the system's states and control variables. As in this research, we are looking for a control approach to be able to deal with frequency deviation as the main output of the system along with the battery's active and reactive power output, which is limited due to its output power capacity and energy price, optimal control approach is considered as the control approach to design the optimal control for the batteries.

Considering the large-scale battery integration to the power grid, and the necessity of switching between charging/discharging scenarios implies the centralized control's effectiveness to optimally schedule the batteries output power and operating power factor to suppress the frequency deviation at minimum cost. However, the power system's complexity is a significant challenge to design and implement a proper centralized control. On the other hand, decentralized control methods have been widely used in power systems

as more practical control strategies compared to centralized control methods in large-scale systems. In a decentralized control design, no information exchange among different areas is necessary to establish a subsystem controller. Also, any inputs to the subsystem other than local inputs are considered as perturbations [85]. This makes the control design and implementation easier in large power systems.

Another important factor that we need to consider in control design is the measurability of the system states. In most systems, especially large-scale systems such as the power system, it is practically or economically almost impossible to measure systems' states. Observer design and implementation give a close estimation of the system state information; however, large-scale systems generally experience higher estimation errors or convergence problems. To overcome these challenges, the decentralized observer approach is introduced and implemented for large-scale systems [86]-[87]. Another practical approach is output feedback control, which is based on the system's measurable data, allowing us to design a decent controller for the large-scale system [88]- [90].

Finally, considering the large-scale battery integration to the power grid and the different charging/discharging dynamic models of the large-scale battery introduced in the previous section, and the necessity of switching between charging/discharging scenarios, the power system dynamic model converts to the hybrid system model [91]. Therefore, considering the case study model's hybrid nature, we need to design a hybrid optimal control for the case study system to optimize system response.

This section design and implement four different optimal control approaches to compare each control's pros and cons for the case study model to benefit selecting the best control approach based on our system characteristics and our objectives.

To design the control for the case study model, which simulates a large-scale interconnected power system, we assume a large-scale battery is connected to each area as shown in Fig. 72. The firing angles of the batteries' inverters are considered as control input signals. The control inputs schedule the batteries' active and reactive power, so batteries inject/absorb both active are reactive power to/from the power grids as needed. The system has three batteries, which implies eight different possible scenarios for batteries charging and discharging modes.

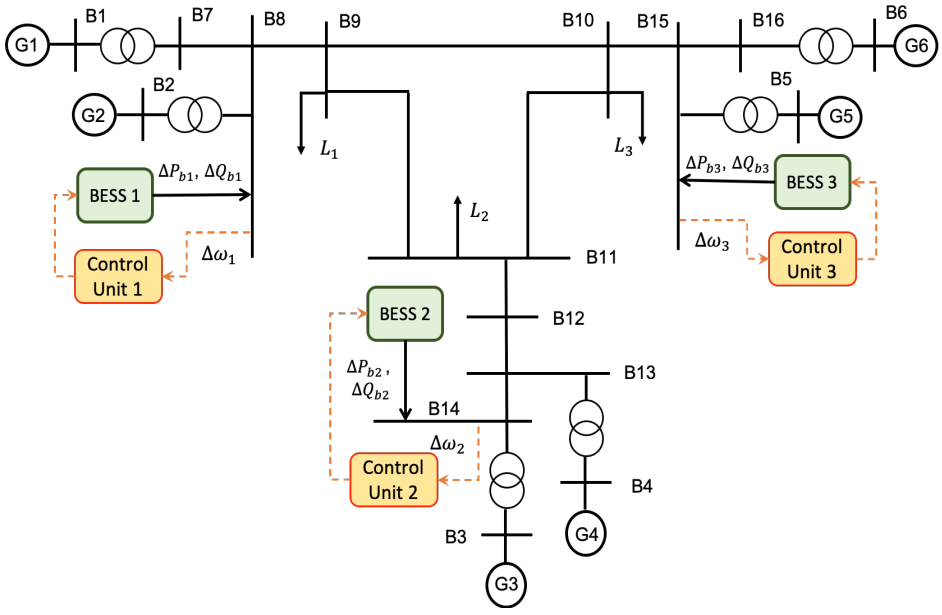

Figure 72. Battery integration to the three-area case study model

7.2. Centralized State Feedback Control

To design a centralized state feedback control approach for the case study model, we assume the system as

$$\begin{cases} \dot{x} = Ax + Bu \\ y = Cx + Du \end{cases} \tag{109}$$

The cost function for the system is

$$min\, J_j = \int_{t_{k-1}}^{t_k} (x^T\, Q\, x + u^T\, R\, u)\; d\tau \qquad \text{for } j = 1{:}\,8 \tag{110}$$

Where x is system state vector, u is batteries inverter firing angle deviation vector and j represents each possible scenario for the batteries operation. Q and R are the weighting matrices for the system states and inputs, respectively. These matrices help to design a control law based on system requirements and constraints.

Control system law for system (109) based with cost function of (110) is defined as

$$u = Kx \tag{111}$$

$$K = -R^{-1}B^T P \tag{112}$$

$$\hat{A}^T P + P\hat{A} = -\hat{Q} \tag{113}$$

$$\hat{A} = A + BK \tag{114}$$

$$\hat{Q} = Q - PBR^{-1}B^T P \tag{115}$$

System in each time step faces eight optimal value for different scenarios of battery operation. To find the final optimum batteries operation policy, a switching policy is considered to shift between charging and discharging conditions to minimize the cost function in each time interval of (t_{k-1}, t_k) and consequently the total cost function of the batteries operation in the power system. The update time interval will be a trade-off

between the frequency deviation damping period and the battery's switching capability. The hybrid controller selects the scenario with minimum cost function as the operating mode for the time interval. Then, the system's states are updated based on the selected mode and the selected LQR controller. The objective of the control design is to damp the generators' frequency deviation using the inputs.

By calculating the control law and implementing the control in our case study model, the frequency deviation of the second generator will be as Fig. 73. To clearly show the results and batteries operations, batteries operation for two extreme cases and the final batteries operation have been plotted.

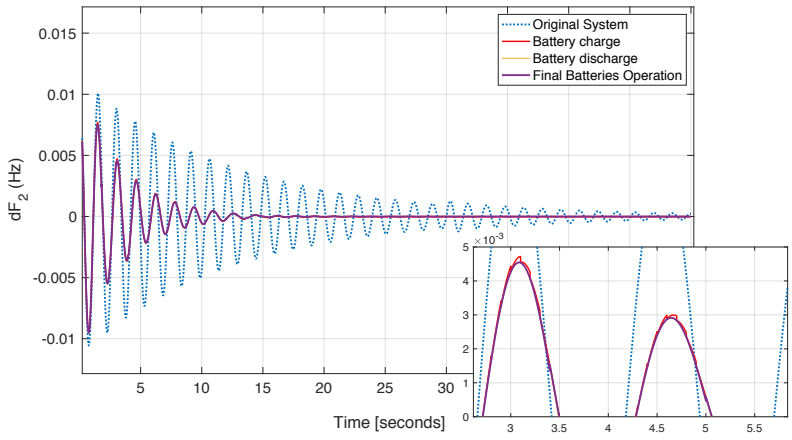

Figure. 73 Frequency deviation of the generator two in the first area for; (i) original system, (ii) all battery charging scenario, (iii) all battery discharging scenario, and (iv) final batteries operation

7.3. Decentralized State Feedback Control

In this section we assume i) we only have access to the local subsystem information and ii) all subsystem states are not measurable. To design a decentralized state feedback control,

we need to have a decent estimation of the system states, so at first step, a decentralized observer is designed for each subsystem.

7.3.1. Step 1: Decentralized Observer Design

It is showen that the existing regulator and servomechanism theories can be modified to take into account the presence of persistent fluctuating disturbances and design a deterministic controller which consistently maintains set-point regulation, or servo tracking for a broad class of realistic external disturbances. Later several approaches are developed based on Johnson study to design decentralized observer for a complex system [87]. These methods mainly developed based on the assumption of the interconnectivity of the system and measurements on the system local and global inputs and/or outputs. Assuming that we have access to the system (116) input and output measurements, we will be able to design a partially decentralized observer by following instruction. Considering that system in (109) has three subsystems, each subsystem $i, i \in N,$ has the following dynamics

$$\begin{cases} \dot{x}_i = A_i x_i + B_i u_i + \sum_{j=1}^{N} A_{ij}\, x_j \\ y_i = C_i x_i \end{cases} \qquad i \in N \tag{116}$$

The system in (116) can be written as

$$\begin{cases} \dot{x}_i = A_i x_i + V_i \zeta_i + B_i u_i \\ \dot{\zeta}_i = G_i x_i + F_i \zeta_i + W_i w_i \end{cases} \tag{117}$$

$$\begin{cases} y_i = C_i x_i \\ \eta_i = H_i \zeta_i \end{cases} \tag{118}$$

$x \in R^n, u \in R^n,$ and $y \in R^m$

For the system in (116) there exists a decentralized and asymptotically stable observer if and only if

$$\text{i) Rank}\begin{bmatrix} C_i & 0 \\ C_iA_i & 0 \\ H_iG_i & H_iF_i \\ 0 & H_i \\ 0 & V_i \end{bmatrix} = \text{Rank}\begin{bmatrix} C \\ CA \end{bmatrix} \tag{119}$$

$$\text{ii) Rank}\begin{bmatrix} \lambda I - A_i \\ C_i \end{bmatrix} = n_i \text{ for all } \lambda \text{ with } Re(\lambda) \geq 0 \tag{120}$$

The observer for each subsystem is obtained as

$$\hat{\dot{x}}_i = \xi_i + M_i y_i + X_i \eta_i \tag{121}$$

$$\dot{\xi}_i = (A_i - L_iC_i)\xi_i + T_iB_iu_i + [(A_i - L_iC_i)M_i + L_i + N_i)y_i + U_iW_iw_i + [(A_i - L_iC_i)X_i + Z_i]\eta_i \tag{122}$$

$T_i, U_i, N_i, M_i, X_i \; and \; Z_i$ are calculated from

$$[T_i \quad U_i \quad N_i \quad M_i \quad X_i \quad Z_i]\begin{bmatrix} I & 0 & 0 & 0 \\ 0 & I & 0 & 0 \\ 0 & 0 & C_i & 0 \\ C_i & 0 & C_iA_i & C_iV_i \\ 0 & H_i & H_iG_i & H_iF_i \\ 0 & 0 & 0 & H_i \end{bmatrix} =$$

$$[I \quad 0 \quad 0 \quad V_i] \tag{123}$$

By having a proper estimation of system dynamic, we will be able to design a control system such that the system has the required performance in presence of the disturbances.

Knowing that the case study model is an interconnected system, in the next step, a decentralized state feedback control for the interconnected system is designed for each area.

7.3.2. Step 2: Decentralized Control

In interconnected systems, the optimality of the system is a complicated context in the presence of some essential uncertainties among the subsystems, which cannot be described in either deterministic or stochastic terms. Unlike standard optimization schemes where robustness is a part of the solution, robustness in complex systems is a part of the problem and it has to be considered in the design process.

The case study model in (109) can be rewritten in compact form as

$$\dot{x} = A_D x + B_D u + A_C x \tag{124}$$

System consists of three subsystems, $N = 3$, where $x \in R^n$, $u \in R^p$, and $y \in R^m$ are states, inputs and outputs of the system. The dynamics of the decoupled part of the system in (124) can be written as

$$\dot{x} = A_D x + B_D u \tag{125}$$

and its subsystems are

$$\dot{x}_i = A_i x_i + B_i u_i \qquad i \in N \tag{126}$$

where (A_D, B_D) are controllable, A_D is a block diagonal matrix that represents the state matrices of the subsystems and A_C defines the interconnection matrix between the subsystems [85].

$$A_D = diag(A_{D1}, A_{D2}, \dots, A_{DN}) \qquad i \in N \tag{127}$$

Let us consider the state and input weighting matrices as

$$Q_D = diag(Q_1, Q_2, \dots, Q_N) \tag{128}$$

$$R_D = diag(R_1, R_2, \dots, R_N) \tag{129}$$

where Q_D is symmetric nonnegative definite, and R_D is a symmetric positive definite matrix. The optimal control law for system in (125) and total cost function of the system are $u_D^* = -K_D x$, and $J_D = \sum_{i=1}^{N} J_i$, where, J_i is an individual cost function for subsystem i as

$$J_i(x_{i0}, u_i) = \int_0^t (x_i^T Q_i x_i + u_i^T R_i u_i) d\tau \tag{130}$$

$$K_D = R_D^{-1} B_D^T P_D \tag{131}$$

$K_D = diag(K_1, K_2, \dots, K_N)$ and $P_D = diag(P_1, P_2, \dots, P_N)$ is the solution of the Riccati equation

$$A_D^T P_D + P_D A_D - P_D B_D R_D^{-1} B_D^T P_D + Q_D = 0 \tag{132}$$

The close loop system and optimal cost will be

$$\dot{x} = (A_D - B_D K_D) x \tag{133}$$

$$J_D^* = x_0^T P_D x_0 \tag{134}$$

It is clear that the obtained results are optimal for a closed loop system in form of (134); however, for an interconnected system of (125), the closed loop system will be in form of (136) and the obtained solution is not optimal. The decentralized optimal control is

suboptimal for the system. Considering the interconnectivity of the system and the closed loop system (136), the interconnections of the system, matrix A_C, plays the perturbation role in the system and system will be suboptimal.

$$\dot{x} = (A_D - B_D K_D + A_C)x \tag{135}$$

$$\hat{A} = A_D - B_D K_D + A_C \tag{136}$$

It can be shown that the u_D^* is suboptimal for the system (116) if and only if $\hat{A}$ is stable. To calculate the cost function for (124), a suboptimality index is defined to measure the cost of the robustness of the control to the existing structural perturbations. Considering system (136), the performance index is defined as

$$J_D^+ = x_0^T H x_0 \tag{137}$$

$$H = \int_0^{+\infty} \exp\left(\hat{A}^T t\right) . G_D . \exp\left(\hat{A} t\right) dt \tag{138}$$

$$G_D = Q_D + P_D B_D R_D^{-1} B_D^T P_D \tag{139}$$

Matrix H is finite when the $\hat{A}$ is stable and it can be calculated as the unique solution of the Lyapunov matrix equation of the

$$\hat{A}^T H + H\hat{A} + G_D = 0 \tag{140}$$

The decentralized control approach for interconnected system is designed and applied to the case study model subsystems for both charging and discharging modes. Each battery should charge and discharge independently to damp the frequency deviation in the interconnected system. Using the discussed decentralized framework, we design the optimal controllers for each subsystem. Each subsystem has 17 states ($n = 17$) one input

($p = 1$) and 8 outputs ($m = 8$) including dynamics of the battery in each area. Batteries firing angles are considered as control input to schedule the batteries active and reactive power to damp the frequency deviations. The system eigenvalues after applying decentralized controls are shown in Fig. 74. It is shown that the inter-area oscillation modes have moved to the left but still they are slow and will be problematic for the system. These complex modes belong to the first area, so by replacing the first area control with a more effective control we will be able to improve the system response.

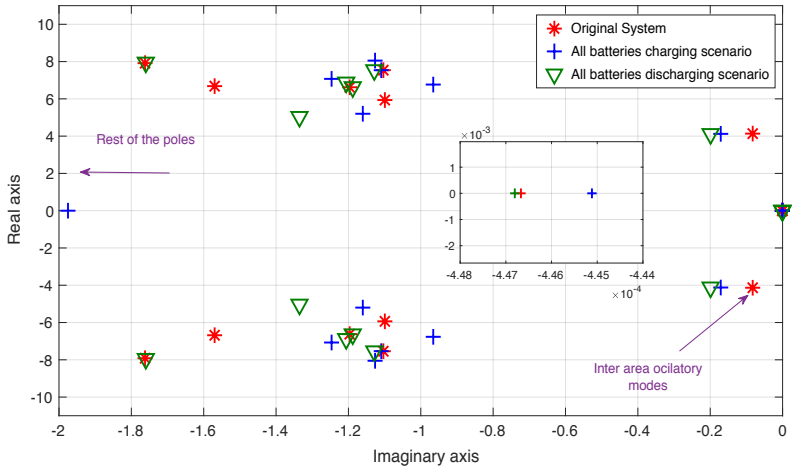

Figure 74. Poles of the case study model

7.3.3. Step 3: Optimal Pole Placement

In optimal control, solutions minimize the overall cost of the control system, meanwhile, using the proper weighting matrices helps to target specific states to force system for the desired results. However, finding the proper weighting matrices in large-scale systems to reach a desired performance is a challenging issue. Rousan in [97] proposed a solution to find an optimal gain to shift systems' poles to desired locations. This method has the

capability of shifting both real and complex poles individually or simultaneously. Considering a system as (109), it is shown that we can design a feedback control $u = Kx$ such that it shifts the original systems poles to desired positions. At the same time feedback gain, K, minimizes the quadratic performance index of the system given in (141).

$$J = \frac{1}{2}\int_0^t (x^T Q x + u^T R u) d\tau \tag{141}$$

To move a real pole to a desired location the control gain is

$$K = -R^{-1} B^T c M c^T \tag{142}$$

$$M = (q - p)/(c^T B R^{-1} B^T c) \tag{143}$$

Where p is the new and desired position of the pole q, and c is the associate eigenvector of the p.

To move a pair of poles of $a \pm jb$

$$w = ([a \quad -b]^T, [b \quad a]^T) \tag{144}$$

$$M = ([t \quad v]^T, [v \quad y]^T) \tag{145}$$

Considering

$$([s \quad f]^T, [f \quad h]^T) = c^T B R^{-1} B^T c \tag{146}$$

c^T is the left eigenvectors associated with the complex poles, and the characteristic polynomial of the reduced closed loop system (for the given pair of the complex poles) has the form of

$$n^2 + d_1 n + d_2 = 0 \quad (147)$$

Then

$$d_1 = st + hy + 2fv - 2a \quad (148)$$

$$(sh - f^2)(ty - v^2) = d_2 - (fb - as)t + (ha + fb)y - (hb - sb - fa - a^2)v - b^2 - a^2 \quad (149)$$

To M be non-negative definite symmetric matrix, the following conditions should be satisfied

$$t > 0 \text{ and } ty - v^2 > 0 \quad (150)$$

The control gain to relocate the complex poles is

$$K = -R^{-1}B^T P \quad (151)$$

$$P = cMc^T \quad (152)$$

System poles can be move simultaneously by summation of the gains for each pole placement.

The undamped frequency oscillation modes are located in the first area (see Fig. 75). The critical complex poles that cause the frequency oscillations and need to be relocated are $-0.0053 \pm j4.35$ (for the original subsystem 1). By moving the critical poles to the left, we manage to suppress the frequency deviation of the generators. In interconnected systems, new poles' location depends on the possibility of the complex poles relocation based on existence of the solution for (148)- (149) equations. The new poles effect the rest of the system through the interconnected part.

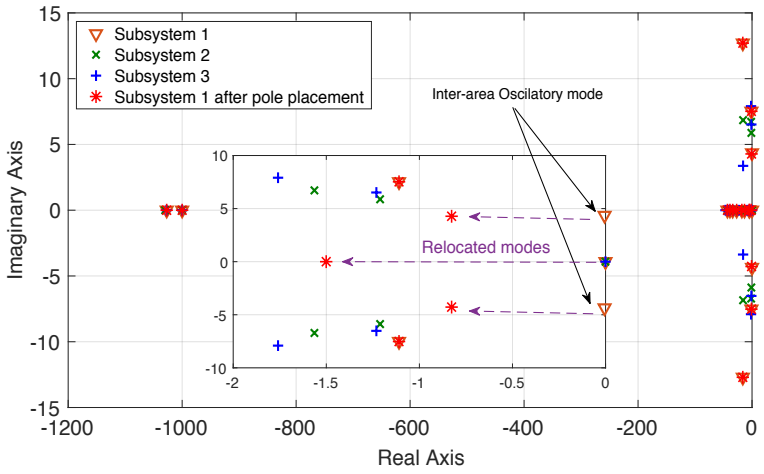

Figure 75. Poles of the case study model subsystems

7.3.4. Step 4: Hybrid Control for Interconnected Systems

The subsystem i of our power system case study with the large-scale battery is represented with two state space models for charging and discharging scenarios. The battery in each operating mode faces four different scenarios that will choose the optimal one in each time interval as shown in (153) and (154). Thus, the control strategy should be able to frequently switch between charging and discharging operating conditions to optimize the battery's operation and reduce the frequency deviations of the system simultaneously. The proposed control system schematic, for the battery in the area i is presented in Fig. 76.

$$J_{ci-j} = min\left(\int_{t_{k-1}}^{t_k}\left(x_{i-j}^T\, Q_{ci-j}\, x_{i-j} + u_{ci-j}^T\, R_{ci-j}\, u_{ci-j}\right)\, d\tau\right) \tag{153}$$

$$J_{di-j} = min\left(\int_{t_{k-1}}^{t_k}\left(x_{i-j}^T\, Q_{di-j}\, x_{i-j} + u_{di-j}^T\, R_{di-j}\, u_{di-j}\right)\, d\tau\right) \tag{154}$$

$$for\ j = 1{:}4\ \ and\ \ \ i = 1{:}3$$

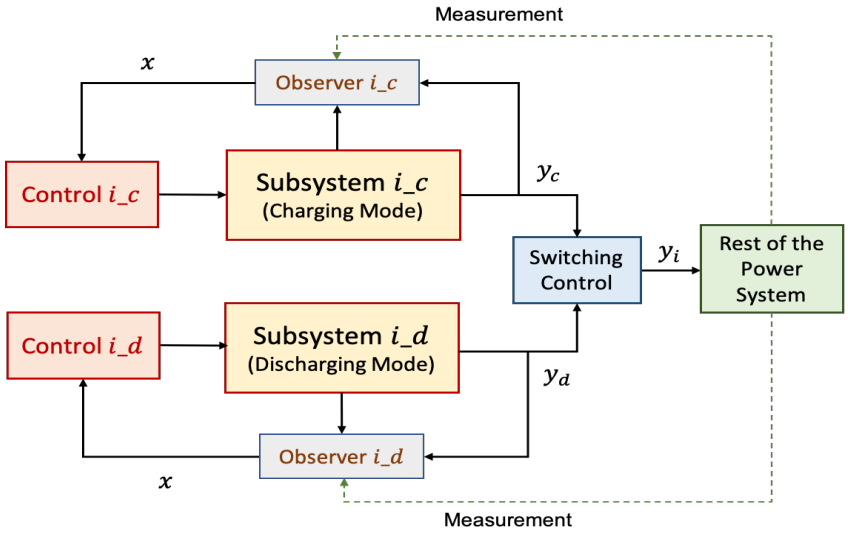

Figure 76. Control design approach based on observer-based decentralized control for interconnected systems in presence of the large-scale battery

We use normalized cost function for each subsystem to prevent frequent and unnecessary switching between charging and discharging modes. J_{ci-j} represents the charging cost function in the k^{th} time interval for the subsystem i faces scenarios j. Similarly, J_{di-j} represents the discharging cost function in the k^{th} time interval for the subsystem i faces scenarios j.

Each battery in subsystem $i = 1{:}3$ has two modes of charging and discharging for operation. Each of these modes will face four operation scenarios from the other two areas (based on the possible combinations of their batteries' operation modes). Also, Q_{ci-j}, R_{ci-j}, Q_{di-j}, R_{di-j} define the state and input weighting matrices for charging and discharging conditions, respectively.

The second generator frequency deviation under optimal switching policy based on hybrid control's final decision are shown with purple line in Fig. 77. The jumps in the simulation

are the updated initial conditions in result of the batteries switching between the charging and discharging modes.

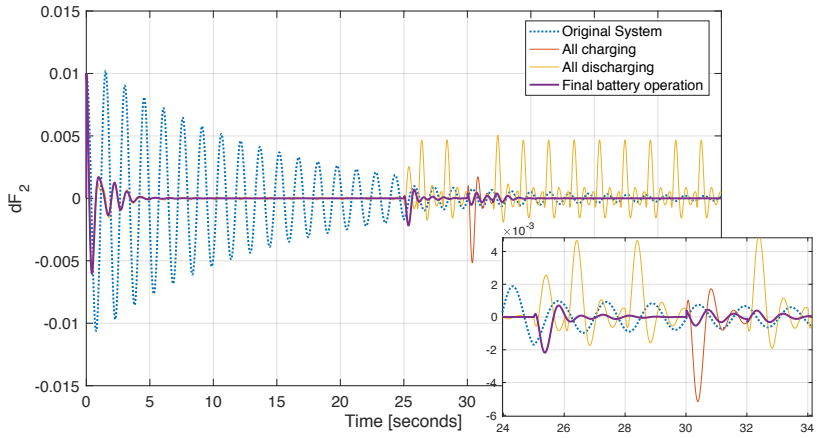

Figure 77. Frequency deviation of the generator two in the first area for; (i) original system, (ii) all battery charging scenario, (iii) all battery discharging scenario, and (iv) final batteries operation

The red and yellow lines show the generator's frequency deviation for battery's charging and discharging scenarios with decentralized state feedback control, while in each time interval, the initial conditions of the subsystem (the first area) is updated. The zoomed section shows the initial condition update. The final battery operation (the purple line) overlaps the charging or discharging operation, and it remains unchanged for the next intervals if the cost function is still lower than the other operating mode

7.4. Centralized Output Feedback Control

Considering the fact that having access to a large-scale system states information is infeasible, the best approach to design a control system for such systems is output-based

control approaches. In this section we assume that we have access to all system's output information. For the system (109), considering the cost function in (110), the control law for centralized optimal control is

$$u = Ky = KCx \tag{155}$$

$$K = -R^{-1}B^{T}P\Lambda C^{T}(C\Lambda C^{T})^{-1} \tag{156}$$

$$\hat{A}^{T}P + P\hat{A} = -\hat{Q} \tag{157}$$

$$\hat{A} = A + BKC \tag{158}$$

$$\hat{Q} = Q - PBR^{-1}B^{T}P \tag{159}$$

The hybrid control design is similar to the centralized state feedback approach. By designing the centralized output feedback and implementing on the case study mode the second generator frequency deviation will be as Fig. 78.

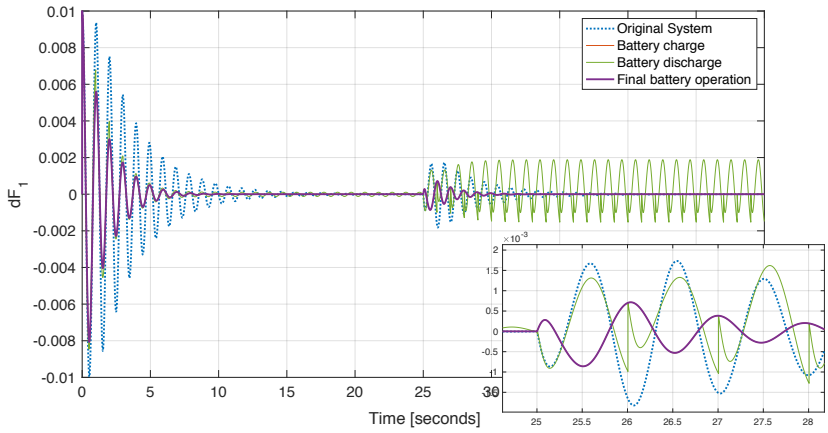

Figure 78. Frequency deviation of the generator two in the first area for; (i) original system, (ii) all battery charging scenario, (iii) all battery discharging scenario, and (iv) final batteries operation

7.5. Decentralized Output Feedback Control

There are several studies on decentralized state feedback [88]- [90] and output feedback

[92]– [94] control design methods. Particularly, the output feedback control design has attracted more attention from research scholars as in real-world applications, not all states of the systems are accessible. Moreover, several literatures contribute on both theory and numerical methods to solve optimal output feedback control problems for decentralized systems [95]. In most of the aforementioned literature, any inputs to the subsystem other than local inputs are considered perturbations [85]. This makes the control design and implementation easier in large-scale systems; however, the control system will be more conservative, and the system operation will be different from expected results with higher control cost [96].

In this section, we consider a large-scale power system as the case study model and develops a framework for decentralized optimal multi-channel output feedback control design to damp inter-area oscillation. In this regard, we use local large-scale batteries to control the frequency deviations of the generators locally.

Multi-Channel Optimal Output Feedback Control

In optimal decentralized control design approaches, the goal is to achieve an optimal global performance by designing local feedback controls. The key feature of these systems is that individual agents must make decisions with only partial knowledge of the whole system’s states, as having access to the all system's information is infeasible and almost impossible.

Consider an interconnected system as (160); we assume that we have only access to the system's local outputs.

$$\begin{cases} \dot{x} = Ax + \sum_{i=1}^{v} B_i u_i \\ y_i = C_i x \end{cases} \qquad for\ \forall\ i \in v \tag{160}$$

where $x \in R^n$, $u \in R^n$, and $y \in R^m$ are states, inputs, and outputs of the system, and v is the number of subsystems.

The proposed optimal decentralized output control design aims to find proper u_i such that minimize the desired cost function. For a linear system (160), the standard cost function (performance index) that we aim to minimize is defined as

$$J = \int_0^t (x^T Q x + \sum_{i=1}^{v} u_i^T R_i u_i) d\tau \tag{161}$$

and the feedback gain is

$$u_i = K_i y_i \tag{162}$$

The system (1) with the defined control law in (3) is

$$\dot{x} = A_c x \tag{163}$$

$$A_c = A + \sum_{i=1}^{v} B_i K_i C_i \tag{164}$$

$$K_i = -R_i^{-1}(B_i^T P L C_i^T)(C_i L C_i^T)^{-1} \tag{165}$$

Note that $(C_i L C_i^T)^{-1}$ must be invertible.

The solution to the close loop system is

$$x = e^{A_c t} x(0) \tag{166}$$

$x(0)$ is system's initial condition and

$$J = x(0)^T \left(\int_0^{\infty} e^{A_c t}\ \hat{Q}\ e^{A_c t}\ dt \right) x(0) \tag{167}$$

$$J = x(0)^T P x(0) \tag{168}$$

Where P satisfies the Lyapunov equation

$$A_c^T P + P A_c^T + \hat{Q} = 0 \tag{169}$$

$$X_0 = x(0).x(0)^T \tag{170}$$

To calculate the optimal gain with guarantee of the convergence, we follow the gradient algorithm as

i) Choose an initial matrix K_{0i} that stabilize the system and a proper step size of ε

ii) Solve equation (9) for $\hat{Q}$

iii) Solve equation (14) for L

iv) Calculate $\nabla_i^j \mathcal{H} = B_i^T P^j L^j C_i^T + R_i K_i^j C_i L^j C_i^T$

v) Find $K_i^{j+1} = K_i^j - \varepsilon \nabla_i^j \mathcal{H}$

vi) Solve for J^{j+1}

vii) Go back to *ii*

The step size of ε is adjustable based on $\mathcal{H}$ stiffness and $\partial \mathcal{H} / \partial K$ or calculated based on the Anderson-Moore algorithm [26].

The decentralized optimal output feedback control strategy is used to find the optimal output gain for all possible combinations of the batteries' operation modes.

The proposed hybrid output control system schematic for each battery is presented in Fig. 79.

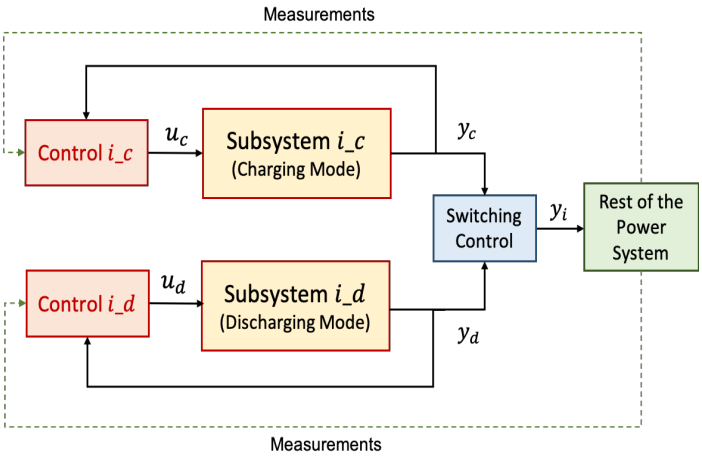

Figure 79. Control design approach based on decentralized control for interconnected systems in the presence of the large-scale battery

At each time interval, the hybrid controller of each subsystem first calculates possible charging output (y_c) and discharging output (y_d); and the corresponding normalized cost functions as (153) and (154); to determine the operating mode for the next time interval. After selecting the most cost-effective mode, the controller also updates the next time interval's initial condition. Similar to the decentralized state feedback control, for switching, we use normalized cost function for each subsystem to prevent frequent and unnecessary switching between charging and discharging modes. J_{ci-j} represents the charging cost function in the k^{th} time interval for the subsystem i faces scenarios j. Similarly, J_{di-j} represents the discharging cost function in the k^{th} time interval for the subsystem i faces scenarios j.

Each battery in subsystem $i = 1{:}3$ has two modes of charging and discharging for operation. Each of these modes will face four operation scenarios from the other two areas (based on the possible combinations of their batteries' operation modes). Also, Q_{ci-j}, R_{ci-j},

Q_{di-j}, R_{di-j} define the state and input weighting matrices for charging and discharging conditions, respectively.

A switching policy will be considered to shift between charging and discharging conditions and moving in the operating spectrum to minimize the cost function in each time interval of (t_{k-1}, t_k) and, consequently, the battery's total cost function in the power system. The hybrid controller in each area selects the mode with minimum cost function as the operating mode during the time intervals. Then, the system's states are updated based on the selected mode and the selected output controller. The control design's objective is to damp the generators' frequency deviation using the inputs u_{ci-j}, and u_{di_j}. The Q_{ci_j} and Q_{di_j} are designed to reduce the system's frequency deviation with an optimal cost.

Each battery in subsystem $i = 1{:}3$ has two modes of charging and discharging for operation. Each of these modes will face four operation scenarios from the other two areas (based on the possible combinations of their batteries' operation modes). Also, Q_{ci-j}, R_{ci-j}, Q_{di-j}, R_{di-j} define the state and input weighting matrices for charging and discharging conditions, respectively.

A switching policy will be considered to shift between charging and discharging conditions and moving in the operating spectrum to minimize the cost function in each time interval of (t_{k-1}, t_k) and, consequently, the battery's total cost function in the power system. The hybrid controller in each area selects the mode with minimum cost function as the operating mode during the time intervals. Then, the system's states are updated based on the selected mode and the selected output controller. The control design's objective is to damp the

generators' frequency deviation using the inputs u_{ci-j}, and u_{di_j}. The Q_{ci_j} and Q_{di_j} are designed to reduce the system's frequency deviation with an optimal cost.

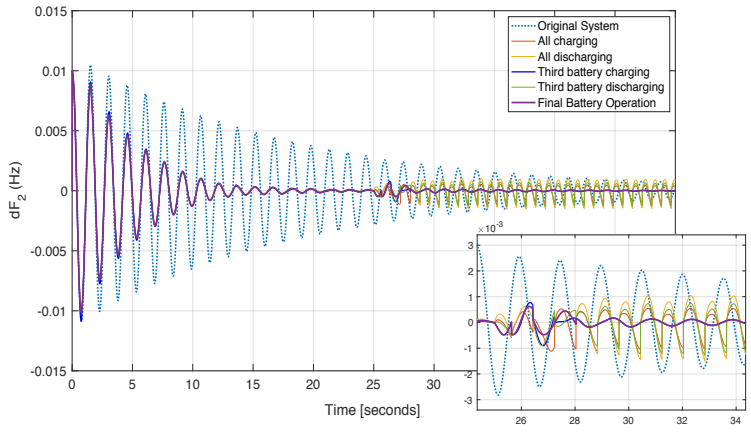

Figure 80. Frequency deviation of the generator two in the first area for; (i) original system with no battery operation; (ii) only charging mode; (iii) only discharging mode; (iv) first and second batteries charge and third one discharges (v) first and second batteries discharge and third one charges (vi) hybrid control final decision.

To elaborate on the switching policy and demonstrate how the hybrid controller decides between all scenarios, the battery's detailed operation mechanism under switching condition for the generator number two is shown in Fig. 80. Based on the hybrid controller's decision, the optimal controllers' initial conditions get updated at the beginning of the next interval. The blue dotted line shows the original frequency deviation of the generator. The red and yellow lines show the generator's frequency deviation for battery's charging and discharging scenarios with output feedback control, while in each time interval, the initial conditions of the subsystem (the first area) is updated. The zoomed section shows the initial condition update. The bright blue line shows the system frequency deviation for the case batteries in the first and second area are charging, and the third

battery is discharging, and green line shows the opposite scenario. The other scenarios are not plotted to have a clear figure. The final battery operation (the purple line) overlaps the charging or discharging operation, and it remains unchanged for the next intervals if the cost function is still lower than the other operating mode. The batteries inverter firing angle or the control efforts are shown in Fig. 81. Batteries active and reactive output power due to the inverters' angles deviation is shown in Fig. 82.

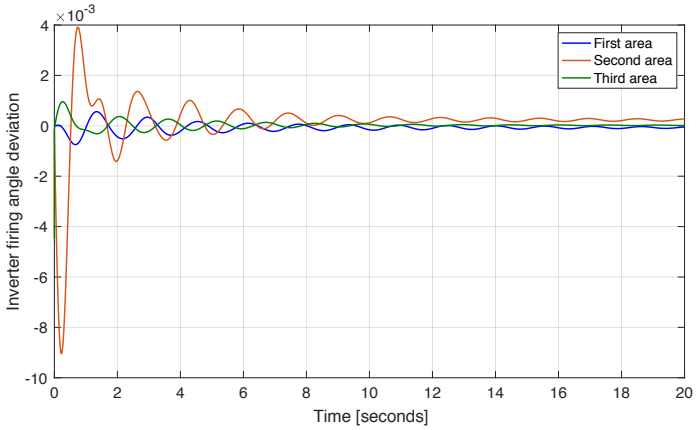

Figure 81. Control effort (inverter's firing angle deviation) for each area

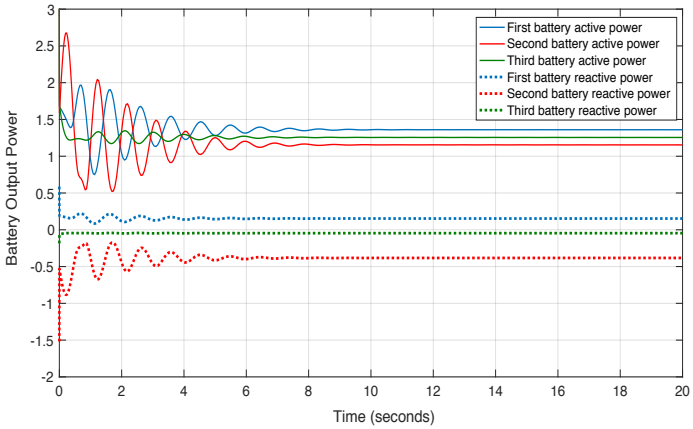

Figure 82. Batteires active and reactive output power for each area

Finally, Buses voltage deviation in result of the batteries operation have been presented in Fig. 83. The buses voltage deviations are less than two percent.

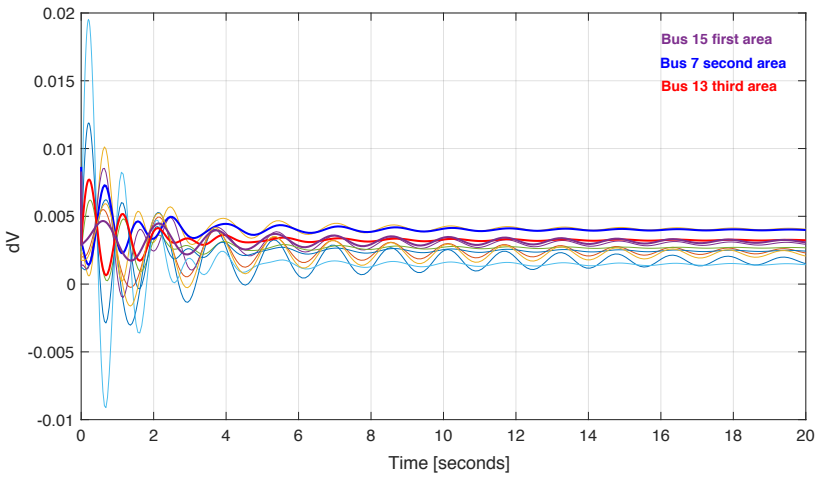

Figure 83. Buses voltage deviation

CONCLUSION

This dissertation considers battery integration's impact on the power system in both distribution and transmission level.

At the distribution level, we investigate the small-scale battery integration into the power system. It is shown that under the current electricity tariff, the higher penetration level of renewables integration into the power system causes serious challenges such as over-voltage and frequency deviations in the power grid. Sensitivity analysis is conducted to find the most effective parameters on the load exchange between the customer and POD's distribution system.

Energy consumption-based and demand-based tariffs are introduced to minimize the exchanged loads positive and negative peaks and load profile's sudden deviations. Results confirm the effectiveness of the tariff regulation approach.

In the transmission level, the effect of the unmanaged renewables' integration on the power system's coherency is investigated. It is shown that the coherency of the power system and inter-area frequency deviation depends on power system exchange through transmission lines. Large-scale batteries are considered to mitigate the inter-area frequency deviations in the case study model.

A large-scale battery's dynamic model in d-q axis is developed to simulate the battery's active and reactive power output in the power grid. Centralized and decentralized state and output feedback controls are designed for the batteries to schedule their active and reactive

power to minimize the frequency deviation without compromising the system's voltage stability.

- In future work, we aim to extend this study to:
- New tariff definition for future power grid with new architecture.
- New energy market design based on new service providers.
- Investigate the impact of large-scale battery integration on power system transient stability.
- Design the decentralized control system considering the unknown state of operation for the other areas.
- Considering the impact of the communication delay on the control system.
- Investigating the impact of renewables integration and cyber-attack vulnerability of the power grid on power system stability.
- Design model predictive control with considering constraints on control input and system outputs.
- Considering the large-scale batteries as a third-party service provider under energy market regulations.

REFERENCES

[1] https://www.aps.org/policy/reports/popa-reports/upload/integratingelec.pdf

[2] https://www.energy.gov/sites/prod/files/SunShot%20Vision%20Study.pdf

[3] J. C. Neely, J. Johnson, R. H. Byrne, and R. T. Elliott, “Structured Optimization for Parameter Selection of Frequency-Watt Grid Support Functions for Wide-Area Damping,” International Journal of Distributed Energy Resources and Smart Grids, pp. 69-94, Vol. 11, No. 1, January 2015.

[4] R.A Biroon, P Pisu, and and D. Schoenwald, “Decentralized Servomechanism Control Design for Inter-Area Oscillations Damping in in Power Systems”. IEEE, North American Power Symposium (NAPS), Oct. 2019.

[5] M. Singh, V. Khadkikar, A. Chandra, and R.K. Varma, “Grid interconnection of renewable energy sources at the distribution level with power-quality improvement features", IEEE transactions on power delivery pp. 307-315, 2010.

[6] X. Liang, "Emerging power quality challenges due to integration of renewable energy sources", IEEE Transactions on Industry Applications 53.2 pp. 855-866 2010

[7] A. Osmani, J. Zhang, V. Gonela, and I. Awudu, “Electricity generation from renewables in the United States: Resource potential, current usage, technical status, challenges, strategies, policies, and future directions.” Renewable and Sustainable Energy Reviews, 24, 454-472, 2013.

[8] Yang, P., Chavali, P., Gilboa, E., & Nehorai, A. (2013). Parallel load schedule optimization with renewable distributed generators in smart grids. *IEEE Transactions on Smart Grid*, *4*(3), 1431-1441.

[9] M. Castillo-Cagigal, E. Caamaño-Martín, E. Matallanas, D. Masa-Bote, A. Gutiérrez, F. Monasterio-Huelin, et al. “PV self-consumption optimization with storage and Active DSM for the commercial sector.” Solar Energy, pp:2338–48, 2011

[10] M. Muratori, and G. Rizzoni. "Commercial demand response: Dynamic energy management and time-varying electricity pricing." IEEE Transactions on Power systems, pp: 1108-1117, 2016.

[11] Anwar, Adnan, and H. R. Pota. "Loss reduction of power distribution network using optimum size and location of distributed generation." *AUPEC 2011*. IEEE, 2011.

[12] He, Jinwei, Md Shirajum Munir, and Yun Wei Li. "Opportunities for power quality improvement through DG-grid interfacing converters." *The 2010 International Power Electronics Conference-ECCE ASIA-*. IEEE, 2010.

[13] Reza, M., et al. "Impacts of distributed generation penetration levels on power systems transient stability." *IEEE Power Engineering Society General Meeting, 2004.*. IEEE, 2004

[14] X. Liang, "Emerging power quality challenges due to integration of renewable energy sources", IEEE Transactions on Industry Applications 53.2 pp. 855-866 2010

[15] A. Osmani, J. Zhang, V. Gonela, and I. Awudu, “Electricity generation from renewables in the United States: Resource potential, current usage, technical status, challenges, strategies, policies, and future directions.” Renewable and Sustainable Energy Reviews, 24, 454-472, 2013.

[16] F. Katiraei, and R. A. Julio, "Solar PV integration challenges." IEEE Power and Energy Magazine 9.3 pp. 62-71, 2011
[17] K. Petrou, L.F. Ochoa, A. T. Procopiou, J. Theunissen, J. Bridge, T. Langstaff, and K. Lintern, “Limitations of residential storage in PV-rich distribution networks: An Australian case study.” Power & Energy Society General Meeting (PESGM) ,pp. 1-5, 2018.
[18] Roghieh A. Biroon,, Zoleikha Abdollahi, and Ramtin Hadidi, " On the Tariff Modification for Future Electric Vehicle Connection to the Grid”, North America Power Symposium (NAPS) 2019.
[19] S. Koch, D. Meier, M. Zima, M. Wiederkehr, and G. Andersson, "An active coordination approach for thermal household appliances – local communication and calculation tasks in the household," 2009 IEEE Bucharest Power Tech Conference, June 28th - July 2nd, Bucharest, Romania, 2009.
[20] V. Hamidi, F. Li, and F. Robinson, "Demand response in the UK’s domestic sector," Electric Power Systems Research, vol. 79, no. 12, pp 1722-1726, Dec. 2009.
[21] M. S. Majid, H. A. Rahman, M. Y. Hassan, and C. A. Ooi, "Demand side management using direct load control for residential," 4th Student Conference on Research and Development, pp.241-245, Jun. 2006.
[22] D. G. Infield, J. Short, C. Home, and L. L. Freris, "Potential for Domestic Dynamic Demand-Side Management in the UK," IEEE Power Engineering Society General Meeting, 2007.
[23] Ayón X, Gruber JK, Hayes BP, Usaola J, Prodanovic´ M. “An optimal day-ahead load scheduling approach based on the flexibility of aggregate demands”. Appl Energy 2017;198:1–11
[24] Y. Cao, S. Tang, C. Li, P. Zhang, Y. Tan, Z. Zhang, and J. Li, “An Optimized EV Charging Model Considering TOU Price and SOC Curve”, IEEE Transaction on Smart Grid, 3(1), pp. 388-393, 2012.
[25] Y. T. Chen, “The factors affecting electricity consumption and the consumption characteristics in the residential sectora case example of Taiwan,” Sustainability (Switzerland), vol. 9, no. 8, p. 1484, 2017.
[26] R.A. Biroon, Z. Abdollahi, and R. Hadidi,” Effect of Tariff on Commercial Load Profile Optimization in Presence of the Battery”, in Proc. 2019 IEEE Ind. Appl. Soc. Ann. Meeting, Baltimore, MD USA, pp. 1-8, DOI: 10.1109/IAS.2019.8911955.
[27] R.A. Biroon, Z. Abdollahi, and R. Hadidi,” Fast and Regular Electric Vehicle Charging Impacts on the Distribution Feeders”, IAS Annual meeting, Baltimore, MD, 2019.
[28] Weniger, J., Tjaden, T., & Quaschning, V. (2014). Sizing of residential PV battery systems. Energy Procedia, 46, 78-87.
[29] Aichhorn, A., Greenleaf, M., Li, H., & Zheng, J. (2012, July). A cost effective battery sizing strategy based on a detailed battery lifetime model and an economic energy management strategy. In 2012 IEEE Power and Energy Society General Meeting (pp. 1-8). IEEE.
[30] Zhang, Y., Lundblad, A., Campana, P. E., Benavente, F., & Yan, J. (2017). Battery sizing and rule-based operation of grid-connected photovoltaic-battery system: A case study in Sweden. Energy conversion and management, 133, 249-263.

[31] Khorramdel, H., Aghaei, J., Khorramdel, B., & Siano, P. “Optimal battery sizing in microgrids using probabilistic unit commitment”. IEEE Transactions on Industrial Informatics, 12(2), 834-843. 2015.

[32] https://loadshape.epri.com/wholepremise

[33] https://www.greentechmedia.com/articles/read/hour-debate-california-time-of-use-rates#gs.41zBgS0

[34] https://batteryuniversity.com/learn/article/elevating_self_discharge.

[35] Bindner, H., Cronin, T., Lundsager, P., Manwell, J. F., Abdulwahid, U., & Baring-Gould, I. (2005). Lifetime modelling of lead acid batteries.

[36] Wu, Zhou, Henerica Tazvinga, and Xiaohua Xia. "Demand side management of photovoltaic-battery hybrid system." Applied Energy 148 (2015): 294-304

[37] Phiri, S. F., and K. Kusakana. "Demand Side Management of a grid connected PV-WT-Battery hybrid system." 2016 International Conference on the Industrial and Commercial Use of Energy (ICUE). IEEE, 2016.

[38] H. Hatta, M. Asari, and H. Kobayashi, “Study of Energy Management for Decreasing Reverse Power Flow from Photovoltaic Power Systems,” *SAE2009, pp. 1-5, Sept. 2009.*

[39] H. Hatta and H. Kobayashi, "A Study of Centralized Voltage Control Method for Distribution System with Distributed Generation," *in Proc. CIRED 2007, No. 0330.*

[40] J. Oravec, and M. Bakošová. "Alternative LMI-based robust MPC design approaches." IFAC-PapersOnLine 48.14 (2015): 180-185.

[41] R. Preece, J. V. Milanović, A. M. Almutairi, and O. Marjanovic. “Damping of inter-area oscillations in mixed AC/DC networks using WAMS based supplementary controller.” IEEE Transactions on Power Systems, 28(2), 1160-1169, 2012.

[42] R. Cresap, W. Mittelstadt, D. Scott, C. Taylor, “Operating experience with modulation of the pacific HVDC intertie,” IEEE Transactions on S. Nabavi and A. Chakrabortty, “Distributed estimation of inter-area oscillation modes in large power systems using alternating direction multiplier method,” in Proc. IEEE Power Energy Soc. Gen. Meeting, National Harbor, MD, USA, 2014, pp. 1–5

[43] Lin Bo; Lv Lin; Liu Jun-Yong; Liu You-Bo; Zhao Wei; Tian Jun-Jie,”An identification method for critical low frequency oscillation mode based on inter-area oscillation relevant generator contribution factor’, IEEE, International Conference on Power System Technology 2014: 408 - 414

[44] T. Jiang et al., “A novel dominant mode estimation method for analyzing inter-area oscillation in China Southern power grid,” IEEE Trans. Smart Grid, vol. 7, no. 5, pp. 2549–2560, Sep. 2016.

[45] http://powerit.utk.edu/research.html

[46] Rogers, Graham. *Power system oscillations*. Springer Science & Business Media, 2012.

[47] E.V. Larsen and 1.H. Chow, "SVC Control Design Concepts for System Dynamic Performance", Application of Static VAR Systems for System Dynamic Performance, IEEE pUblication 87THOI 87-5-PWR, 1987, pp. 36-53.

[48] S. Geeves, K. Bergmaa, D. Tetzmann and R. Witzmann, , Improvement of System Stability by the Harker Static V ar Compensators / UK V erification o f System Performance by Digital and Real-Time Simulation', ICPST' 94, Beijing, China.

[49] Nelson Martins and Leonardo T.G. Lima, "Determination of Suitable Locations for Power System Stabilizers and Static VAR Compensators for Damping Electromechanical Oscillations in Large Scale Power Systems", IEEE Transactions on Power Systems, Vol. 5, No.4, November 1990, pp. 1455-1463.

[50] Chow, Joe H., ed. *Power system coherency and model reduction*. Vol. 84. New York: Springer, 2013.

[51] I. J. Pérez-Arriaga, "Selective modal analysis with applications to electric power systems" Ph.D. Thesis, Department of Electrical Engineering and Computer Science, Massachusetts Institute of Technology, June 1981

[52] I.J. Pérez-Arriaga, G. C. Verghese, F. C. Schweppe, "Selective modal analysis with applications to electric power systems. Part I: Heuristic introduction. Part II: The dynamic stability problem. IEEE Trans. Power Apparatus Syst. **PAS–101**(9), 3117–3134 (1982)

[53] G. Cedersund, L.Rouco,G.C.Verghese, "Structure dreduction of dynamic biochemical models." In Proceedings of 10th International Conference on Systems Biology, Poster 2.091, Stanford, California, USA, 2009.

[54] X. Wu, F. Dorfler, and M. R. Jovanovi ¨ c, "Decentralized optimal control of inter-area oscillations in bulk power systems," in Proceedings of the 54th IEEE Conference on Decision and Control, Osaka, Japan, 2015, pp. 5532–5537.

[55] V, Krishnan, S. Chakrabarti, S. Srivastava,"A Robust Decentralized Wide Area Damping Controller for Wind Generators and FACTS Controllers Considering Load Model Uncertainties", IEEE Transactions on Smart Grid , vol. 9, no. 1, pp. 360-372, April 2016

[56] S.K. Pandey, S.R. Mohanty, N. Kishore, "A literature survey on LFC for conventional and distributed generation power systems", Renew. Sustain. Energy Rev. 25 (2013) 318–324

[57] Chandra, Souvik, Dennice F. Gayme, and Aranya Chakrabortty. "Coordinating wind farms and battery management systems for inter-area oscillation damping: A frequency-domain approach." *IEEE Transactions on Power Systems* 29.3 (2013): 1454-1462.

[58] Tsang, M. W., and D. Sutanto. "Damping inter-area oscillation using a battery energy storage system." (1997): 409-414.

[59] X. Sui, Y. Tang, H. He, and J. Wen, "Energy-storage-based low frequency oscillation damping control using particle swarm optimization and heuristic dynamic programming," IEEE Transactions on Power Systems, vol. 29, no. 5, pp. 2539–2548, September 2014.

[60] J. C. Neely, R. H. Byrne, C. A. Silva Monroy, R. T. Elliott, D. A. Schoenwald, D. Trudnowski, and M. Donnelly, "Damping of Inter-Area Oscillations using Energy Storage," IEEE Power & Energy Soc. General Meeting, Vancouver, Canada, July 2013.

[61] Mercier, Pascal, Rachid Cherkaoui, and Alexandre Oudalov. "Optimizing a battery energy storage system for frequency control application in an isolated power system." *IEEE Transactions on Power Systems* 24.3 (2009): 1469-1477.

[62] Murakami, Akiko, Akihiko Yokoyama, and Yasuyuki Tada. "Basic study on battery capacity evaluation for load frequency control (LFC) in power system with a large penetration of wind power generation." *IEEJ Transactions on Power and Energy*126 (2006): 236-242.

[63] Wang, Wenxi, et al. "Active and reactive power coordinated control strategy of battery energy storage system in active distribution network." *2017 32nd Youth Academic Annual Conference of Chinese Association of Automation (YAC)*. IEEE, 2017.

[64] Oudalov, Alexdandre, et al. "Value analysis of battery energy storage applications in power systems." *2006 IEEE PES Power Systems Conference and Exposition*. IEEE, 2006.

[65] G. W. Scott, V. F. Wilerker, and R. K. Shaltens, "Wind turbine generator interaction with diesel generation on an isolated power system," IEEE Transactions on PAS, vol. PAS-103, pp. 933–936, May 1984.

[66] P. Khayyer and U. Özgüner, "Decentralized control of large-scale storagebased renewable energy systems," IEEE Trans. Smart Grid, vol. 5, no. 3, pp. 1300–1307, May 2014.

[67] P. Kundur, "Power System Stability and Control". New York: published by Mc.Graw-Hill, 1994.

[68] Siljak, D. D. (1991). "Decentralized control of large-sca systems". New York: published by Academic Press.

[69] X. B. Chen and S. S. Stankovic, "Overlapping decentralized approach to automation generation control of multi-area power systems," Int. J. Control, volume. 80, no. 3, pages. 386–402, year 2007.

[70] U. Ozguner and H. Hemami, "Decentralized control of interconnected physical systems," Int. J. Control, vol. 41, no. 6, pp. 1445-1459, 1985.

[71] E.J, Davison, H.W, Smith, "Pole assignment in linear time invariant multivariable systems with constant disturbances", Automatica, volume 7, July 1971, pages 489-498.

[72] E.J, Davison, "The output control of linear time-invariant multivariable systems with unmeasurable arbitrary disturbances," IEEE Trans. on Automati Control., volume. AC-17, pages. 621430, Febuary 1976.

[73] J. C. Doyle, "Guaranteed margins for LQG regulators," *IEEE Trans. Autom. Contr.*, vol. AC-23, no. 4, pp. 756–757, Aug. 1978.

[74] https://www.wecc.org/Reliability/WECC%20Approved%20Energy%20Storage%20System%20Model%20-%20Phase%20II.pdf

[75] P. Pourbeik, *"Proposal for Simple Battery Energy Storage Model",* PPT presentation slides; prepared on 1/13/15.

[76] Beck, J. W., Carroll, D. P., Gareis, G. E., Krause, P. C., & Ong, C. M. (1976). A computer study of battery energy storage and power conversion equipment operation. IEEE Transactions on Power Apparatus and Systems, 95(4), 1064-1072.

[77] Salameh, Ziyad M., Margaret A. Casacca, and William A. Lynch. "A mathematical model for lead-acid batteries." IEEE Transactions on Energy Conversion 7.1 (1992): 93-98.
[78] Lu, C-F., C-C. Liu, and C-J. Wu. "Dynamic modelling of battery energy storage system and application to power system stability." IEE Proceedings-Generation, Transmission and Distribution 142.4 (1995): 429-435.
[79] Chandra, Souvik, Dennice F. Gayme, and Aranya Chakrabortty. "Using battery management systems to augment inter-area oscillation control in wind-integrated power systems." *2013 American Control Conference*. IEEE, 2013.
[80] Datta, Ujjwal, Akhtar Kalam, and Juan Shi. "Battery energy storage system for transient frequency stability enhancement of a large-scale power system." *2017 Australasian Universities Power Engineering Conference (AUPEC)*. IEEE, 2017.
[81] Adrees, Atia, Hooman Andami, and Jovica V. Milanović. "Comparison of dynamic models of battery energy storage for frequency regulation in power system." 2016 18th Mediterranean Electrotechnical Conference (MELECON). IEEE, 2016.
[82] Padyar, K. R. "Power System Dynamics Stability and Control, Hyderabad, AP." (2002).
[83] Shubhanga K. N. "Power System Analysis, a dynamic presentation" Pearson, 2018
[84] https://www.wecc.org/Reliability/WECC_Flexibility_Assessment_ExecSumm_2016-01-11.pdf
[85] Siljak, Dragoslav D. Decentralized control of complex systems. Courier Corporation, 2011.
[86] Benigni, A., D'Antona, G., Ghisla, U., Monti, A., & Ponci, F. (2009). A decentralized observer for ship power system applications: Implementation and experimental validation. IEEE Transactions on Instrumentation and Measurement, 59(2), 440-449
[87] Ficklscherer, P., and P. C. Müller. "Decentralized state observers for large-scale systems." IFAC Proceedings Volumes 17.2 (1984): 1153-1158.
[88] A. K. Singh and B. C. Pal, "Decentralized dynamic state estimation in power systems using unscented transformation," IEEE Trans. Power Syst., vol. 29, no. 2, pp. 794–804, Mar. 2014.
[89] Singh, Abhinav Kumar, and Bikash C. Pal. "Decentralized control of oscillatory dynamics in power systems using an extended LQR." IEEE Transactions on Power Systems 31.3 (2015): 1715-1728
[90] Schuler, Simone, Ulrich Münz, and Frank Allgöwer. "Decentralized state feedback control for interconnected systems with application to power systems." Journal of Process Control 24.2 (2014): 379-388
[91] R. A. Biroon, P. Pisu, and D. Schoenwald. "A Hybrid Control Framework for Large-Scale Battery Integration to the Power System for Stability Analysis. " American Control Conference (ACC) IEEE, 2020.
[92] Yuan, Lisong, Luke EK Achenie, and Weisun Jiang. "Linear quadratic optimal output feedback control for systems with poles in a specified region." International Journal of Control64.6 (1996): 1151-1164.
[93] W. Levine and M. Athans, "On the determination of the optimal constant output feedback gains for linear multivariable systems," IEEE Transactions on Automatic control, vol. 15, no. 1, pp. 44–48, 1970.

[94] J. Bernussou and J. Geromel, “An easy way to find gradient matrix of composite matricial functions,” IEEE Transactions on Automatic Control, vol. 26, no. 2, pp. 538–540, 1981.
[95] Rautert, Tankred, and Ekkehard W. Sachs. "Computational design of optimal output feedback controllers." SIAM Journal on Optimization 7.3 (1997): 837-852.
[96] Yan, Xing-Gang, Christopher Edwards, and Sarah K. Spurgeon. "Decentralised robust sliding mode control for a class of nonlinear interconnected systems by static output feedback." *Automatica* 40.4 (2004): 613-620.
[97] Rousan, N. S., and M. Edwin Sawan. "Pole placement by linear quadratic modification for continuous time systems." *1991 American Control Conference*. IEEE, 1991.